INVESTIGATION OF FINITE PHASED ARRAYS OF PRINTED ANTENNAS ON PLANAR AND CYLINDRICAL GROUNDED DIELECTRIC SLABS

A THESIS

SUBMITTED TO THE DEPARTMENT OF ELECTRICAL AND

ELECTRONICS ENGINEERING

AND THE INSTITUTE OF ENGINEERING AND SCIENCE

OF BILKENT UNIVERSITY

IN PARTIAL FULFILLMENT OF THE REQUIREMENTS

FOR THE DEGREE OF

MASTER OF SCIENCE

By

Onur Bakır

August, 2006

I certify that I have read this thesis and that in my opinion it is fully adequate, in scope and in quality, as a thesis for the degree of Master of Science.

Assist. Prof. Dr. Vakur B. Ertürk(Advisor)

I certify that I have read this thesis and that in my opinion it is fully adequate, in scope and in quality, as a thesis for the degree of Master of Science.

Prof. Dr. Ayhan Altıntaş

I certify that I have read this thesis and that in my opinion it is fully adequate, in scope and in quality, as a thesis for the degree of Master of Science.

Assoc. Prof. Dr. Özlem Aydın Çivi

Approved for the Institute of Engineering and Science:

Prof. Dr. Mehmet B. Baray
Director of the Institute

in loving memory of my father ...

ABSTRACT

INVESTIGATION OF FINITE PHASED ARRAYS OF PRINTED ANTENNAS ON PLANAR AND CYLINDRICAL GROUNDED DIELECTRIC SLABS

Onur Bakır
M.S. in Electrical and Electronics Engineering
Supervisor: Assist. Prof. Dr. Vakur B. Ertürk
August, 2006

Printed structures, in the form of a single printed antenna (printed dipole, patch, etc.) or an array of printed antennas on planar and cylindrical grounded dielectric slabs, are investigated. Full-wave solutions based on the hybrid method of moments (MoM)/Green's function technique in two different domains, the spectral and the spatial domains are used to analyze these types of geometries. Several numerical problems, encountered in the evaluation of both the spectral and spatial domain integrals are addressed and solutions for these problems are presented. Among them the two important ones are: (1) The infinite double integrals which appear in the asymptotic parts of the spectral domain MoM impedance matrix and the MoM excitation vector elements for planar grounded dielectric slabs are evaluated in closed-form in this thesis, resulting an improved efficiency and accuracy for the rigorous investigation of printed antennas. (2) In the space domain MoM solution of printed structures on planar grounded dielectric slabs, an accurate way of treating the singularity problem of the self-term and overlapping terms as well as the MoM excitation vector is presented along with a way to halve the order of space domain integrals by employing a proper change of variables and analytical evaluation of one of the integrals for each double integral.

Finally two different studies which use these improved methods are presented in order to asses their accuracy and efficiency: (1) Investigation of scan blindness phenomenon for finite phased arrays of printed dipoles on material coated electrically large circular cylinders, and its comparison with the same type of arrays on planar platforms. In this study effects on the scan blindness mechanism of several array and supporting structure parameters, including curvature effects, are discussed. (2) A discrete Fourier transform (DFT) based acceleration algorithm is used in conjunction with the generalized forward backward method (GFBM)

to reduce the computational complexity and memory storage requirements of the aforementioned full-wave solution method for the fast analysis of electrically large finite phased arrays of microstrip patches. As a result both the computational complexity and memory storage requirements are reduced to O(N) (of order N), where N is the number of unknowns.

Keywords: Microstrip antennas and antenna arrays, Method of moments, Green's function, Scan blindness.

ÖZET

TOPRAKLANMIŞ DÜZLEMSEL VE SİLİNDİRSEL DİELEKTRİK YÜZEYLER ÜZERİNDEKİ FAZ DİZİLİMLİ VE SONLU BASKI DEVRE ANTENLERİN İNCELENMESİ

Onur Bakır
Elektrik ve Elektronik Mühendisliği, Yüksek Lisans
Tez Yöneticisi: Yrd. Doç. Dr. Vakur B. Ertürk
Ağustos, 2006

Düzlemsel ve silindirsel yüzeyler üzerine basılmış, tek bir anten veya anten dizileri şeklindeki baskı devre yapıları, bir tam dalga çözümü olan Momentler Metodu (MoM), Green fonksiyonu karma tekniği kullanılarak incelenmiştir. Bu tezde hem spektral hem uzamsal bölgede kullanılan bu tekniğin uygulanışındaki sorunlar ele alınmış ve bu sorunlara yönelik çözümler sunulmuştur. Bunlar arasında göze çarpan iki tanesi: (1) Topraklanmış düzlemsel dielektrik materyaller üzerine basılmış, baskı devre yapıları için, spektral bölgede yazılmış MoM empedans matrisi ve MoM voltaj vektörü elemanlarının asimptotik kısımlarını oluşturan iki katlı integrallerin kapalı formlarının bulunması ve böylelikle verimlilik ve doğrulukta bir artış elde eldilmesi. (2) Yine aynı geometrideki yapılar için uzamsal bölgede yazılan MoM çözümünde, temel fonksiyonlar tam ya da yarım olarak üst üste geldiği zaman, MoM empedans matrisi ve MoM voltaj vektorü elemanlarında meydana gelen tekillik problemine, doğru bir çözüm bulunmuş ve yine bu elemanlardaki katlı integrallerin sayısını yarıya indirmek için bir yol öne sürülmüştür.

Son olarak bu geliştirilmiş metodların verimliliğini ve doğruluğunu göstermek için, bunların kullanıldığı iki ayrı çalışma sunulmuştur: (1) Dielektrik kapı büyük metal silindirler üzerindeki faz dizilimli, sonlu baskı dipol antenlerde tarama körlüğü olgusunun incelenmesi ve topraklanmış düzlemsel dielektrik yüzeylerdeki anten dizilerindeki durumla karşılaştırılması. Bu çalışmada anten dizileriyle ilgili bir çok parametrenin ve yüzey eğiminin tarama körlüğü mekanizması üzerine etkileri incelenmiştir. (2) Ayrık Fourier dönüşümü tabanlı bir hızlandırma algoritmasının, genel ileri-geri metodu ile birlikte kullanılmasıyla, elektriksel olarak büyük faz dizilimli sonlu baskı anten dizilerinin tam dalga çözümünde hesaplama

karmaşıklığı ve hafıza gereksinimlerinin azaltılmasına yarayan hızlı bir metod geliştirilmesi. Bu sayede hesaplama karmaşıklığı ve hafıza gereksinimleri O(N) (N. dereceden) bir seviyeye düşürülmüştür. N bilinmeyenlerin sayısıdır.

Anahtar sözcükler: Mikroşerit antenler ve anten dizileri, Momentler metodu, Green fonksiyonu, Tarama körlügü.

Acknowledgement

I would like to express my sincere gratitude to my supervisor Assist. Prof. Vakur B. Ertürk for his guidance, encouragement and support not only in this thesis but also during my undergraduate education. Thank you for being there, supporting my decisions during the worst and best times of my academic career. He has been the best advisor, supervisor and also a good friend to me and he will always be.

I would like to thank Prof. Ayhan Altıntaş and Assoc. Prof. Özlem Aydın Çivi from METU for being in my jury and reading this long thesis. I would also like to mention Assoc. Prof. Özlem Aydın Çivi again and express my special thanks to her for her collobration in my research.

I would like to thank to Prof. İrşadi Aksun from Koç University and Assist. Prof. Lale Alatan from METU for their interest and support in this thesis.

Finally I would like to thank to my family, friends, officemate (Niyazi), and to my dearest Hande for their love, understanding and support.

Contents

List of Figures

List of Tables

Chapter 1

Introduction

Printed antennas and arrays are preferred over the conventional antennas and arrays in a wide range of applications starting from military systems like airborne, ship borne, space borne systems, naval or aircraft radar applications to the civilian systems like wireless or satellite communications, mobile base stations, cellular phones, remote sensing and biomedical applications. This is due to their advantages over conventional antennas and arrays such as low fabrication costs, light-weight, direct integrability with the solid state and other microwave devices, and conformity to the surface where they can be mounted on planar grounded dielectric slabs or conform to the coated convex perfectly electric conducting (PEC) structures like circular, elliptical cylinders, spheres etc. However, the majority of the computer-aided design (CAD) tools, which are developed to perform the full-wave analysis of these structures exhibit memory storage and computing time problems when these structures are electrically large. Furthermore, when the printed arrays on coated convex bodies are considered, available tools are scant, and results obtained from these tools yield accuracy problems, in particular if the arrays and/or array supporting structures are electrically large. Therefore, a great number of studies using the integral equation (IE) based method of moments (MoM) solutions, which use the appropriate Green's function representations, have been directed toward the development of efficient and accurate methods that can be implemented in CAD packages to investigate printed arrays

mounted on various shaped coated host platforms [1]-[17].

In the light of above discussion, in this thesis a hybrid method based on the combination of MoM with special Green's function representations is used to investigate printed antennas/arrays on planar and cylindrical grounded dielectric slabs in both spatial and spectral domains. These Green's function representations include all the effects of the grounded dielectric slabs and they are specific to the geometry that is being analyzed. In the spectral domain, an infinitesimal current source on the air-dielectric interface is assumed and then the corresponding Green's function representation, which might involve Fourier integrals or Fourier summations, is found by applying the boundary conditions for the electric and magnetic fields. However, to obtain the spatial domain Green's function representations, we usually start with the spectral domain representations and perform several asymptotic techniques and various approximations to evaluate the aforementioned integrals and summations.

On the other hand MoM is used to convert an integral equation, which is the electric field integral equation (EFIE) in our case, to a system of linear equations. In this method currents on the surface of PEC are modeled as a sum of known entire-domain or sub-domain basis functions with unknown coefficients written in the form of a vector (MoM current vector) and found by solving the system of linear equations. The most important element of this system of linear equations is the MoM impedance matrix whose elements denote the self and mutual couplings between the basis functions. Accurate evaluation of these elements can be carried out both in spatial and spectral domains, which is explained in Chapter 2. Finally, the right hand side of this matrix equation is the voltage (excitation) vector whose elements represent the interaction between the feeding mechanism and the testing functions. It is important to note that the accuracy and efficiency of this hybrid MoM/Green's function technique depends on the accurate and efficient evaluation of the MoM impedance matrix entries, which strongly depend on the Green's function representations. When the spectral domain calculations are considered for planar and cylindrical geometries, each has a single representation, which is the eigenfunction solution for the corresponding geometry. Besides, each solution is used as a reference solution in many studies. However, mutual coupling

calculations in this domain has severe convergence issues especially for electrically large lateral separations between the source and observation points. Therefore, several techniques are used to improve their efficiency and accuracy. On the other hand, in the spatial domain, more than one representation is used for both planar and cylindrical geometries based on where each representation yields the most accurate results and where each representation is the most efficient [18], [19].

In this thesis Chapter 3 and 4 present the evaluation of the MoM impedance matrix and the voltage vector entries both in spectral and spatial domains for planar and cylindrical geometries, respectively, in a detailed way. During the evaluation of these entries, encountered difficulties and methods to handle these difficulties as well as several methods to improve both the efficiency and accuracy are explained. Among them a noticeable one is related to the spectral domain mutual coupling calculations for planar structures. Mutual coupling expressions involve the evaluation of infinite double integrals in the spectral domain, which have severe convergence issues. In previous studies [20] and [21], an asymptotic extraction method is applied to these integrals along with some integration formulas to decrease the computation time. As a result, the asymptotic parts of both the impedance matrix and the voltage vector are transformed to finite one-dimensional integral, which are evaluated using a highly specialized commercial package 'International Mathematics and Statistics Library' (IMSL). Note that these 1-D integrals may posses integrable singularities. In Chapter 3, we provide closed-form solutions to these 1-D integrals.

However, due to the limited usage of spectral domain solutions (convergence problems for electrically large geometries), more emphasis is given to the spatial domain calculations both in Chapter 3 and Chapter 4. In the spatial domain calculations the main problem is handling the singularities when two basis functions overlap with each other completely or partially. In this thesis we explain how to treat these singularities for co- and cross-coupling cases as well as probe-basis function interactions using mappings and change of variable methods in a similar fashion to [22]. Besides, apart from the singularity treatments, same change

of variables are used to reduce the order of integrations. Finally, the remaining integrals are numerically calculated using an adaptive Gaussian integration scheme, which increases the number of points adaptively until a level where the convergence of the integral is achieved for a desired accuracy.

Finally these improved methods are incorporated into two different studies to asses their accuracy and efficiency. First study is the investigation of the scan blindness phenomenon for finite arrays of printed dipoles on material coated electrically large circular cylinders, and its comparison with the same type of arrays on planar platforms. Scan blindness phenomenon which is investigated previously for infinite [23]- [24], [25] and finite [4]-[26] printed antenna arrays on planar grounded dielectric slabs, are investigated for cylindrical ones and the results are published in [27]. These foundings are restated in this thesis in Chapter 5.

The second study is a method to reduce the computational time and memory costs of the aforementioned full-wave solution for the analysis of electrically large finite phased arrays of printed dipoles and patches on planar grounded dielectric slabs. In this thesis a generalized forward backward method (GFBM) [28] based on a discrete Fourier transform (DFT) based acceleration algorithm ([8], [9]) is used in order to achieve this goal. The computational complexity of the problem which is originally $O(N_{tot}^2)$ (order of N_{tot}^2) for each iteration can be reduced to $O(N_{tot})$ (N_{tot} is the total number of unknowns) using this method. The result is remarkably fast and accurate as it is shown in Chapter 6.

Chapter 7 concludes this thesis and explains the importance of the work in the view of presented results. In Appendix A some integral formulas are given which are used in this thesis. An $e^{j\omega t}$ time dependence is assumed and suppressed throughout this work.

Chapter 2

The Hybrid MoM/Green's Function Solution

2.1 Introduction

In this chapter a hybrid technique is explained, which is used to analyze the printed circuit structures. This technique is called the hybrid MoM/Green's function method [29]. It is a combination of the conventional Method of Moments (MoM) solution with a special Green's function. The special Green's functions are specific to the medium that is being analyzed and they are given for planar and circularly cylindrical grounded dielectric slabs in Chapter 3 and Chapter 4, respectively. In hybrid MoM/Green's function technique, an electric field integral equation (EFIE), whose kernel is the special Green's functions that include the presence of the dielectric layer(s) (by satisfying the appropriate boundary conditions), is formulated for the unknown equivalent currents, representing the printed elements on the dielectric substrate. These currents are then approximated as a finite sum of known expansion functions multiplied by unknown coefficients. Finally by taking the moments of the approximated integral equation using the same expansion functions as weighting functions (Galerkin's Method), the integral equation is converted into a matrix equation. Coefficients of the expansion

functions are the unknowns in this matrix equation. Once we solve for these unknowns, we can express the current distribution on the dielectric substrate. Formulation of this matrix equation is given in Section 2.2. Calculation of the entries of this matrix can be done in spectral or spatial domains and Section 2.3 explains these methods.

2.2 MoM Formulation

In Figure 2.1(a) and 2.2(a) basic geometries for printed circuit structures are given for planar and cylindrical dielectric slabs, respectively. Although rectangular microstrip patch antennas are given as an example in these figures, any shape of a printed structure can be analyzed using the hybrid MoM/Green's function technique. These antennas are excited by a probe which is assumed to be ideal in the rest of the work. Using the Schelkunoff's surface equivalence principle [30], these geometries can be analyzed using an equivalent problem as illustrated in Figure 2.1(b) and Figure 2.2(b), respectively. In the equivalent problem, conducting patch surfaces are replaced with the equivalent induced surface currents which are unknown and are to be solved via MoM.

In order to write the EFIE, we start by writing the total electric field in free-space denoted as $\vec{E_0}(\vec{r})$, given by

$$\mathbf{E}_0(\mathbf{r}) = \mathbf{E}^i(\mathbf{r}) + \mathbf{E}^s(\mathbf{r})\,. \tag{2.1}$$

In this equation $\mathbf{E}^s(\mathbf{r})$ is the scattered electric field created by the induced surface currents whereas the $\mathbf{E}^i(\mathbf{r})$ is the incident field which can be a plane wave incident on the patch (scattering problem) or a field generated by the probe current density (radiation and/or mutual coupling problem). We are assuming the latter case in this thesis. $\mathbf{E}^s(\mathbf{r})$ and $\mathbf{E}^i(\mathbf{r})$ are formulated using the special Green's function and the corresponding current densities such that

$$\mathbf{E}^i(\mathbf{r}) = \iint_{S_{source}} \underline{\mathbf{G}}(\mathbf{r},\, \mathbf{r}') \cdot \mathbf{J}^i(\mathbf{r}')\, ds' \tag{2.2}$$

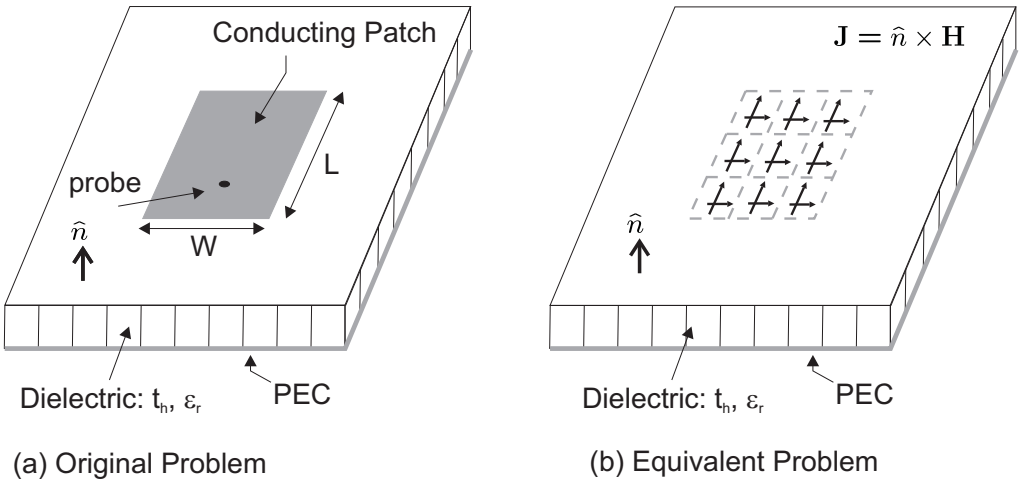

Figure 2.1: A Microstip patch antenna on planar host platform.

$$\mathbf{E}^s(\mathbf{r}) = \iint_{S_{conductor}} \underline{\mathbf{G}}(\mathbf{r},\, \mathbf{r}') \cdot \mathbf{J}^s(\mathbf{r}')\, ds' \tag{2.3}$$

where $\underline{\mathbf{G}}$ is the Green's dyad involving the appropriate components of the electric field related to the surface currents on the conducting patch in the existence of the grounded dielectric slab. These equations are valid for both cylindrical ($\underline{\mathbf{G}}^{\mathrm{cyl}}$) and planar geometries ($\underline{\mathbf{G}}^{\mathrm{pl}}$). Finally in (2.2) and in (2.3) $\mathbf{r}$ and $\mathbf{r}'$ denote the cylindrical or the cartesian coordinate system position vectors according to the geometry that is being analyzed, and the primed coordinates denote the source points whereas unprimed coordinates denote the field points.

Using the boundary condition, that the tangential component of the total electric field is zero on the surface of the conducting patch, one obtains the EFIE given by

$$\hat{n} \times \Big(\mathbf{E}^i(\mathbf{r}) + \mathbf{E}^s(\mathbf{r})\Big) = 0 \quad \text{on} \quad S_{conductor}\,, \tag{2.4}$$

which can be expressed as (using (2.2) & (2.3))

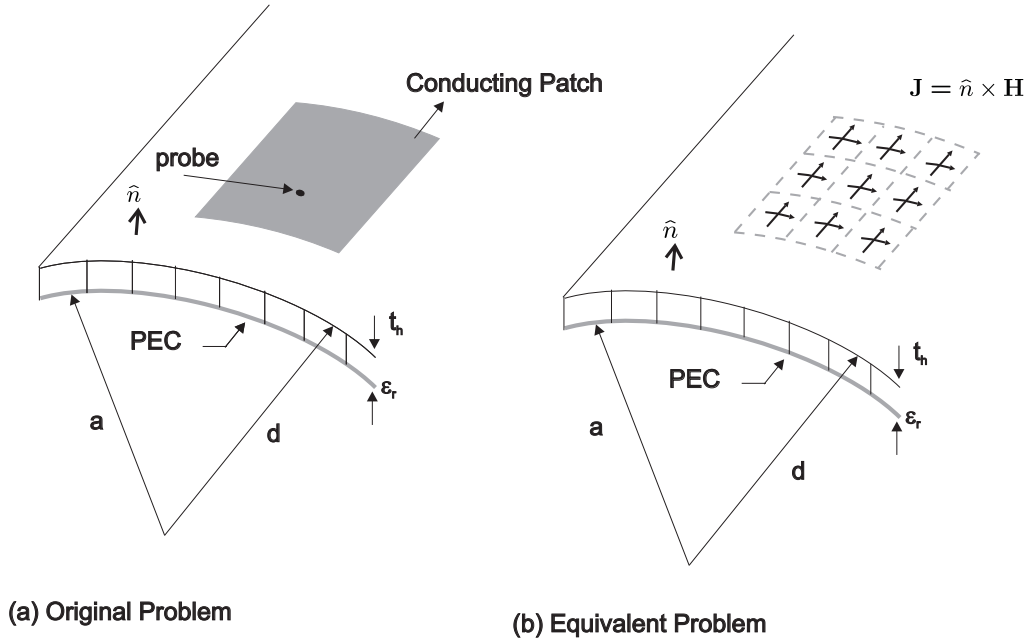

Figure 2.2: A Microstip patch antenna on cylindrical host platform.

$$\iint_{S_{patch}} \hat{n} \times \underline{\mathbf{G}}(\mathbf{r},\, \mathbf{r}') \cdot \mathbf{J}^s(\mathbf{r}')\, ds' = -\iint_{S_{source}} \hat{n} \times \underline{\mathbf{G}}(\mathbf{r},\, \mathbf{r}') \cdot \mathbf{J}^i(\mathbf{r}')\, ds' \qquad (2.5)$$

where $\mathbf{r}$ and $\mathbf{r}' \in S_{conductor}$ and $\hat{n}$ is the unit vector normal to the conductor surface. Then, the MoM procedure starts with the expansion of the unknown surface current in terms of known basis functions

$$\mathbf{J^s}(\mathbf{r}) = \sum_{n=1}^{N} I_n \mathbf{J}_n(\mathbf{r}) \qquad (2.6)$$

where I_n represents the unknown current coefficients which are to be found. Using (2.6) in (2.5) and taking the moments of this integral equation using the same basis functions as weighting functions (Galerkin procedure) we obtain a matrix equation given by

$$\underline{\mathbf{Z}} \cdot \mathbf{I} = \mathbf{V} \qquad (2.7)$$

where

$$Z_{mn} = \iint_{S_m} ds\, \mathbf{J_m}(\mathbf{r}) \cdot \left(\iint_{S_n} ds'\, \underline{\mathbf{G}}(\mathbf{r}, \mathbf{r}') \cdot \mathbf{J_n}(\mathbf{r}') \right) \tag{2.8}$$

$$V_m = - \iint_{S_m} ds\, \mathbf{J}_m(\mathbf{r}) \cdot \mathbf{E}^i(\mathbf{r})\,. \tag{2.9}$$

Z_{mn} is the mutual coupling between m^{th} and n^{th} basis functions. (2.9) is a general equation for the voltage vector. Specifically for a radiation problem with an ideal probe excitation it can be written as

$$V_m = - \iint_{S_m} ds\, \mathbf{J_m}(\mathbf{r}) \cdot \underline{\mathbf{G}}^u_{\mathrm{n}}(\mathbf{r}) \tag{2.10}$$

where $\underline{\mathbf{G}}^u_{\mathrm{n}}$ represents a modified version of the special Green's dyad involving the normal components of the electric field related to the surface currents on the conducting patch as

$$\underline{\mathbf{G}}^u_{\mathrm{n}} = \int_0^d \underline{\mathbf{G}}_{\mathrm{n}}\, dz\,, \tag{2.11}$$

with $\underline{\mathbf{G}}_{\mathrm{n}}$ representing the normal components of Green's function for either the cylindrical ($\underline{\mathbf{G}}^{\mathrm{cyl}}_{\mathrm{n}}$) or planar ($\underline{\mathbf{G}}^{\mathrm{pl}}_{\mathrm{n}}$) geometries. In (2.10) V_m can be considered as a mutual coupling between the m^{th} basis function on the conducting patch and the feeding probe, which is assumed to be a unit current source at the probe position (ideal probe). $\underline{\mathbf{G}}^u_{\mathrm{n}}$ is the special Green's function for this kind of feeding source.

Solution of the matrix equation (2.7) will give us the current coefficients which define the surface current distribution on the conducting patch. The inversion of the MoM matrix can be done using standard routines. For very large arrays iterative methods like generalized forward backward method (GFBM) can be necessary to reduce the computational complexity of this solution (as will be briefly explained in Chapter 6).

There are different types of basis functions used in this thesis for comparison reasons. For planar dielectric slabs 3 types of basis functions are used. These are entire basis (EB) functions (of order m):

$$J_x^{EB}(x,y) = \frac{1}{W}\text{rect}\left(\frac{y-y_n}{W}\right)\sin\left(\frac{m\pi}{L}\left[x-\left(x_n-\frac{L}{2}\right)\right]\right), \tag{2.12}$$

piecewise sinusoidal (PWS) basis functions:

$$J_x^{PWS}(x,y) = \text{rect}\left(\frac{y-y_n}{2y_a}\right)\frac{\sin\left[k_e\left(x_a-|x-x_n|\right)\right]}{2y_a\sin(k_e x_a)}, \tag{2.13}$$

and roof-top (RT) basis functions:

$$J_x^{RT}(x,y) = \frac{1}{2y_a}\text{rect}\left(\frac{y-y_n}{2y_a}\right)\left(1-\frac{|x-x_n|}{x_a}\right). \tag{2.14}$$

where the "rect" function is defined as:

$$\text{rect}(x/2a) = \begin{cases} 1, & |x| < a \\ 0, & \text{otherwise} \end{cases}. \tag{2.15}$$

The EB function is defined over the entire domain of the rectangular conducting patch whereas the PWS and the RT basis functions are sub-sectional basis functions and they are defined over the sub-section

$$\begin{matrix}(x_n-x_a) \le x \le (x_n+x_a) \\ (y_n-y_a) \le y \le (y_n+y_a)\end{matrix}. \tag{2.16}$$

In (2.16), x_a and y_a denote the half-length and the half-width of the basis functions, respectively. x_n and y_n are the center points of the n^{th} basis function. Note that basis functions (2.12)-(2.15) are directed in the $\hat{x}$ direction. The $\hat{y}$-directed basis functions can be written similarly by interchanging the x and y variables. Also note that the EB function is defined over the entire patch surface of length

L and width W. In (2.13) k_e is the effective wavenumber of the substrate given in [31] as

$$k_e = \omega\sqrt{\mu_0\epsilon_e} \tag{2.17}$$

$$\epsilon_e = \frac{\epsilon_r + 1}{2} + \frac{\epsilon_r - 1}{2}\left(1 + \frac{10t_h}{W}\right). \tag{2.18}$$

For cylindrical dielectric slabs only PWS basis functions are considered. $\hat{z}$ and ϕ-directed PWS basis functions are given by

$$J_n^z(z,\phi) = \text{rect}\left(\frac{\mathrm{d}\phi - \mathrm{d}\phi_n}{2rl_a}\right)\frac{\sin\left[k_e\left(z_a - |z - z_n|\right)\right]}{2rl_a\sin\left(k_e z_a\right)} \tag{2.19}$$

$$J_n^\phi(z,\phi) = \text{rect}\left(\frac{z - z_n}{2z_a}\right)\frac{\sin\left[k_e\left(rl_a - |\mathrm{d}\phi - \mathrm{d}\phi_n|\right)\right]}{2z_a\sin\left(k_e rl_a\right)}, \tag{2.20}$$

respectively, where z_a and rl_a denote the half-length and the half-width of the $\hat{z}$-directed basis functions, respectively. These basis functions are located at (z_n, ϕ_n) and they are sinusoidal in the direction of current and constant in the orthogonal direction.

2.3 Spectral and Spatial Domain Methods

Equations (2.8) and (2.9) are two spatial domain representations of the impedance matrix and voltage vector entries, which involve the special Green's functions in the spatial domain. However, analytically exact expressions for the Green's functions which include the effects of planar and cylindrical dielectric slabs are available only in the spectral domain. Therefore, in the spatial domain these Green's functions are represented as the inverse Fourier transform (IFT) of their spectral domain counterparts, and the MoM matrix and the voltage vector entries are given by

$$Z_{mn} = \iint_{S_m} ds\, \mathbf{J}_m(x,y) \cdot \Big[\iint_{S_n} ds' \Big(\iint_{\infty} dk_y\, dk_x\, \underline{\tilde{\mathbf{G}}}(k_x,k_y) e^{jk_x(x-x')} e^{jk_y(y-y')} \Big) \cdot \mathbf{J}_n(x',y') \Big] \quad (2.21)$$

and

$$V_m = -\iint_{S_m} ds\, \Big(\iint_{\infty} dk_y\, dk_x\, \underline{\tilde{\mathbf{G}}}_{\mathrm{n}}(k_x,k_y) e^{jk_x(x_p-x)} e^{jk_y(y_p-y)} \Big) \cdot \mathbf{J}_m(x,y)\,, \quad (2.22)$$

respectively for a planar geometry. In (2.21) and (2.22) $\underline{\tilde{\mathbf{G}}}$ and $\underline{\tilde{\mathbf{G}}}_{\mathrm{n}}$ represent the appropriate components of the spectral domain Green's function, $\mathbf{J}_m$ and $\mathbf{J}_n$ are the same type of basis functions chosen from the list of basis functions discussed in the previous section. $\mathbf{J}_m$ and $\mathbf{J}_n$ are centered at $(x_m,\, y_m)$ and $(x_n,\, y_n)$, respectively. Finally $(x_p,\, y_p)$ denotes the coordinates of the probe feeding the microstrip patch antenna. However, in (2.21) and (2.22) the IFT of the spectral domain Green's function can not be taken, since $\underline{\tilde{\mathbf{G}}}$ and $\underline{\tilde{\mathbf{G}}}_{\mathrm{n}}$ are not absolutely integrable. Therefore, in (2.21) and (2.22) first the order of integrals are changed by taking the finite integrals inside the IFT integrals. Then these finite integrals are evaluated in closed-form by recognizing the Fourier transforms (FT) of $\mathbf{J}_m$ and $\mathbf{J}_n$. As a results (2.21) and (2.22) become

$$Z_{mn} = \iint_{\infty} dk_x\, dk_y\, \tilde{\mathbf{J}}^*_m(k_x,k_y) \cdot \underline{\tilde{\mathbf{G}}}(k_x,k_y) \cdot \tilde{\mathbf{J}}_n(k_x,k_y) \quad (2.23)$$

and

$$V_m = -\iint_{\infty} dk_x\, dk_y\, \tilde{\mathbf{J}}_m(k_x,k_y) \cdot \underline{\tilde{\mathbf{G}}}_{\mathrm{n}}(k_x,k_y) e^{jk_x x_p} e^{jk_y y_p} \quad (2.24)$$

which are called the spectral domain representation of the MoM matrix and voltage vector entries. Note that $\mathbf{J}_m$ and $\mathbf{J}_n$ should be chosen carefully so that their FT, denoted by $\tilde{\mathbf{J}}_m$ and $\tilde{\mathbf{J}}_n$ (with their complex conjugates $\tilde{\mathbf{J}}^*_m$, $\tilde{\mathbf{J}}^*_n$), will make the integrands of (2.23) and (2.24) absolutely integrable.

For cylindrical geometries, equations (2.23) and (2.24) are written as (except the factor $1/2\pi$)[32]

$$Z_{mn} = \sum_{n=-\infty}^{\infty} \left\{ \int_{\infty}^{\infty} \tilde{\mathbf{J}}_m^*(n,\xi) \underline{\tilde{\mathbf{G}}}(n,\xi) \tilde{\mathbf{J}}_n(n,\xi)\, d\xi \right\} \tag{2.25}$$

$$V_m = \sum_{n=-\infty}^{\infty} \left\{ \int_{-\infty}^{\infty} \tilde{\mathbf{J}}_m^*(n,\xi) \underline{\tilde{\mathbf{G}}}_{\mathrm{n}}(n,\xi)\, d\xi \right\} . \tag{2.26}$$

Although the spectral domain method saves us from the integration along the domain of the basis and testing functions and automatically handles the singularity problem, it is extremely inefficient for small basis functions and large separations. Integrands in (2.23) and (2.24) are slowly convergent and highly oscillatory especially for small basis functions and large separations. This is even worse for cylindrical geometries where (2.25) and (2.26) are used. Because of the need for efficient solvers for electrically large structures, there are efficient spatial domain methods developed by Barkeshli et al. [22] and Erturk et al. [33] for planar and cylindrical dielectric slabs, respectively. These methods utilize some high frequency based asymptotic approximations in order to calculate the Green's function representations in the spatial domain efficiently.

2.4 Array Geometry

In this subsection we present several geometries (Fig. 2.3 and Fig. 2.4) where the hybrid MoM/Green's function technique is used. Fig. 2.3(a) and (b) show the geometries of finite, periodic arrays of $(2N+1) \times (2M+1)$ axially ($\hat{z}$-directed) and circumferentially ($\hat{\phi}$-directed) oriented printed dipoles, respectively. The arrays are mounted on the dielectric-air interface of dielectric coated, perfectly conducting, circular cylinders, which are assumed to be infinitely long along the z-direction. The coated cylinders have an inner radius denoted by a, outer radius denoted by d, and hence the coating thickness $t_h = d - a$. The relative permittivity of the coating is $\epsilon_r > 1$. The geometry of a finite, planar, periodic array of $(2N+1) \times (2M+1)$ printed dipoles is also given in Fig. 2.3(c). In all three geometries, the dipoles are assumed to be center-fed with infinitesimal generators with impedance Z_T as depicted in Fig. 2.3(d). Each dipole has a length L, width

W, and is uniformly spaced from its neighbors by distances $d_{rl} = d\Delta\phi$ and d_z in the $rl-$ ($rl = d\phi$) and $z-$directions, respectively. Similarly for the planar case, each dipole is uniformly spaced from its neighbors by distances d_y and d_z in the $y-$ and $z-$directions, respectively. Similar to the the dipole array case, microstrip patch antenna arrays of $(2N+1)\times(2M+1)$ rectangular patch antennas on cylindrical and planar grounded dielectric slabs are depicted in Fig. 2.4 (a) and (b), respectively. These antennas are excited with coaxial-probes which are modeled as ideal probes.

In order to analyze these structures, which are shown in Fig. 2.3 and Fig. 2.4, we developed a general code which implements MoM in spectral and spatial domains (which is selected by the user). This code is fully capable of simulating these geometries with arbitrary parameters. Key features of our code are:

(i) Several types of basis functions are supported in the modeling of patch surface currents. For the planar geometries entire basis functions (2.12), PWS basis functions (2.13) and RT basis functions (2.14) are all available in the spectral domain. In the spatial domain, basis function selection is limited to PWS and RT basis functions. For the cylindrical geometries the only available type is PWS basis functions (2.19) both in the spectral and spatial domain solutions.

(ii) User selects the number of sub-domains or the number of modes in the orthogonal directions which is identical on each element (uniform array). Virtually there is no limit to how dense the discretization can be. However the accuracy of the solution is obviously limited by the accuracy of the Green's function representations.

(iii) For these types of geometries the impedance matrix is a block toeplitz matrix with toeplitz blocks. By exploiting these properties the fill-time of the matrix is reduced tremendously.

(iv) Our code can simulate a single antenna or an arbitrarily sized array of antennas. However only the sub-domain basis functions (PWS and RT basis functions) can be used for an array of antennas.

(v) After the solution of current coefficients several antenna and antenna array performance metrics can be calculated such as input impedance of a single antenna, active reflection coefficient of an element of the array, active element gain patterns.

(vi) The code features a frequency sweep option where start and stop frequencies and the step size can be selected. In the simulation of a single antenna, feed position sweep option is also available.

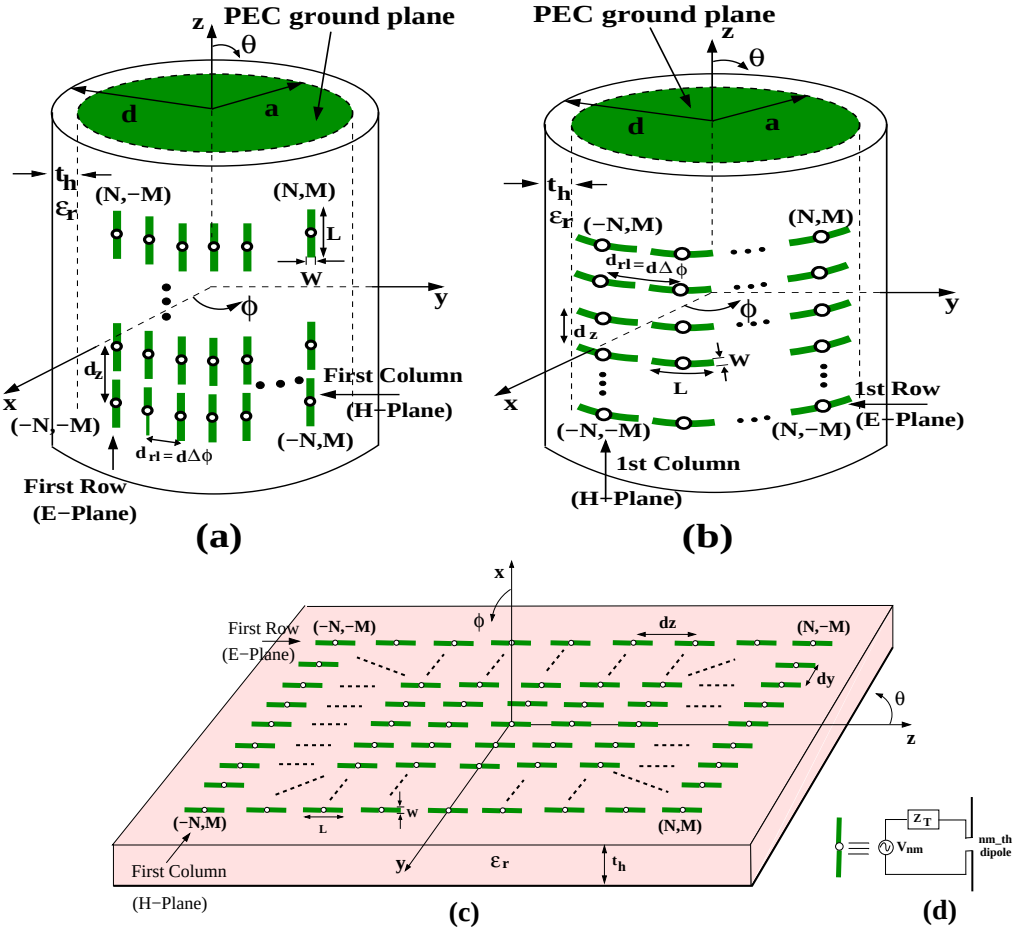

Figure 2.3: Geometries of periodic arrays of $(2N+1)\times(2M+1)$ (a) axially, (b) circumferentially oriented printed dipoles on dielectric coated, electrically large circular cylinders. (c) Geometry of a periodic, planar array of $(2N+1)\times(2M+1)$ printed dipoles. (d) Dipole connected to an infinitesimal generator with a voltage V_{nm} and a terminating impedance Z_T.

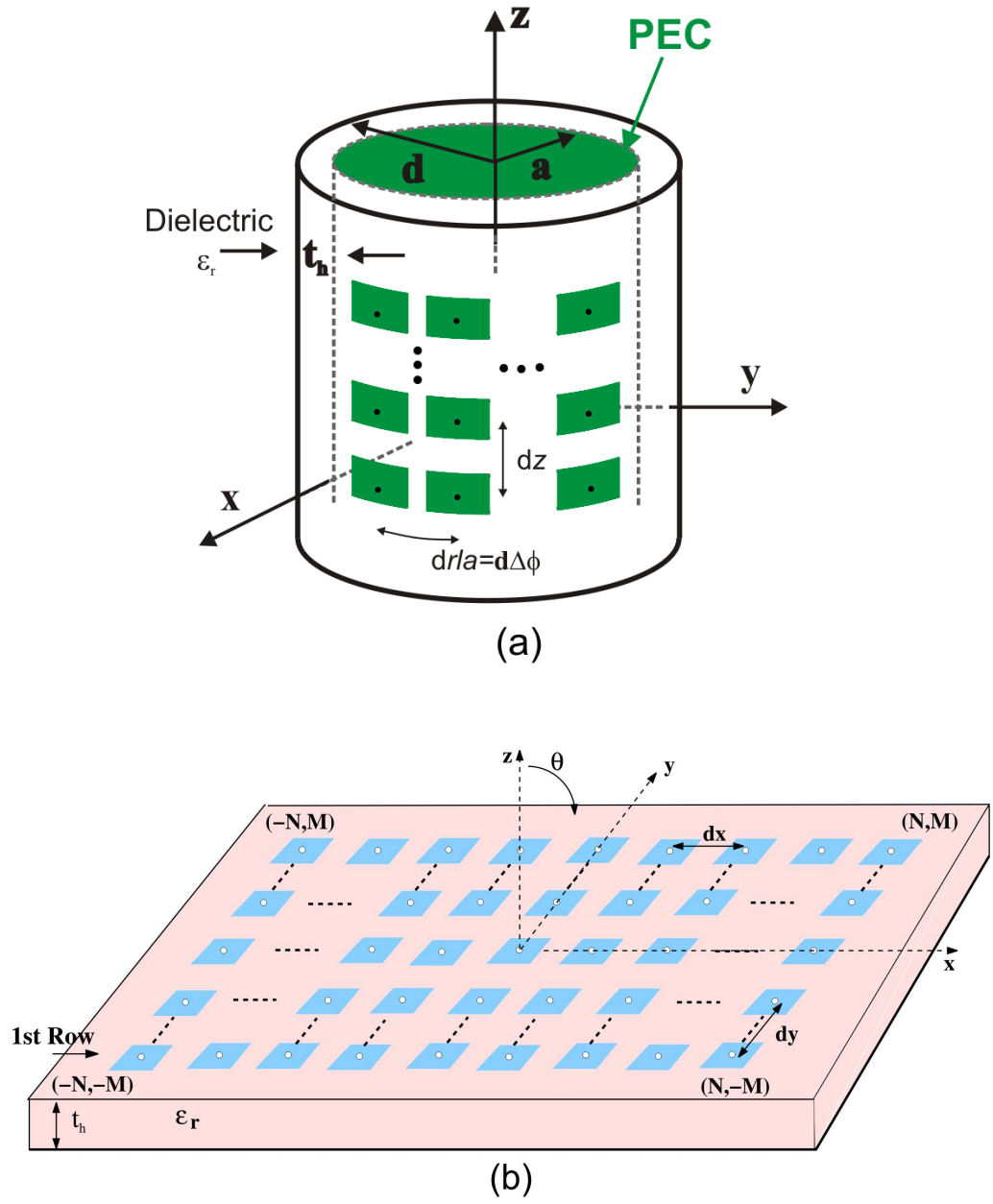

Figure 2.4: (a) Geometry of periodic array of $(2N+1) \times (2M+1)$ microstrip rectangular patch antennas on a dielectric coated, electrically large circular cylinder. (b) Geometry of a periodic, planar array of $(2N+1) \times (2M+1)$ microstrip rectangular patch antennas on a grounded dielectric slab.

Chapter 3

Green's Function Representations for Planar Grounded Dielectric Slab

3.1 Introduction

In the previous chapter spectral and spatial domain methods in the calculation of MoM matrix and voltage vector entries are explained. This chapter gives a detailed explanation on the Green's function representations of planar grounded dielectric slab for spectral and spatial domain methods. There are some established formulations for these functions in the literature which will be restated in this chapter. Spectral domain expressions for the planar geometries will be presented in Section 3.2. Our improvements in the spectral domain for the calculation of self and mutual couplings as well as voltage vector entries for ideal probe excitation using roof-top sub-sectional basis functions are explained in detail in Section 3.3. Briefly, using asymptotic extraction techniques convergence of the numerical integration is accelerated and closed-form expressions are developed for the asymptotic part of the integral. Consequently, the final form of the spectral domain solution becomes faster and more accurate compared to the previous

studies. In Section 3.4, we briefly explain the spatial domain expressions of the Green's function representations for planar geometries. These expressions require the calculation of two double integrals for the MoM matrix entries and a single double integral for the voltage vector entries. Spatial domain calculation of the mutual coupling between two basis functions must be carried out with extra care if they overlap because of the $1/s$ type singularity where s is the lateral separation between the source and field points. We present an asymptotic solution to this problem in section 3.5. Using a proper change of variables, order of these integrals can be reduced to one by taking one of the integrals in closed-form which is explained in detail in Section 3.6. As a result computational burden is reduced in the computation of these integrals.

3.2 Spectral Domain Green's Function for Planar Grounded Dielectric Slabs

Spectral domain Green's function representation for the planar grounded dielectric slab geometries can be expressed in the form of [21], [31]:

$$\tilde{G}_{xx}(k_x,k_y) = -j\frac{Z_0}{k_0}\frac{(\epsilon_r k_0^2 - k_x^2)k_2 + jk_1(k_0^2 - k_x^2)\tan(k_1 d)}{T_e T_m}\tan(k_1 d) \tag{3.1}$$

$$\tilde{G}_{yy}(k_x,k_y) = -j\frac{Z_0}{k_0}\frac{(\epsilon_r k_0^2 - k_y^2)k_2 + jk_1(k_0^2 - k_y^2)\tan(k_1 d)}{T_e T_m}\tan(k_1 d) \tag{3.2}$$

$$\tilde{G}_{yx}(k_x,k_y) = \tilde{G}_{xy}(k_x,k_y) = j\frac{Z_0}{k_0}\frac{k_x k_y \tan(k_1 d)\,[k_2 + jk_1\tan(k_1 d)]}{T_e T_m} \tag{3.3}$$

$$\tilde{G}_{xz}(k_x,k_y) = \tilde{G}_{zx}(k_x,k_y) = j\frac{Z_0}{k_0}\frac{k_x k_2 \tan(dk_1)}{k_1 T_m} \tag{3.4}$$

$$\tilde{G}_{yz}(k_x,k_y)=\tilde{G}_{zy}(k_x,k_y)=j\frac{Z_0}{k_0}\frac{k_yk_2\tan(dk_1)}{k_1T_m} \tag{3.5}$$

with

$$\begin{aligned}
T_e &= k_1+jk_2\tan(k_1d) && (3.6)\\
T_m &= \epsilon_rk_2+jk_1\tan(k_1d) && (3.7)\\
k_1^2 &= \epsilon_rk_0^2-k_x^2-k_y^2, \qquad \mathrm{Im}(k_1)\leq 0 && (3.8)\\
k_2^2 &= k_0^2-k_x^2-k_y^2, \qquad \mathrm{Im}(k_2)\leq 0 && (3.9)\\
\beta^2 &= \sqrt{k_x^2+k_y^2} && (3.10)\\
k_0 &= \omega\sqrt{\mu_0\epsilon_0} && (3.11)
\end{aligned}$$

where $Z_0=\sqrt{\frac{\mu_0}{\epsilon_0}}$ is the intrinsic impedance of the free space. Note that $\tilde{G}_{zz}(k_x,k_y)$ is not used in this study.

3.3 Closed Form Solution to the Asymptotic Part of the MoM Impedance Matrix and the MoM Excitation Vector

Spectral domain MoM solution to the EFIE given by (2.23) requires the computation of the spectral domain integrals which has to be done numerically. These double integrals have limits extended to infinity. Unfortunately, the integrands have slowly convergent and highly oscillatory behaviors which make the computation of the impedance matrix elements as the most time consuming part of the MoM solution. Besides, such behaviors can create accuracy problems. These problems also occur in the computation of the excitation vector elements. Thus, various techniques have been developed related to the spectral domain evaluation of the matrix and the excitation vector entries [34]-[35]. Among them, in [20] and [21], the authors have successfully derived an analytical technique for the fast and accurate evaluation of the asymptotic part of the impedance matrix when triangular edge mode and roof-top subdomain basis functions are used in the spectral domain MoM solution for printed narrow strips and antennas. Basically, they

provide an analytical transformation from an infinite double integral to a finite one-dimensional (1-D) integral for the asymptotic part of the impedance matrix, thereby reducing the CPU time dramatically and improving the accuracy regardless of the lateral separation between the basis and testing functions. Recently, the same method has been applied to the MoM excitation vector for probe-fed planar microstrip antennas [35].

In all these three studies ([20], [21] and [35]), the resulting 1-D finite integrals are computed using the 'International Mathematics and Statistics Library (IMSL)' subroutines DQDAGP (if there is a singularity) or DQDAGS, which are high-quality adaptive integral routines. Unfortunately, these routines are highly specialized and may not be available on all platforms. Moreover, using standard numerical integration techniques instead of these IMSL routines may yield accuracy problems. In subsection 3.3.1 we will provide closed-form results for these 1-D integrals. Consequently, the asymptotic parts of both the impedance matrix and the excitation vector are evaluated completely in closed-form, which results a further reduction in the CPU time and a further improvement in the accuracy for the evaluation of the MoM matrix and the excitation vector entries. Besides, these closed-form expressions eliminate the need for such highly specialized subroutines for this problem. In order to asses the accuracy of the closed-form expressions several numerical results are given in subsection 3.3.2.

3.3.1 Formulation

In the spectral domain MoM solution of printed structures on planar grounded dielectric slabs, using (2.23) and employing the asymptotic extraction technique, the impedance matrix elements can be expressed in the form of

$$Z_{mn}^{pq} = -\frac{1}{4\pi^2}\int_{-\infty}^{\infty}\int_{-\infty}^{\infty}\tilde{J}_m^{p^*}(k_x,k_y)\left[\tilde{G}_{pq}(k_x,k_y)-\tilde{G}_{pq}^{\infty}(k_x,k_y)\right]\tilde{J}_n^{q}(k_x,k_y)dk_xdk_y$$

$$-\frac{1}{4\pi^2}\int_{-\infty}^{\infty}\int_{-\infty}^{\infty}\tilde{J}_m^{p^*}(k_x,k_y)\tilde{G}_{pq}^{\infty}(k_x,k_y)\tilde{J}_n^{q}(k_x,k_y)dk_xdk_y \tag{3.12}$$

($p = x$ or y, and $q = x$ or y) where Z_{mn}^{pq} represents the self and mutual interactions between the roof-top sub-domain current basis functions J_m^p and J_n^q. In (3.12) $\tilde{J}_m^p$ is the Fourier transform of the p-directed basis function (i.e., J_m^p). Basically, when $p = x$ we have

$$\tilde{J}_m^x = \frac{8}{\Delta x\Delta y}\frac{\sin^2\left(k_x\frac{\Delta x}{2}\right)}{k_x^2}\frac{\sin\left(k_y\frac{\Delta y}{2}\right)}{k_y}e^{-j(k_xx_m+k_yy_m)} \tag{3.13}$$

and when $p = y$ we have

$$\tilde{J}_m^y = \frac{8}{\Delta x\Delta y}\frac{\sin\left(k_x\frac{\Delta x}{2}\right)}{k_x}\frac{\sin^2\left(k_y\frac{\Delta y}{2}\right)}{k_y^2}e^{-j(k_xx_m+k_yy_m)}. \tag{3.14}$$

Also in (3.12) $\tilde{J}_m^{q^*}$ is the complex conjugate of the Fourier transform of the q-directed basis function and finally $\tilde{G}_{pq}$ is the appropriate dyadic Green's function component in the spectral domain (given in (3.1)-(3.3)) with $\tilde{G}_{pq}^{\infty}$ being its asymptotic value for large $\beta = \sqrt{k_x^2+k_y^2}$ values, given by [21]

$$\tilde{G}_{xx}^{\infty}(k_x,k_y) = -j\frac{Z_0}{k_0}\left\{\frac{k_0^2}{2\beta}-\frac{k_x^2}{(\epsilon_r+1)\beta}\right\} \tag{3.15}$$

$$\tilde{G}_{yy}^{\infty}(k_x,k_y) = -j\frac{Z_0}{k_0}\left\{\frac{k_0^2}{2\beta}-\frac{k_y^2}{(\epsilon_r+1)\beta}\right\} \tag{3.16}$$

$$\tilde{G}_{xy}^{\infty}(k_x,k_y) = \tilde{G}_{yx}^{\infty}(k_x,k_y) = j\frac{Z_0}{k_0}\frac{k_xk_y}{(\epsilon_r+1)\beta}. \tag{3.17}$$

In a similar fashion, the MoM excitation vector elements (for probe-fed structures) are expressed as

$$V_m^q = \frac{1}{4\pi^2}\int_{-\infty}^{\infty}\int_{-\infty}^{\infty}\left[\tilde{G}_{zq}(k_x,k_y)-\tilde{G}_{zq}^{\infty}(k_x,k_y)\right]\tilde{J}_m^q(k_x,k_y)e^{j(k_x x^p+k_y y^p)}dk_x dk_y$$

$$+\frac{1}{4\pi^2}\int_{\infty}^{\infty}\int_{\infty}^{\infty}\tilde{G}_{zq}^{\infty}(k_x,k_y)\tilde{J}_m^q(k_x,k_y)e^{j(k_x x^p+k_y y^p)}dk_x dk_y \tag{3.18}$$

where (x^p, y^p) is the coaxial probe attachment position on the patch surface and $\tilde{G}_{zq}$ is appropriate dyadic Green's function component in the spectral domain ((3.4) and (3.5)) with $\tilde{G}_{zq}^{\infty}$ being its asymptotic value for large β values given by [35]

$$\tilde{G}_{zx}^{\infty} = -\frac{Z_0}{k_0}\frac{k_x}{\beta(1+\epsilon_r)} \tag{3.19}$$

$$\tilde{G}_{zx}^{\infty} = -\frac{Z_0}{k_0}\frac{k_y}{\beta(1+\epsilon_r)}\,. \tag{3.20}$$

In the first terms of (3.12) and (3.18), the infinite double integrals converge rapidly to zero. However, the second terms in (3.12) and (3.18) (called as the asymptotic part of the impedance matrix element and the MoM excitation vector element) also contain the infinite double integrals which exhibit slowly convergent and highly oscillatory behavior. Therefore, in [20] and [21] an analytical technique has been derived for the fast and accurate evaluation of the asymptotic part of the impedance matrix elements, and then this technique has been applied to the MoM excitation vector elements in [35]. Consequently, the infinite double integrals in the asymptotic part of (3.12) and (3.18) are analytically transformed to 1-D integrals given by

$$Z_{mn}^{xx^{Asy}} = -\frac{j}{\pi^2}\left(\frac{8}{\Delta x\Delta y}\right)^2\left\{-\frac{k_0^2}{2}I_{mn}^{xx^a}+\frac{1}{\epsilon_r+1}I_{mn}^{xx^b}\right\} \tag{3.21}$$

$$Z_{mn}^{xy^{Asy}} = Z_{mn}^{yx^{Asy}} = \frac{j}{\pi^2}\frac{Z_0}{k_0}\left(\frac{64}{\Delta x^2\Delta y^2}\right)\frac{1}{\epsilon_r+1}I_{mn}^{xy} \tag{3.22}$$

$$V_m^{x^{Asy}} = -\frac{j}{\pi^2}\frac{Z_0}{k_0}\left(\frac{8}{\Delta x \Delta y}\right)\frac{1}{\epsilon_r+1} I_m^{zx} \tag{3.23}$$

where

$$I_{mn}^{xx^a} = \frac{1}{\pi}\int_{-2\Delta x}^{2\Delta x} \mathcal{A}(\chi - x_s)\,\Im_a(\chi) d\chi \tag{3.24}$$

$$I_{mn}^{xx^b} = \frac{1}{\pi}\int_{-2\Delta x}^{2\Delta x} \mathcal{A}(\chi - x_s)\,\Im_b(\chi) d\chi \tag{3.25}$$

$$I_{mn}^{xy} = \frac{1}{\pi}\int_{-\frac{3\Delta x}{2}+x_s}^{\frac{3\Delta x}{2}+x_s} \mathcal{B}(\chi)\,T(\chi - x_s) d\chi \tag{3.26}$$

$$I_m^{zx} = -\frac{1}{\pi}\int_{x_A-\Delta x}^{x_A+\Delta x} C(\chi)\,\Gamma(\chi - x_A) d\chi \quad . \tag{3.27}$$

$\mathcal{A}(\chi - x_s)$, $\Im_a(\chi)$, $\Im_b(\chi)$, $\mathcal{B}(\chi)$, $T(\chi)$, $C(\chi)$ and $\Gamma(\chi)$ are the integrals evaluated in closed-form in [21] and [35], and they are given by (A.1) through (A.7), respectively, in Appendix A. Similar expressions can be formed for $I_{mn}^{yy^a}$, $I_{mn}^{yy^b}$, I_{mn}^{yx} and I_{mn}^{zy} by interchanging $\Delta x \leftrightarrow \Delta y$, $x_s \leftrightarrow y_s$ and $x_A \leftrightarrow y_A$ where x_s and y_s are the lateral separation between the basis and testing functions (i.e., $x_s = x_m - x_n$; $y_s = y_m - y_n$), and x_A and y_A are the separation between the basis function under analysis and the probe location (i.e., $x_A = x_p - x_m$; $y_A = y_p - y_m$).

In [20], [21] and [35], the 1-D integrals given in (3.24)-(3.27) were computed numerically using the the International Mathematics and Statistics Library (IMSL) subroutines. During the computation of these integrals, if there is a singularity at the integration interval, then the IMSL routine DQDAGP was used, which can handle interior and endpoint singularities. If there is no singularity, the IMSL routine DQDAGS was used. Unfortunately, these routines are highly specialized and may not be available on all platforms. Besides, it is observed that using standard numerical integration techniques instead of these IMSL routines yields accuracy problems. In this thesis we are providing closed-form expressions. The key steps in arriving these closed-form expressions are:

(i) The analytic evaluation of the following type integrals:

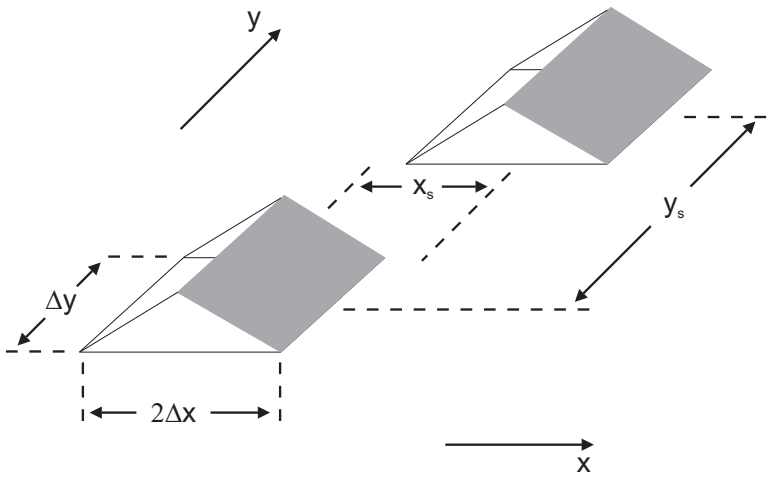

Figure 3.1: A couple of $\hat{x}$-directed RT basis functions

$$f_i(a, x_1, x_2) = \int_{x_1}^{x_2} x^i \sqrt{x^2 + a^2}\, dx \ , \tag{3.28}$$

$$F_i(a, x_1, x_2, x_s) = \int_{x_1}^{x_2} x^i \sqrt{(x - x_s)^2 + a^2}\, dx \ , \tag{3.29}$$

$$g_i(a, x_1, x_2) = \int_{x_1}^{x_2} x^i \ln\left(a + \sqrt{x^2 + a^2}\right)\, dx \ , \tag{3.30}$$

$$G_i(a, x_1, x_2, x_s) = \int_{x_1}^{x_2} x^i \ln\left(a + \sqrt{(x - x_s)^2 + a^2}\right)\, dx \ , \tag{3.31}$$

with $i = 0, 1, 2, 3$. Analytical expressions to the results of the integrals (3.28), (3.29), (3.30) and (3.31) are given by (B.1)-(B.4), (B.5)-(B.8), (B.9)-(B.12) and (B.13)-(B.16), in Appendix B. It is important to notice that $F_i(a, x_1, x_2, x_s)$ and $G_i(a, x_1, x_2, x_s)$, are expressed in terms of $f_i(a, x_1, x_2)$ and $g_i(a, x_1, x_2)$, respectively.

(ii) Recognizing that the closed-form expressions to the integrals given by (3.24)-(3.27) can be obtained as a combination of (3.28)-(3.31).

Consequently, the closed-form expressions for the 1-D integrals given by (3.24)-(3.27) are found as follows:

$$
\begin{aligned}
I_{mn}^{xx^a} &= \frac{\pi}{768}\sum_{q=1}^{2}\sum_{p=1}^{3}\sum_{i=0}^{3}\Big\{c_i^{s_1}(\Delta x,\, q)\Big[c_g(p)\, G_i(a_p^{xx}, \chi_{3q-2}^{xx}, \chi_{3q-1}^{xx}, x_s) \\
&\quad + c_f(p)\, F_i(a_p^{xx}, \chi_{3q-2}^{xx}, \chi_{3q-1}^{xx}, x_s)\Big]\Big\} \\
&\quad + \frac{\pi}{768}\sum_{q=1}^{2}\sum_{p=1}^{3}\sum_{i=0}^{3}\Big\{c_i^{s_2}(\Delta x, q)\Big[c_g(p)\, G_i(a_p^{xx}, \chi_{q+1}^{xx}, \chi_{q+2}^{xx}, x_s) \\
&\quad + c_f(p)\, F_i(a_p^{xx}, \chi_{q+1}^{xx}, \chi_{q+2}^{xx}, x_s)\Big]\Big\} \qquad (3.32)
\end{aligned}
$$

$$
\begin{aligned}
I_{mn}^{xx^b} &= \frac{\pi}{16}\sum_{q=1}^{2}\sum_{p=1}^{3}\sum_{i=0}^{1}\Big\{c_i^{s_3}(\Delta x, q)\Big[c_g(p)\, G_i(a_p^{xx}, \chi_{3q-2}^{xx}, \chi_{3q-1}^{xx}, x_s) \\
&\quad + c_f(p)\, F_i(a_p^{xx}, \chi_{3q-2}^{xx}, \chi_{3q-1}^{xx}, x_s)\Big]\Big\} \\
&\quad + \frac{\pi}{16}\sum_{q=1}^{2}\sum_{p=1}^{3}\sum_{i=0}^{1}\Big\{c_i^{s_4}(\Delta x, q)\Big[c_g(p)\, G_i(a_p^{xx}, \chi_{q+1}^{xx}, \chi_{q+2}^{xx}, x_s) \\
&\quad + c_f(p)\, F_i(a_p^{xx}, \chi_{q+1}^{xx}, \chi_{q+2}^{xx}, x_s)\Big]\Big\}\,, \qquad (3.33)
\end{aligned}
$$

$$
\begin{aligned}
I_{mn}^{xy} &= \sum_{q=1}^{4}\sum_{p=1}^{3}\Big\{d^{xy}(q)\Big[c^{xy}(2p-1)\Big(f_0(a_q^{xy}, \chi_p^{xy}, \chi_{p+1}^{xy}) - a_q^{xy} g_0(a_q^{xy}, \chi_p^{xy}, \chi_{p+1}^{xy})\Big) \\
&\quad + c^{xy}(2p)\Big(f_1(a_q^{xy}, \chi_p^{xy}, \chi_{p+1}^{xy}) - a_q^{xy} g_1(a_q^{xy}, \chi_p^{xy}, \chi_{p+1}^{xy})\Big)\Big]\Big\}\,, \qquad (3.34)
\end{aligned}
$$

$$
\begin{aligned}
I_m^{zx} &= g_0(a_1^{zx}, \chi_1^{zx}, \chi_2^{zx}) - g_0(a_2^{zx}, \chi_1^{zx}, \chi_2^{zx}) \\
&\quad - g_0(a_1^{zx}, \chi_2^{zx}, \chi_3^{zx}) \,+\, g_0(a_2^{zx}, \chi_2^{zx}, \chi_3^{zx})\,. \qquad (3.35)
\end{aligned}
$$

In (3.32) and (3.33), the constants and the coefficients are given in Table 3.1 and Table 3.2. Similarly, in (3.34) and (3.35), the constants and the coefficients are given in Tables 3.3-3.5.

$c_0^{s1} = 8\Delta x^3$	$c_0^{s2} = -4\Delta x^3$	$c_0^{s3} = -\frac{\Delta x}{4}$
$c_1^{s1} = 12\Delta x^2(-1)^{q+1}$	$c_1^{s2} = 0$	$c_1^{s3} = \frac{1}{8}(-1)^q$
$c_2^{s1} = 6\Delta x$	$c_2^{s2} = -6\Delta x$	$c_0^{s4} = \frac{\Delta x}{4}$
$c_3^{s1} = (-1)^{q+1}$	$c_3^{s2} = 3\,(-1)^q$	$c_1^{s4} = \frac{3}{8}(-1)^{q+1}$
$a_1^{xx} = y_s + \Delta y$	$c_g(1) = y_s + \Delta y$	$c_f(1) = -1$
$a_2^{xx} = y_s - \Delta y$	$c_g(2) = y_s - \Delta y$	$c_f(2) = -1$
$a_3^{xx} = y_s$	$c_g(3) = -2y_s$	$c_f(3) = 2$

Table 3.1: Constants I

$\chi_1^{xx} = -2\Delta x$
$\chi_2^{xx} = -\Delta x$
$\chi_3^{xx} = 0$
$\chi_4^{xx} = \Delta x$
$\chi_5^{xx} = 2\Delta x$

Table 3.2: Constants II

3.3.2 Numerical Results

To assess the accuracy of the closed-form expressions presented in (3.32)-(3.35) with the related parameters given by Table 3.1-3.5, several numerical results in the form of mutual impedance between two expansion functions and the input impedance of several probe-fed microstrip patch antennas are obtained and compared with the simulation and measurement results available in the literature.

The first numerical example is the duplication of Fig. 2 in [21], where the finite 1-D integrals are compared with the double infinite integrals using $\Delta x = \Delta y = 1$ and $y_s = 2\Delta y$ for $0 \leq x_s \leq 10$ for (3.24) and (3.25), and using $\Delta x = \Delta y = 1$ and $y_s = \frac{3}{2}\Delta y$ for $0 \leq x_s \leq 10$ for (3.26). We also evaluated the same integrals,

$\chi_1^{xy} = -1.5\Delta x + x_s$	$a_1^{xy} = -1.5\Delta y + y_s$	$d^{xy}(1) = -\frac{1}{16}$
$\chi_2^{xy} = -0.5\Delta x + x_s$	$a_2^{xy} = -0.5\Delta y + y_s$	$d^{xy}(2) = \frac{3}{16}$
$\chi_3^{xy} = 0.5\Delta x + x_s$	$a_3^{xy} = 0.5\Delta y + y_s$	$d^{xy}(3) = -\frac{3}{16}$
$\chi_4^{xy} = 1.5\Delta x + x_s$	$a_4^{xy} = 1.5\Delta y + y_s$	$d^{xy}(4) = \frac{1}{16}$

Table 3.3: Constants III

$c^{xy}(1) = -\frac{\pi}{8}(1.5\Delta x - x_s)$	$c^{xy}(4) = \frac{\pi}{4}$	$\chi_1^{zx} = x_p - \Delta x$
$c^{xy}(2) = -\frac{\pi}{8}$	$c^{xy}(5) = \frac{\pi}{8}(1.5\Delta x + x_s)$	$\chi_2^{zx} = x_p$
$c^{xy}(3) = -\frac{\pi}{4}x_s$	$c^{xy}(6) = -\frac{\pi}{8}$	$\chi_3^{zx} = x_p + \Delta x$

Table 3.4: Constants IV

(3.24)- (3.26), using the closed-form expressions. As depicted in Fig. 3.2, excellent agreement is obtained.

As a second example, the mutual interaction between two $\hat{x}$-directed current modes, which are defined to be roof-top functions (2.14), are evaluated along the H-plane (i.e., along the y-axis). These current modes are on a grounded dielectric slab with a thickness, $t_h = 0.057\lambda_0$ (λ_0 is the free-space wavelength) and $\epsilon_r = 2.33$, and the size of each current mode is selected to be $\Delta x = 0.05\lambda_0$ and $\Delta y = 0.025\lambda_0$. Since IMSL routines are highly specialized and are not available on our platforms, we used the standard Gaussian quadrature algorithm in the following way: For the integration limits from $-2\Delta x$ to $2\Delta x$, we divided the integration interval to subintervals with subinterval length being $\Delta x/8$. In each subinterval we used an 8-point Gaussian quadrature algorithm. As seen in Fig. 3.3, we have an excellent agreement both in magnitude and phase except for relatively large separations, where the finite 1-D integration method yields some numerical problems. As a result, we believe this result illustrates the importance of the closed-form expressions that we provide for the 1-D integrals.

$$\boxed{\begin{aligned} a_1^{zx} &= y_p + \tfrac{\Delta y}{2} \\ a_2^{zx} &= y_p - \tfrac{\Delta y}{2} \end{aligned}}$$

Table 3.5: Constants V

The last two numerical examples, shown in Fig. 3.4 and Fig. 3.5, provide the Smith Chart plots of the input impedance of two probe-fed microstrip antennas, where the closed-form expressions for both the impedance matrix and the excitation vector are used. Results are also compared with the previously published results as well as the results of a software package ENSEMBLE [36]. Fig. 3.4 is given for a rectangular microstrip patch antenna on a grounded dielectric slab with $\epsilon_r = 10.2$ and thickness, $t_h = 0.127$ cm. The length of the patch L is 2 cm, the width of the patch W is 3 cm, and the feed is located 1 cm from the long edge (i.e., from the W edge) and 0.65 cm from the short edge (i.e., from the L edge) as explained in [37]. The frequency is varied from 2.2 GHz to 2.4 GHz, and 9 roof-top basis functions are used along the width of the patch. As seen in Fig. 3.4, very good agreement is obtained with both the measured results given in [37] and the results obtained from the ENSEMBLE software [36].

In a similar fashion Fig. 3.5 is given for $W = 39.52$ mm by $L = 49.91$ mm rectangular antenna with a coaxial feed located at $W/2$ from the long side (i.e., from the L edge) and 15.36 mm from the short side (i.e., from the W edge) as depicted in [38]. The antenna is located on a grounded dielectric slab with $\epsilon_r = 2.484$ and $h = 6.3$ mm. The frequency is varied from 1.72 GHz to 2.10 GHz, and 5 roof-top basis functions are used along the length of the patch. Similar to the previous case, very good agreement is obtained with both the measured and the simulated results given in [38] as well as the results obtained from the ENSEMBLE software [36]. Note that to account the self inductance of the probe we added jX_{pr} to the input impedance given by

$$X_{pr} = -\frac{\eta k t_h}{2\pi}\left[ln\left(\frac{kd_p}{4}\right) + 0.577\right] \tag{3.36}$$

where η is the intrinsic impedance of the dielectric medium, k is the wave number

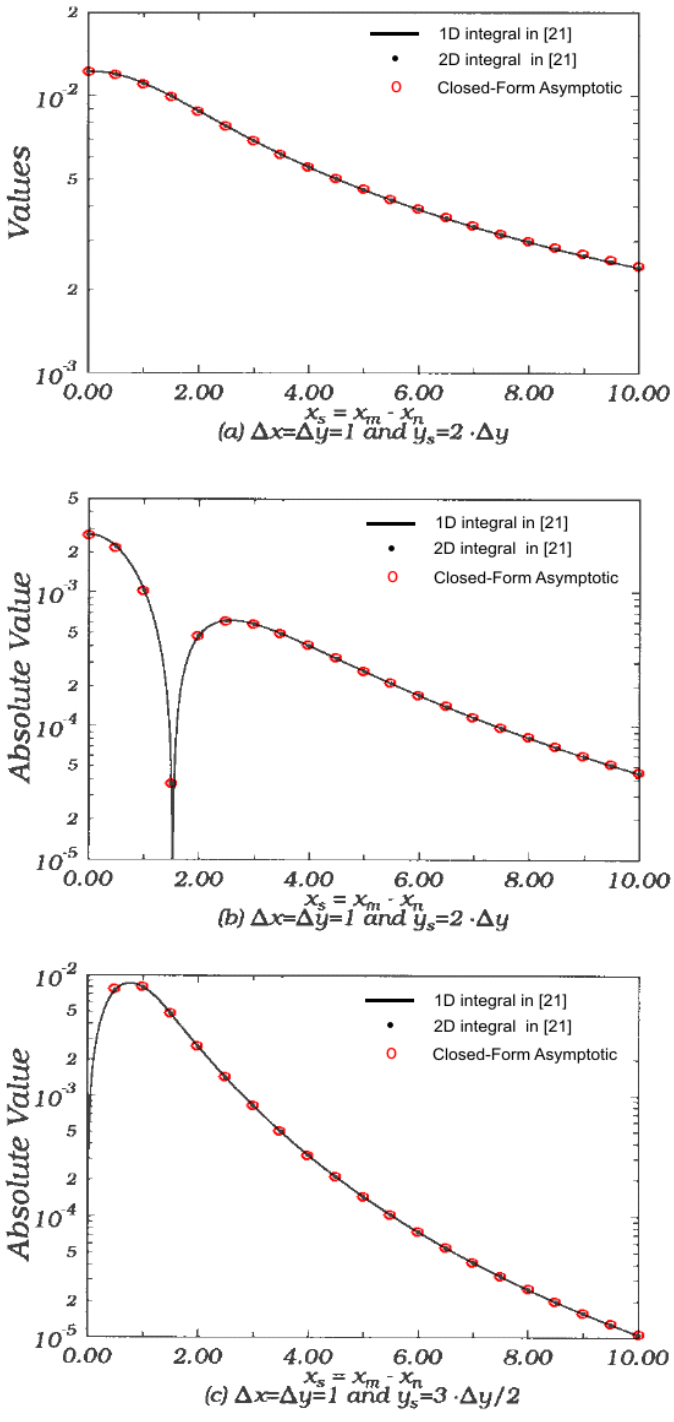

Figure 3.2: Comparison among the infinite 2-D integral, the finite 1-D integral and the closed-form expressions.

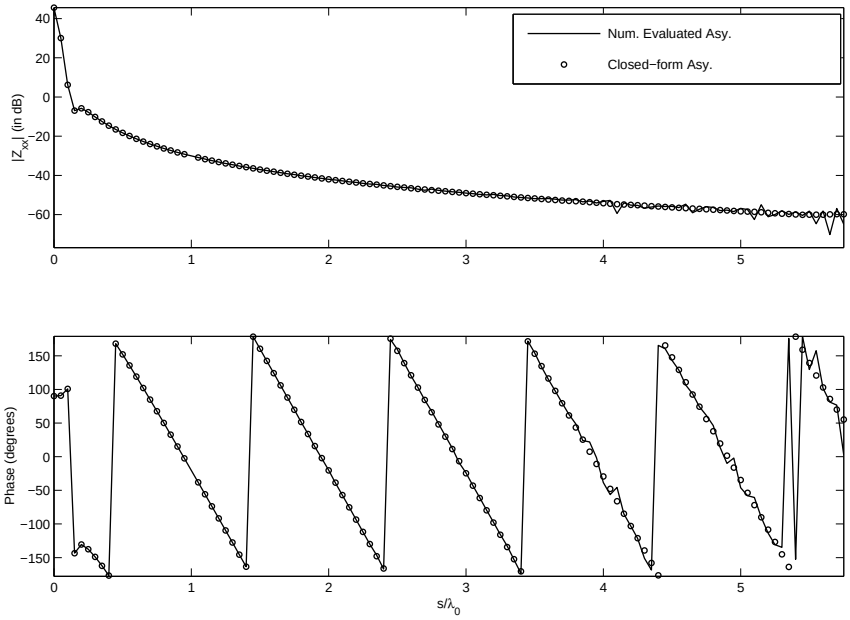

Figure 3.3: Magnitude and phase of mutual impedance Z_{12}^{xx} between two identical $\hat{x}-$directed current modes on a $t_h = 0.057\lambda_0$ thick grounded dielectric slab with $\epsilon_r = 2.33$.

of the dielectric medium, d_p is the diameter of the feed probe and t_h is the thickness of the substrate [39].

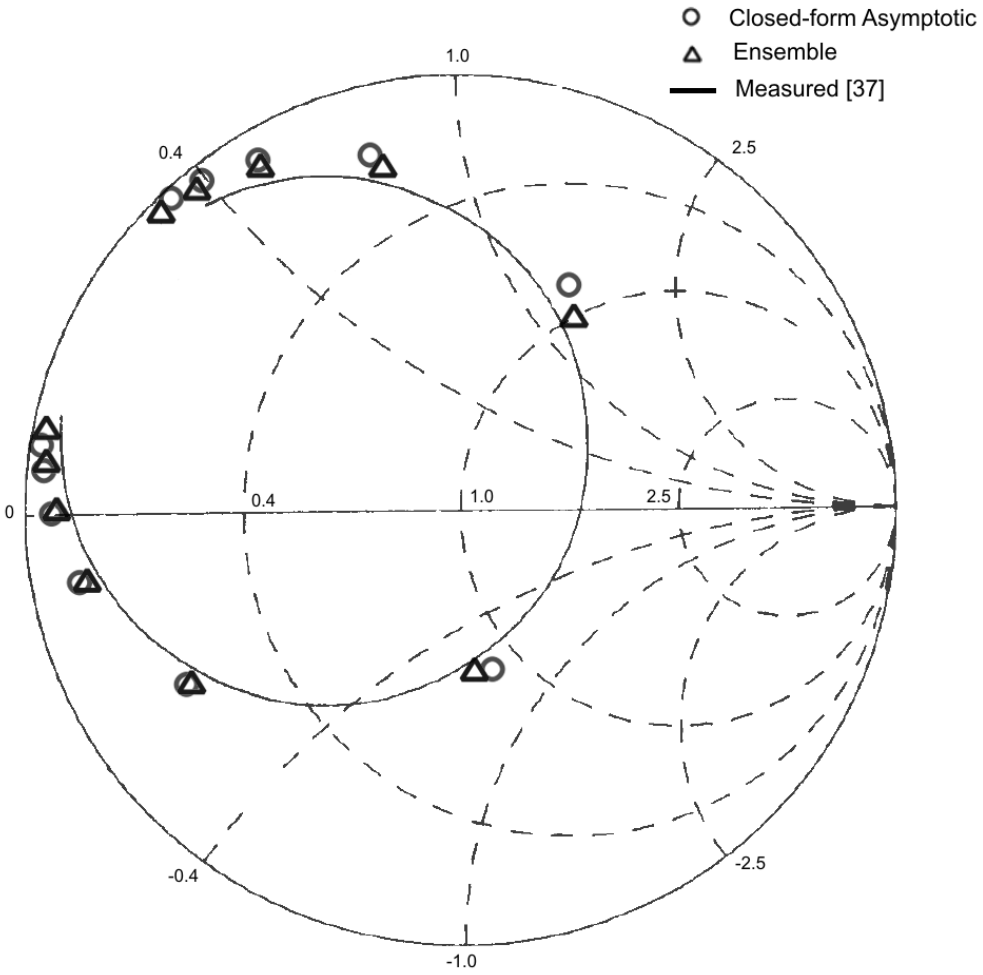

Figure 3.4: Input impedance data of a probe-fed, $L = 2$ cm by $W = 3$ cm rectangular antenna on a $h = 0.127$ cm thick grounded dielectric slab with $\epsilon_r = 10.2$. Frequency = 2.2-2.4 GHz.

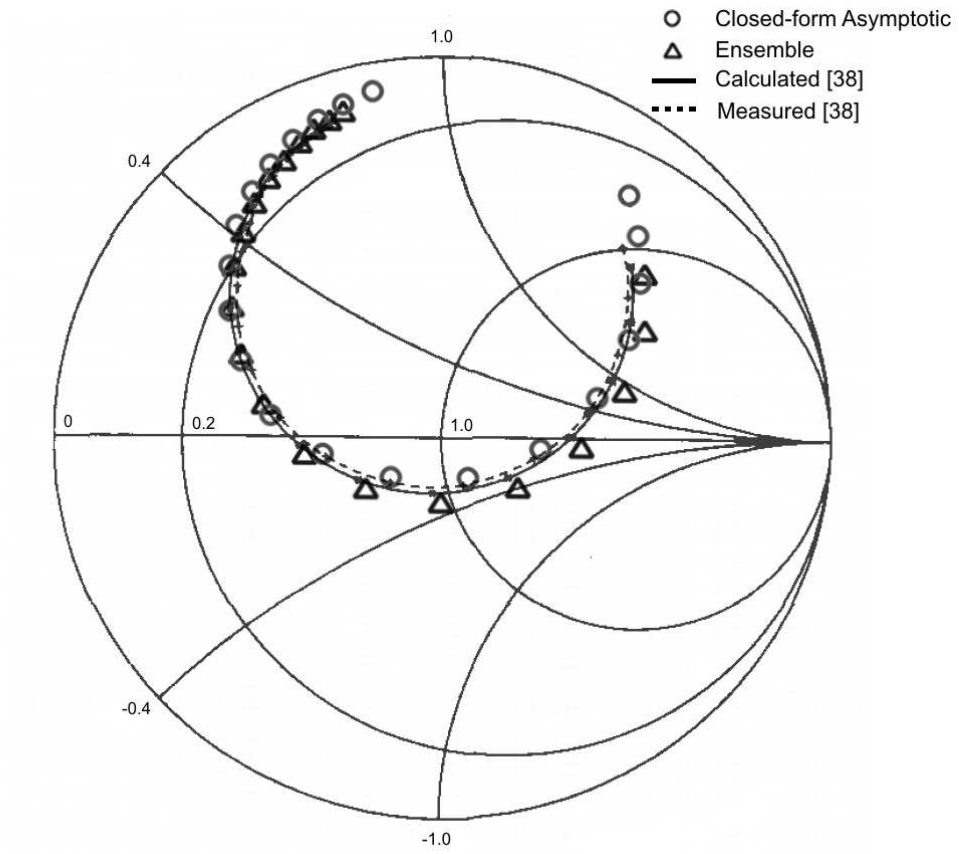

Figure 3.5: Input impedance data of a probe-fed, $L = 49.91$ mm by $W = 39.52$ mm rectangular antenna on a $h = 6.3$ mm thick grounded dielectric slab with $\epsilon_r = 2.484$. Frequency = 1.72-2.10 GHz.

3.4 Space Domain Green's Function for Planar Grounded Dielectric Slabs

Space domain representations of the Green's function is obtained by transforming the double IFT integrals into a Fourier-Bessel integral and employing some parameter transformations. This is also called the Sommerfeld integral type representation of the Green's function. The detailed derivation and computation of the Sommerfeld integral type representation of the Green's function is explained in a detailed way in [22]. In this section, we briefly review it and highlight the important steps. The evaluation of these integrals starts by considering the two dimensional (2-D) IFT of the spectral domain Green's function which is given by

$$G_{pq}(x,y) = \frac{1}{4\pi^2} \iint_{-\infty}^{\infty} \tilde{G}_{pq}(k_x,k_y)\, e^{j[k_x(x-x')+k_y(y-y')]}\, dk_x\, dk_y \tag{3.37}$$

($p = x$, y or z and $q = x$ or y). The integral in (3.37) can be written as a Fourier Bessel integral given by

$$G_{pq}(\rho,\rho',\phi,\phi') = \frac{1}{2\pi} \sum_{n=-\infty}^{\infty} e^{-jn(\phi-\phi')} \int_0^{\infty} \tilde{G}_{pq}(\xi,\alpha) J_n(\xi\rho) J_n(\xi\rho')\xi\, d\xi \tag{3.38}$$

where the following transformations have been used:

$$\begin{aligned} k_t &= \sqrt{k_x^2+k_y^2} = \xi && (3.39)\\ k_x &= \xi\cos(\alpha) && (3.40)\\ k_y &= \xi\sin(\alpha) && (3.41)\\ x-x' &= \rho\cos(\phi)-\rho'\cos(\phi') && (3.42)\\ y-y' &= \rho\sin(\phi)-\rho'\sin(\phi') \quad . && (3.43) \end{aligned}$$

If we choose the coordinate system in such a way that $\rho' = 0$, (3.38) becomes (using the fact that $J_0(0) = 1$, $J_m(0) = 0; m \neq 0$)

$$G_{pq}(\rho) = \frac{1}{2\pi} \int_0^{\infty} \tilde{G}_{pq}(\xi) J_0(s\xi)\xi\, d\xi \tag{3.44}$$

where

$$s = \rho - \rho' = \sqrt{(x-x')^2 + (y-y')^2}. \tag{3.45}$$

As a result the components of the Sommerfeld integral type representation of the Green's function can be written as

$$G_{xx}(s) = -\frac{Z_0}{2\pi k_0}\left[k_0^2 U + \frac{\partial^2}{\partial x^2}\left(U - \frac{\epsilon_r - 1}{\epsilon_r} W\right)\right] \tag{3.46}$$

$$G_{yy}(s) = -\frac{Z_0}{2\pi k_0}\left[k_0^2 U + \frac{\partial^2}{\partial y^2}\left(U - \frac{\epsilon_r - 1}{\epsilon_r} W\right)\right] \tag{3.47}$$

$$G_{xy}(s) = -\frac{Z_0}{2\pi k_0}\left[\frac{\partial^2}{\partial x \partial y}\left(U - \frac{\epsilon_r - 1}{\epsilon_r} W\right)\right] \tag{3.48}$$

$$G_{zx}(s) = \frac{Z_0}{2\pi k_0}\left[\frac{\partial P}{\partial x}\right] \tag{3.49}$$

$$G_{zy}(s) = \frac{Z_0}{2\pi k_0}\left[\frac{\partial P}{\partial y}\right]. \tag{3.50}$$

In (3.46)-(3.50), P, U and W are the Sommerfeld type integrals given by

$$P = \int_0^\infty \zeta_p(\xi) J_0(s\xi)\, d\xi \tag{3.51}$$

$$U = \int_0^\infty \zeta_u(\xi) J_0(s\xi)\, d\xi \tag{3.52}$$

$$W = \int_0^\infty \zeta_w(\xi) J_0(s\xi)\, d\xi \tag{3.53}$$

where the functions ζ_p, ζ_u and ζ_w are defined as

$$\zeta_p(\xi) = \frac{\beta_{z0}\,\xi}{\beta_{z1}[j\beta_{z1} + \epsilon_r \beta_{z0} \cot(t_h \beta_{z1})]} \tag{3.54}$$

$$\zeta_u(\xi) = \frac{\xi}{\beta_{z0} - j\beta_{z1}\cot(t_h\beta_{z1})} \tag{3.55}$$

$$\zeta_w(\xi) = \frac{\beta_{z0}\xi}{[\beta_{z0} - j\beta_{z1}\cot(t_h\beta_{z1})]\,[\beta_{z0} + \beta_{z1}\tan(t_h\beta_1)/\epsilon_r]} \tag{3.56}$$

with $J_0(s\xi)$ being the Bessel function of the first kind of order 0 with the argument $s\xi$. Finally β_{z0} and β_{z1} are defined as

$$\beta_{z0} = \begin{cases} \sqrt{k_0^2 - \xi^2} & \text{if } k_0^2 \geq \xi^2 \\ -j\sqrt{\xi^2 - k_0^2} & \text{if } k_0^2 < \xi^2 \end{cases} \tag{3.57}$$

$$\beta_{z1} = \sqrt{\epsilon_r k_0^2 - \xi^2}\,. \tag{3.58}$$

Note that during the evaluation of these Sommerfeld type integrals (i.e., P, U and W), the envelope extraction technique is used to speed up the computation of these integrals. Briefly,

(i) the limiting values of ζ_p, ζ_u and ζ_w are found when $\xi \to \infty$. These values are

$$\lim_{\xi\to\infty} \zeta_p(\xi) = \zeta_p^{\infty} = \frac{1}{\epsilon_r + 1} \tag{3.59}$$

$$\lim_{\xi\to\infty} \zeta_u(\xi) = \zeta_u^{\infty} = j(0.5) \tag{3.60}$$

$$\lim_{\xi\to\infty} \zeta_w(\xi) = \zeta_w^{\infty} = j\frac{(0.5)\epsilon_r}{\epsilon_r + 1}\,. \tag{3.61}$$

(ii) These limiting values are subtracted from the integrands and added as a separate integral as follows:

$$P = \int_0^{\infty} \left[\left(\zeta_p(\xi) - \zeta_p^{\infty}\right) J_0(s\xi)\right] d\xi + \int_0^{\infty} \zeta_p^{\infty} J_0(s\xi)\, d\xi \tag{3.62}$$

$$U = \int_0^\infty \left[(\zeta_u(\xi) - \zeta_u^\infty)\, J_0(s\xi)\right]\, d\xi + \int_0^\infty \zeta_u^\infty J_0(s\xi)\, d\xi \tag{3.63}$$

$$W = \int_0^\infty \left[(\zeta_w(\xi) - \zeta_w^\infty)\, J_0(s\xi)\right]\, d\xi + \int_0^\infty \zeta_w^\infty J_0(s\xi)\, d\xi \tag{3.64}$$

The first integrals in (3.62)-(3.64) are now rapidly decaying and hence are computed efficiently. On the other hand, the second integrals in (3.62)-(3.64) are evaluated analytically recognizing the fact that ζ_p^∞, ζ_u^∞ and ζ_w^∞ are constants and

$$\int_0^\infty \text{Constant} \cdot J_0(s\xi)\, d\xi = \frac{\text{Constant}}{s}\,. \tag{3.65}$$

Finally, in the numerical computation of the first integrals given in (3.62)-(3.64) special care is given to the pole singularities which exist in the interval $k_0 < \xi < \sqrt{\epsilon_r} k_0$. These singularities are treated using the singularity extraction method which is different than the singularity removal procedure for the self and overlapping terms explained in the following sections. For the details of this singularity extraction method reader is referred to [22].

3.5 Singularity Removal in the Spatial Domain for Overlapping Basis Functions

When calculating the mutual couplings for the MoM analysis, analytically evaluated asymptotic parts of the integrals, explained in the previous section, cause a singularity problem in the spatial domain integrals when the basis functions overlap (i.e. $s = 0$). This singularity must be removed for the efficient calculation of the MoM matrix entries in the space domain. This section describes the procedure for the singularity removal when we use PWS basis functions.

3.5.1 Z^{xx} Component Self-Term

Calculation of the coupling of the $\hat{x}$-directed PWS basis function with itself (self-term) in the spatial domain for planar dielectric slabs requires the computation

of the integral

$$Z_{nn}^{xx} = \int_{-y_a}^{y_a}\int_{-y_a}^{y_a}\int_{-x_a}^{x_a}\int_{-x_a}^{x_a} G_{xx} J_n(x,y) J_n(x',y')\, dx dx' dy dy' \tag{3.66}$$

where G_{xx} is the electric field of an $\hat{x}$-directed infinitesimal source given by (3.46) and J_n is the aforementioned PWS basis function given in (2.13). In the view of (3.63) and (3.64), the self-term can be separated into two parts. Namely the proper part (denoted by $Z_{nn}^{xx^{proper}}$) and the singular part (denoted by $Z_{nn}^{xx^{singular}}$). Hence Z_{nn}^{xx} is written as

$$\begin{aligned} Z_{nn}^{xx} &= Z_{nn}^{xx^{proper}} + Z_{nn}^{xx^{singular}} \\ &= \int_{-y_a}^{y_a}\int_{-y_a}^{y_a}\int_{-x_a}^{x_a}\int_{-x_a}^{x_a} \left(G_{xx}^{proper} + G_{xx}^{singular}\right) J_n(x,y) J_n(x',y')\, dx\, dx' dy\, dy'. \end{aligned} \tag{3.67}$$

Making use of (3.63) and (3.64), G_{xx}^{proper} and $G_{xx}^{singular}$ are defined as

$$G_{xx}^{proper} = -\frac{Z_0}{2\pi k_0}\left[k_0^2 U_{num} + \frac{\partial^2}{\partial x^2}\left(U_{num} - \frac{\epsilon_r - 1}{\epsilon_r} W_{num}\right)\right] \tag{3.68}$$

$$G_{xx}^{singular} = -\frac{Z_0}{2\pi k_0}\left[k_0^2 U_{analytic} + \frac{\partial^2}{\partial x^2}\left(U_{analytic} - \frac{\epsilon_r - 1}{\epsilon_r} W_{analytic}\right)\right] \tag{3.69}$$

Proper part of the integral (3.67) is carried out numerically whereas the singular part is treated carefully using some variable changes and approximate analytic formulas. By employing integration by parts in x and x' variables in order to transfer the derivatives onto the basis and testing functions as explained in [32] and using (3.63) and (3.64), we can write $Z_{nn}^{xx^{singular}}$ as

$$\begin{aligned} Z_{nn}^{xx^{singular}} = -\frac{Z_0}{2\pi k_0} \int_{-y_a}^{y_a}\int_{-y_a}^{y_a}\int_{-x_a}^{x_a}\int_{-x_a}^{x_a} \frac{1}{s}\Big\{ & \zeta_u^{\infty} k_0^2 \sin\left[k_e(x_a - |x|)\right] \sin\left[k_e(x_a - |x'|)\right] \\ & - \left(\zeta_u^{\infty} - \frac{\epsilon_r + 1}{\epsilon_r}\zeta_w^{\infty}\right) k_e^2 \cos\left[k_e(x_a - |x|)\right] \cos\left[k_e(x_a - |x'|)\right] \\ & \times \mathrm{sign}(x)\mathrm{sign}(x') \Big\} \frac{1}{4y_a^2 \sin^2(k_e x_a)}\, dx\, dx'\, dy\, dy' \end{aligned} \tag{3.70}$$

where s is given in (3.45). Note that since the singular point $s = 0$ is in the integration surface, standard numerical techniques can not be used for this integral. First step to attack this integral is to reduce the order of integration. This is achieved by using the following the change of variables:

$$\tau = \frac{1}{\sqrt{2}}(y' - y) \tag{3.71}$$

$$\psi = \frac{1}{\sqrt{2}}(y' + y) \tag{3.72}$$

$$dy'\,dy = d\tau\,d\psi \tag{3.73}$$

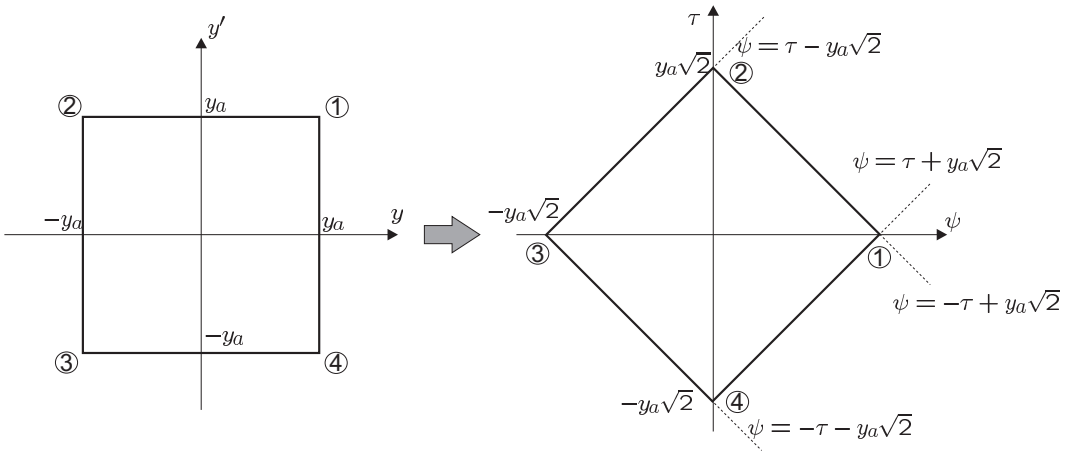

Figure 3.6: Mapping from the y-y' plane to τ-ψ plane

By doing that the y-y' integrals are converted to τ and ψ domain integrals as it is shown in Fig. 3.6. However, the resultant integrands are only a function of τ. That is, τ and ψ domain integrations can be carried out analytically by employing the following integration formulas:

$$\int_{\tau_1}^{\tau_2} \frac{\tau}{\sqrt{a^2+\tau^2}}\,d\tau = \sqrt{a^2+\tau_2^2} - \sqrt{a^2+\tau_2^1} \tag{3.74}$$

$$\int_{\tau_1}^{\tau_2} \frac{1}{\sqrt{a^2+\tau^2}}\,d\tau = \ln\left(a+\sqrt{\tau_2^2+a^2}\right) - \ln\left(a+\sqrt{\tau_1^2+a^2}\right). \tag{3.75}$$

As a result (3.70), which was initially a four-fold integral, is reduced into a double integral given by

$$\begin{aligned} Z_{nn}^{xx^{singular}} &= \int_{-x_a}^{x_a}\int_{-x_a}^{x_a} \Big\{ c_1(x,x')\cos\left[k_e(2x_a-|x'|-|x|)\right] + c_2(x,x')\cos\left[k_e(|x'|-|x|)\right] \Big\} \\ &\quad \left\{ 4y_a \left[\ln\left(y_a\sqrt{2} + \sqrt{\left(\frac{x'-x}{\sqrt{2}}\right)^2 + 2y_a^2} \right) - \ln\left|\frac{x'-x}{\sqrt{2}}\right| \right] \right. \\ &\quad \left. -2\sqrt{2}\left[\sqrt{\left(\frac{x'-x}{\sqrt{2}}\right)^2 + 2y_a^2} - \left|\frac{x'-x}{\sqrt{2}}\right| \right] \right\} dx\,dx' \end{aligned} \tag{3.76}$$

where the functions $c_1(x,x')$ and $c_2(x,x')$ are defined as

$$\begin{aligned} c_1(x,x') &= -\frac{Z_0}{16\pi k_0 y_a^2 \sin^2(k_e x_a)} \\ &\quad \times \left\{ k_e^2 \mathrm{sign}(x)\mathrm{sign}(x') \left(\zeta_u^\infty - \frac{\epsilon_r - 1}{\epsilon_r}\zeta_w^\infty \right) + k_0^2 \zeta_u^\infty \right\} \\ c_2(x,x') &= -\frac{Z_0}{16\pi k_0 y_a^2 \sin^2(k_e x_a)} \\ &\quad \times \left\{ k_e^2 \mathrm{sign}(x)\mathrm{sign}(x') \left(\zeta_u^\infty - \frac{\epsilon_r - 1}{\epsilon_r}\zeta_w^\infty \right) - k_0^2 \zeta_u^\infty \right\} . \end{aligned} \tag{3.77}$$

There are two possible values of each $c_1(x,x')$ and $c_2(x,x')$ based on the value of $\mathrm{sign}(x)\mathrm{sign}(x')$ which will be called $c_{1\pm}$ and $c_{2\pm}$. We use c_{1+} and c_{2+} when the $\mathrm{sign}(x)\mathrm{sign}(x')$ product is positive, and we use c_{1-} and c_{2-} otherwise.

A similar change of variables is used on the x, x' variables as follows:

$$\nu = \frac{x'-x}{\sqrt{2}} \tag{3.78}$$

$$\upsilon = \frac{x'+x}{\sqrt{2}} \tag{3.79}$$

$$dx\,dx' = d\nu\,d\upsilon \tag{3.80}$$

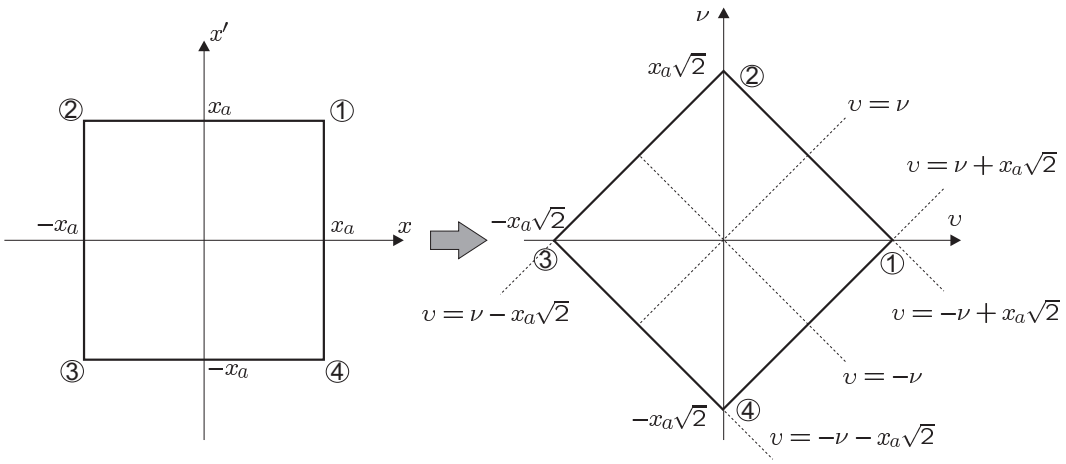

Figure 3.7: Mapping from the x-x' plane to ν-υ plane

which is depicted in Fig. 3.7. Integration on the variable υ can be done analytically. Finally for the resultant ν domain integral we perform a final change of variable given by

$$\alpha = \frac{\nu}{x_a\sqrt{2}} \tag{3.81}$$

$$d\alpha = \frac{d\nu}{x_a\sqrt{2}} \tag{3.82}$$

in order to normalize the integration interval to $(0,1)$. After arranging and regrouping the resultant terms the final integral is in the form of

$$\begin{aligned} Z_{nn}^{xx^{singular}} = & \int_0^{0.5} d\alpha \Big\{ c_3 \sin\left[k_e x_a(1-2\alpha)\right] + c_4\alpha\cos\left[k_e 2x_a(1-\alpha)\right] \\ & + c_5(1-2\alpha)\cos(2k_e x_a\alpha) + c_6\sin(2k_e x_a\alpha)\Big\}\mathcal{H}(\alpha)\,d\alpha \\ & + \int_{0.5}^{1} \Big\{ c_4(1-\alpha)\cos[2k_e x_a(1-\alpha)] \\ & + c_6\sin[2k_e x_a(1-\alpha)]\Big\}\mathcal{H}(\alpha)\,d\alpha \end{aligned} \tag{3.83}$$

where $\mathcal{H}(\alpha)$ is defined as

$$\begin{aligned}\mathcal{H}(\alpha) &= y_a\sqrt{2}\left[\ln\left(y_a+\sqrt{x_a^2\alpha^2+y_a^2}\right)-\ln(x_a\alpha)\right] \\ &\quad -\sqrt{2}\left[\sqrt{x_a^2+\alpha^2}-x_a\alpha\right]\end{aligned} \tag{3.84}$$

and the constants c_3 to c_6 are given by

$$c_3 = \frac{x_a 16\sqrt{2}}{k_e}\cos(k_e x_a)c_{1+} \tag{3.85}$$

$$c_4 = x_a^2 16\sqrt{2}c_{1-} \tag{3.86}$$

$$c_5 = x_a^2 16\sqrt{2}c_{2+} \tag{3.87}$$

$$c_6 = \frac{x_a 8\sqrt{2}}{k_e}c_{2-}\,. \tag{3.88}$$

Numerical integration of the 1-D integral given in (3.83) is significantly more efficient compared to the original four-fold integral given in (3.70). However, still a careful evaluation is required for this integral when α is close to 0 because of the term $\ln(x_a\alpha)$. The best solution to this problem is to use the asymptotic values of the sine and cosine functions in the interval $(0,\delta_1)$ and integrate this part of the integral analytically. This δ_1 parameter is chosen to be $2k_e x_a\delta_1 \ll 1$. Using the series expansion of sine and cosine functions and ignoring the higher order terms one can write:

$$\lim_{\alpha\to 0}\cos(2k_e x_a\alpha) \approx 1 \tag{3.89}$$

$$\lim_{\alpha\to 0}\sin(2k_e x_a\alpha) \approx 2k_e x_a\alpha \tag{3.90}$$

$$\lim_{\alpha\to 0}\sin[k_e x_a(1-2\alpha)] \approx 2\sin(k_e x_a) - k_e x_a\cos(k_e x_a\alpha) \tag{3.91}$$

$$\lim_{\alpha\to 0}\cos[2k_e x_a(1-\alpha)] \approx 2\cos(2k_e x_a) + 2k_e x_a\sin(2k_e x_a\alpha)\,. \tag{3.92}$$

As a result, the problematic part of (3.83) (denoted by I_{p1}) can be written as

$$\begin{aligned} I_{p1} &= -y_a\sqrt{2}\int_0^{\delta_1}(d_1+d_2\alpha+d_3\alpha^2)\ln(\alpha)d\alpha \\ &\quad -y_a\sqrt{2}\int_{\delta_1}^{0.5}d\alpha\Big\{c_3\sin\left[k_e x_a(1-2\alpha)\right]+c_4\alpha\cos\left[k_e 2x_a(1-\alpha)\right] \\ &\quad +c_5(1-2\alpha)\cos(2k_e x_a\alpha)+c_6\sin(2k_e x_a\alpha)\Big\}\ln(\alpha)\,d\alpha \end{aligned} \tag{3.93}$$

where the $\ln(x_a)$ part is left out. Now the first integral in (3.93) (denoted by $I_{p1}^{singular}$) can be evaluated in closed-form as

$$\begin{aligned} I_{p1}^{singular} &= -y_a\sqrt{2}\int_0^{\delta_1}(d_1+d_2\alpha+d_3\alpha^2)\ln(\alpha)d\alpha \\ &= -y_a\sqrt{2}\left\{d_1(\delta_1\ln(\delta_1)-\delta_1)+d_2\left(\frac{\delta_1^2}{2}\ln(\delta_1)-\frac{\delta_1^2}{4}\right)\right. \\ &\quad \left.+d_3\left(\frac{\delta_1^3}{3}\ln(\delta_1)-\frac{\delta_1^3}{9}\right)\right\} \end{aligned} \tag{3.94}$$

where the constants d_1, d_2 and d_3 are given by

$$d_1 = c_3\sin(k_e x_a)+c_5 \tag{3.95}$$

$$d_2 = -2c_3k_e x_a\cos(k_e x_a)+c_4\cos(2k_e x_a)-2c_5+2c_6k_e x_a \tag{3.96}$$

$$d_3 = 2c_4k_e x_a\sin(2k_e x_a)\,. \tag{3.97}$$

Finally (3.83) is expressed in its numerically efficient form as

$$\begin{aligned} Z_{nn}^{xx^{singular}} &= \int_0^{0.5}d\alpha\Big\{c_3\sin\left[k_e x_a(1-2\alpha)\right]+c_4\alpha\cos\left[k_e 2x_a(1-\alpha)\right] \\ &\quad +c_5(1-2\alpha)\cos(2k_e x_a\alpha)+c_6\sin(2k_e x_a\alpha)\Big\}\mathcal{H}^r(\alpha)\,d\alpha \end{aligned}$$

$$+\int_{0.5}^{1}\Big\{c_4(1-\alpha)\cos[2k_e x_a(1-\alpha)] \\ +c_6\sin[2k_e x_a(1-\alpha)]\Big\}\mathcal{H}(\alpha)\,d\alpha + I_{p1} \tag{3.98}$$

where

$$\begin{aligned}\mathcal{H}^r(\alpha) &= y_a\sqrt{2}\left[\ln\left(y_a+\sqrt{x_a^2\alpha^2+y_a^2}\right)-\ln(x_a)\right] \\ &\quad -\sqrt{2}\left[\sqrt{x_a^2+\alpha^2}-x_a\alpha\right]\,.\end{aligned} \tag{3.99}$$

Equation (3.98) can be evaluated using a simple Gaussian quadrature scheme except the $I_{p1}^{singular}$ part which is found in closed-form. The evaluation of the proper part of the self-term $Z_{nn}^{xx^{proper}}$ is explained in Section 3.6.1 .

Note that self-term (Z_{mm}^{yy}) for the $\hat{y}$-directed basis functions can be evaluated using the same expressions (3.98) and (3.84) by simply interchanging the half-length (x_a) and half-width (y_a) of the $\hat{x}$-directed basis function with those of the $\hat{y}$-directed one.

In order to asses the accuracy of this method, we compare the singularity removed self-term results with the spectral domain method results for different sets of geometric parameters given in Table 3.6.

	ϵ_r	t_h	x_a	y_a
Case 1	3.25	$0.06\lambda_0$	$0.195\lambda_0$	$0.005\lambda_0$
Case 2	2.59	$0.02\lambda_0$	$0.05\lambda_0$	$0.05\lambda_0$
Case 3	2.59	$0.003\lambda_0$	$0.05\lambda_0$	$0.01\lambda_0$

Table 3.6: Geometric Parameters

The spectral domain solution to the mutual coupling calculation is pretty accurate for the self-term. Hence, we use it as a reference solution to check the accuracy of the space domain solution. Table 3.7 shows that the results are in good agreement

	Spectral Domain (Z_{nn}^{xx})	Spatial Domain (Z_{nn}^{xx})
Case 1	$-16.14 - j141.87$	$-16.14 - j141.7$
Case 2	$-0.046 + j82.1$	$-0.046 + j82.11$
Case 3	$-0.001 + j98.6$	$-0.001 + j98.9$

Table 3.7: Spectral and Spatial Domain Self-Term Results

with the spectral domain solution. Spatial domain solution to the self-term is generally faster than the spectral domain counter part except for electrically very thin substrates. For electrically thin substrates, convergence of the numerical evaluation of integrals in the proper part of the self-term occupies most of the computation time. CPU time[1] is 11.3sec. for the spectral solution of Case 1 where as the spatial domain solution takes only 1.58sec. However, for Case 3 the spectral domain solution (2.5sec.) is faster compared to the spatial domain CPU time which is found to be 17.0sec.

3.5.2 $Z_{n\,(n+1)}^{xx}$ (or $Z_{n\,(n+1)}^{yy}$) Component Overlapping-Term

In the previous subsection singularity treatment for the self-term is explained. In the analysis of microstrip antennas and antenna arrays using the spatial domain MoM, another case where singularity occurs is the overlapping (not entirely) basis functions (both $\hat{x}$-directed or $\hat{y}$-directed) case where $s = x_a$. In this situation, the mutual coupling between two overlapping basis functions can be written as

$$Z_{n(n+1)}^{xx} = \int_{-y_a}^{y_a}\int_{-y_a}^{y_a}\int_{0}^{2x_a}\int_{-x_a}^{x_a} G_{xx}\frac{\sin\left[k_e(x_a - |x|)\right]}{2y_a\sin(k_e x_a)} \times \frac{\sin\left[k_e(x_a - |x' - x_a|)\right]}{2y_a\sin(k_e x_a)}\,dx\,dx'\,dy\,dy'\,. \tag{3.100}$$

[1]Intel 2.6GHz Pentium 4 CPU with HT and 1GB RAM

Similar to the self-term singularity removal procedure explained in the previous subsection in the view of (3.66), (3.68) and (3.69) we can write the singular part of the mutual coupling (3.100) as

$$Z_{n(n+1)}^{xx^{singular}} = \int_{-y_a}^{y_a}\int_{-y_a}^{y_a}\int_{0}^{2x_a}\int_{-x_a}^{x_a}\frac{1}{s}\Big\{t_3(x,x')\cos\left[k_e(2x_a-|x|-|x'-x_a|)\right] + t_4(x,x')\cos\left[k_e(|x'-x_a|-|x|)\right]\Big\}\,dx\,dx'\,dy\,dy' \quad (3.101)$$

where $t_3(x,x')$ and $t_4(x,x')$ are defined as

$$t_3(x,x') = -\frac{t_1\text{sign}(x'-x_a)\,\text{sign}(x)+t_2}{2} \quad (3.102)$$

$$t_4(x,x') = \frac{t_2-t_1\text{sign}(x'-x_a)\,\text{sign}(x)}{2} \quad (3.103)$$

$$(3.104)$$

with the constants t_1 and t_2 given by

$$t_1 = -\frac{Z_0}{2\pi k_0}\Big\{\zeta_u^{\infty}-\frac{\epsilon-1}{\epsilon}\zeta_w^{\infty}\Big\}\frac{k_e^2}{4y_a^2\sin^2(k_e x_a)} \quad (3.105)$$

$$t_2 = -\left(\frac{Z_0}{2\pi k_0}\right)\frac{k_0^2\zeta_u^{\infty}}{4y_a^2\sin^2(k_e x_a)}\,. \quad (3.106)$$

There are two possible values of each $t_3(x,x')$ and $t_4(x,x')$ based on the value of $\text{sign}(x'-x_a)\,\text{sign}(x)$ which will be called $t_{3\pm}(x,x')$ and $t_{3\pm}(x,x')$. When the $\text{sign}(x'-x_a)\,\text{sign}(x)$ product is positive we use t_{3+} and t_{4+}, and we use t_{3-} and t_{4-} otherwise

Equation (3.101) can be reduced to a 2-D integral by carrying out the y and y' integrals analytically, in a similar fashion how (3.76) is derived. Briefly, using the same change of variables and integration formulas given by (3.71)-(3.75), (3.101) can be expressed as

$$Z_{n(n+1)}^{xx^{singular}} = \int_0^{2x_a}\int_{-x_a}^{x_a} \Big\{ t_3 \cos\left[k_e(2x_a - |x'-x_a| - |x|)\right] + t_4 \cos\left[k_e(|x'-x_a| - |x|)\right] \Big\}$$
$$\left\{ 4y_a \left[\ln\left(y_a\sqrt{2} + \sqrt{\left(\frac{x'-x}{\sqrt{2}}\right)^2 + 2y_a^2} \right) - \ln\left|\frac{x'-x}{\sqrt{2}}\right| \right] \right.$$
$$\left. -2\sqrt{2}\left[\sqrt{\left(\frac{x'-x}{\sqrt{2}}\right)^2 + 2y_a^2} - \left|\frac{x'-x}{\sqrt{2}}\right| \right] \right\} dx\, dx' \,. \qquad (3.107)$$

Transformation from the integration domain of x-x' integrals to the ν-υ domain integrals, based on the change of variables denoted in (3.78)-(3.80), are shown in Fig. 3.8. Applying this last change of variables (3.81)-(3.82) to this integral to normalize the integration limits, the resultant one-dimensional integral is obtained as

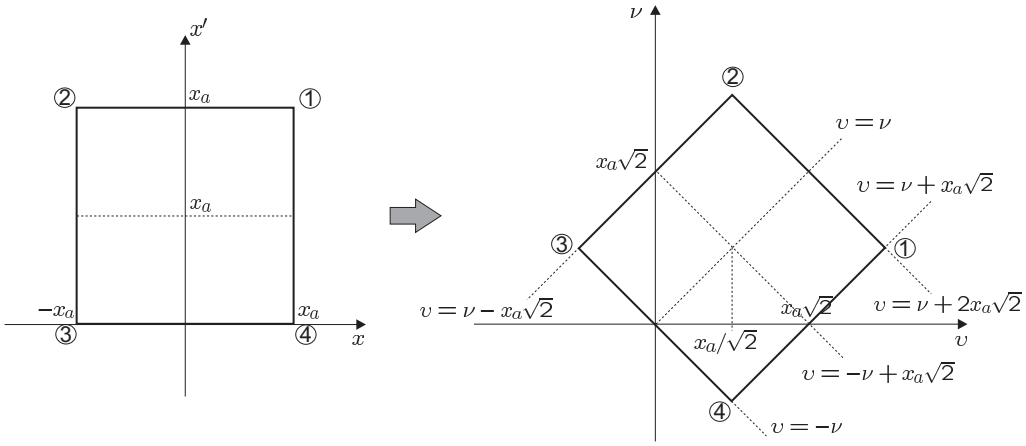

Figure 3.8: Mapping from the x-x' plane to ν-υ plane

$$Z_{n(n+1)}^{xx^{singular}} = \int_0^{0.5} \Big\{ t_5 \sin(2k_e x_a \alpha) + t_6(1-2\alpha)\cos(2k_e x_a \alpha)$$
$$+ t_7 \alpha \cos[k_e x_a(1-2\alpha)] + t_8 \sin[k_e x_a(1-2\alpha)] \Big\} \mathcal{H}(\alpha)\, d\alpha$$

$$+\int_{0.5}^{1}\Big\{t_5\sin[2k_ex_a(1-\alpha)]-t_9(1-2\alpha)\cos[k_ex_a(3-2\alpha)]$$

$$+t_7(1-\alpha)\cos[k_ex_a(1-2\alpha)]-t_{10}\sin[k_ex_a(1-2\alpha)]\Big\}\mathcal{H}(\alpha)\,d\alpha$$

$$+\int_{1}^{1.5}\Big\{t_9(3-2\alpha)\cos[k_ex_a(3-2\alpha)]$$

$$+t_{10}\sin[k_ex_a(3-2\alpha)]\Big\}\mathcal{H}(\alpha)\,d\alpha \tag{3.108}$$

where

$$t_5 = 8\sqrt{2}x_a\frac{\cos(k_ex_a)}{k_e}t_{3+} \tag{3.109}$$

$$t_6 = 8\sqrt{2}x_a^2\cos(k_ex_a)t_{3-} \tag{3.110}$$

$$t_7 = 16\sqrt{2}x_a^2t_{4+} \tag{3.111}$$

$$t_8 = 8\sqrt{2}x_a\frac{1}{k_e}t_{4-} \tag{3.112}$$

$$t_9 = 4\sqrt{2}x_a^2t_{3-} \tag{3.113}$$

$$t_{10} = 4\sqrt{2}x_a\frac{1}{k_e}t_{4-} \tag{3.114}$$

and $\mathcal{H}(\alpha)$ is given by (3.84). Similar to the evaluation of (3.83), (3.108) is problematic when α approaches to zero due to the $\ln(\alpha)$ term. Denoting this part of (3.108) as I_{p2}, in a similar fashion to (3.93) I_{p2} is written in the following way:

$$I_{p2} = -y_a\sqrt{2}\int_{0}^{\delta_2}(\kappa_1+\kappa_2\alpha+\kappa_3\alpha^2)\ln(\alpha)\,d\alpha$$

$$-y_a\sqrt{2}\int_{\delta}^{0.5}\Big\{t_5\sin(2k_ex_a\alpha)+t_6(1-2\alpha)\cos(2k_ex_a\alpha)$$

$$+t_7\alpha\cos[k_ex_a(1-2\alpha)]+t_8\sin[k_ex_a(1-2\alpha)]\Big\}\ln(\alpha)\,d\alpha \tag{3.115}$$

where κ_1, κ_2 and κ_3 are defined by employing the asymptotic values of sine and

cosine functions (3.89)-(3.92) as

$$\kappa_1 = t_6 + t_8 \sin(k_e x_a) \tag{3.116}$$

$$\kappa_2 = 2t_5 k_e x_a - 2t_6 + t_7 \cos(k_e x_a) - 2t_8 k_e x_a(\cos(k_e x_a)) \tag{3.117}$$

$$\kappa_3 = 2t_7 k_e x_a \sin(k_e x_a)\,. \tag{3.118}$$

Also δ_2 is chosen in such a way that $2k_e x_a \delta_2 \ll 1$. The first integral in (3.115), which is called $I_{p2}^{singular}$, is evaluated in closed-form given by

$$\begin{aligned} I_{p2}^{singular} &= -y_a\sqrt{2}\int_0^{\kappa_2}(d_1 + d_2\alpha + d_3\alpha^2)\ln(\alpha)d\alpha \\ &= -y_a\sqrt{2}\left\{d_1(\kappa_2\ln(\kappa_2) - \kappa_2) + d_2\left(\frac{\kappa_2^2}{2}\ln(\kappa_2) - \frac{\kappa_2^2}{4}\right)\right. \\ &\qquad \left. + d_3\left(\frac{\kappa_2^3}{3}\ln(\kappa_2) - \frac{\kappa_2^3}{9}\right)\right\} \end{aligned} \tag{3.119}$$

Finally (3.108) is rewritten in its numerically efficient form as follows:

$$\begin{aligned} Z_{n(n+1)}^{xx^{singular}} &= \int_0^{0.5}\Big\{t_5\sin(2k_e x_a\alpha) + t_6(1-2\alpha)\cos(2k_e x_a\alpha) \\ &\qquad + t_7\alpha\cos[k_e x_a(1-2\alpha)] + t_8\sin[k_e x_a(1-2\alpha)]\Big\}\mathcal{H}^r(\alpha)\,d\alpha \\ &\quad + \int_{0.5}^{1}\Big\{t_5\sin[2k_e x_a(1-\alpha)] - t_9(1-2\alpha)\cos[k_e x_a(3-2\alpha)] \\ &\qquad + t_7(1-\alpha)\cos[k_e x_a(1-2\alpha)] - t_{10}\sin[k_e x_a(1-2\alpha)]\Big\}\mathcal{H}(\alpha)\,d\alpha \\ &\quad + \int_{1}^{1.5}\Big\{t_9(3-2\alpha)\cos[k_e x_a(3-2\alpha)] \\ &\qquad + t_{10}\sin[k_e x_a(3-2\alpha)]\Big\}\mathcal{H}(\alpha)\,d\alpha + I_{p2}\,. \end{aligned} \tag{3.120}$$

This integral is evaluated using a simple Gaussian quadrature integration scheme just like the self-term evaluations. As it is mentioned before proper part of the overlapping-term $Z_{n(n+1)}^{xx}$ is evaluated in an efficient way explained in 3.6.1. Note

	Spectral Domain ($Z^{xx}_{n(n+1)}$)	Spatial Domain ($Z^{xx}_{n(n+1)}$)
Case 1	$-11.8 - j186.1$	$-11.8 - j185.9$
Case 2	$-0.045 - j40.6$	$-0.045 - j40.6$
Case 3	$-0.001 - j54.4$	$-0.001 - j54.64$

Table 3.8: Spectral and Spatial Domain Overlapping-Term Results

that overlapping term ($Z^{yy}_{m(m+1)}$) for $\hat{y}$-directed basis functions can be evaluated using the same equations (3.115), (3.119) and (3.120) with the $\hat{x}$-directed ones, by interchanging the the half-length (x_a) and half-width (y_a) of the $\hat{x}$-directed basis functions with those of the $\hat{y}$-directed ones.

A comparison of the numerical results found using the spatial domain and spectral domain methods for the geometric parameters tabulated in Table 3.6, is given in Table 3.8. The results show an excellent agreement between the spectral and space domain solutions.

3.5.3 Z^{xy}_{mn} Component Overlapping-Term

Finally, we investigated the cross-coupling terms. Consider two basis functions: one $\hat{x}$-directed with its center point $(0, 0)$ and the other one $\hat{y}$-directed with its center at $(-x_a/2, -y_a)$. $2x_a$ and $2y_a$ are the length and width of the $\hat{x}$-directed basis function where as the length of the $\hat{y}$-directed one is $4y_a$ and its width is x_a. The mutual coupling between these two basis functions can be written as

$$
\begin{aligned}
Z^{xy}_{mn} &= Z^{xy^{proper}}_{mn} + Z^{xy^{singular}}_{mn} \\
&= \int_{-3y_a}^{y_a} \int_{-y_a}^{y_a} \int_{-x_a}^{0} \int_{-x_a}^{x_a} (G^{proper}_{xy}(s) + G^{singular}_{xy}(s)) \frac{\sin\left[k_e(2y_a - |y' + y_a|)\right]}{x_a \sin(2k_e y_a)} \\
&\qquad \times \frac{\sin\left[k_e(x_a - |x|)\right]}{2y_a \sin(k_e y_a)}\, dx\, dx'\, dy\, dy'
\end{aligned} \tag{3.121}
$$

where the Green's function component G_{xy} is given in (3.48) and it can be written in terms of its singular and proper terms as

$$\begin{aligned} G_{xy} &= G_{xy}^{proper} + G_{xy}^{singular} \\ G_{xy}^{proper} &= -\frac{Z_0}{2\pi k_0}\left[\frac{\partial^2}{\partial x \partial y}\left(U_{num} - \frac{\epsilon_r - 1}{\epsilon_r} W_{num}\right)\right] \qquad (3.122) \\ G_{xy}^{singular} &= -\frac{Z_0}{2\pi k_0}\left[\frac{\partial^2}{\partial x \partial y}\left(U_{analytic} - \frac{\epsilon_r - 1}{\epsilon_r} W_{analytic}\right)\right]. \qquad (3.123) \end{aligned}$$

Using $G_{xy}^{singular}$ and transferring the derivatives onto the basis and testing functions via integration by parts, singular part of (3.121) can be written as

$$\begin{aligned} Z_{mn}^{xy^{singular}} = \int_{-3y_a}^{y_a}\int_{-y_a}^{y_a}\int_{-x_a}^{0}\int_{-x_a}^{x_a} \frac{c_1^{xy}}{s}\left\{\cos\left[k_e(x_a - |x|)\right]\cos\left[k_e(2y_a - |y' + y_a|)\right]\right\} \\ \times \mathrm{sign}(x)\mathrm{sign}(y' + y_a)\, dx\, dx'\, dy\, dy' \qquad (3.124) \end{aligned}$$

where the constant c_1^{xy} is given by

$$c_1^{xy} = \frac{Z_0}{2\pi k_0}\left\{\zeta_u^{\infty} - \frac{\epsilon_r - 1}{\epsilon_r}\zeta_w^{\infty}\right\}\left\{\frac{k_e^2}{2x_a y_a \sin(k_e x_a)\sin(2k_e y_a)}\right\}. \qquad (3.125)$$

Similar to the previous cases (Z_{nn}^{xx} and $Z_{n(n+1)}^{xx}$), first y, y' domain integrations denoted by I_Y and given by

$$I_Y = \int_{-3y_a}^{y_a}\int_{-y_a}^{y_a} \frac{1}{s}\cos[k_e(2y_a - |y' + y_a|)]\mathrm{sign}(y' + y_a)\, dy\, dy' \qquad (3.126)$$

is reduced to a 1-D integral, using the transformations given in (3.71)-(3.73). Transformation of integration domain from y-y' to τ-ψ domain is depicted in Fig. 3.9. The resultant integral is given by

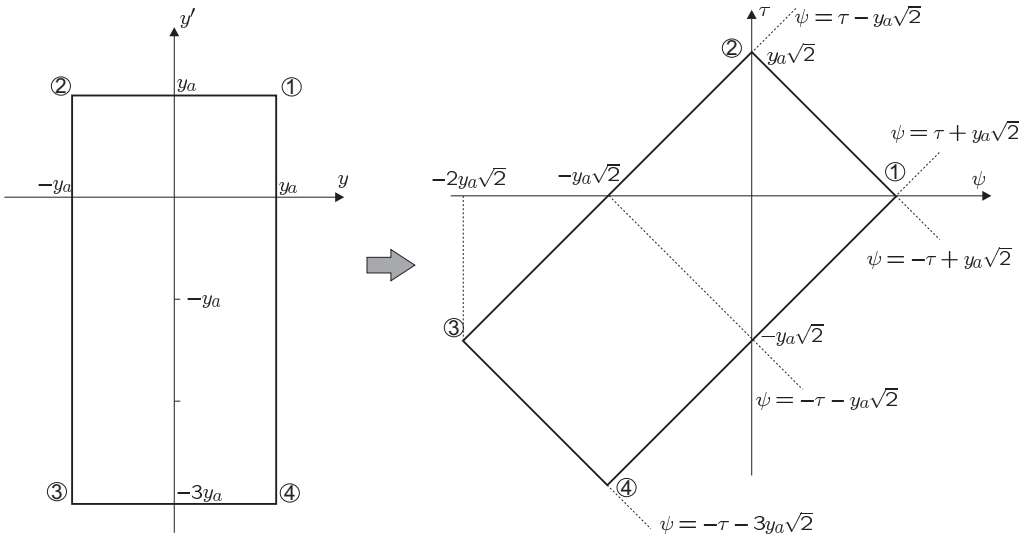

Figure 3.9: Mapping from the y-y' plane to τ-ψ plane

$$I_Y^{1D} = -\frac{1}{k_e}\Bigg\{ \int_0^{y_a\sqrt{2}} \frac{\sin(k_e\tau\sqrt{2}) - 2\sin[k_e(2y_a - \tau\sqrt{2})]}{\sqrt{\left(\frac{x'-x}{\sqrt{2}}\right)^2 + \tau^2}}\, d\tau \int_{y_a\sqrt{2}}^{2y_a\sqrt{2}} \frac{\sin[k_e(4y_a - \tau\sqrt{2})]}{\sqrt{\left(\frac{x'-x}{\sqrt{2}}\right)^2 + \tau^2}}\, d\tau \Bigg\}. \tag{3.127}$$

Then by applying the following change of variables given by

$$\beta = \frac{\tau}{y_a\sqrt{2}} \tag{3.128}$$

$$d\beta = \frac{d\tau}{y_a\sqrt{2}} \tag{3.129}$$

to normalize the integration limits, (3.127) becomes

$$I_Y^{1D} = -\frac{y_a\sqrt{2}}{k_e}\Bigg\{ \int_0^{1} \frac{\sin(2k_e y_a\beta) - 2\sin[2k_e y_a(1-\beta)]}{\sqrt{\left(\frac{x'-x}{\sqrt{2}}\right)^2 + 2y_a^2\beta^2}}\, d\beta \int_{1}^{2} \frac{\sin[2k_e y_a(2-\beta)]}{\sqrt{\left(\frac{x'-x}{\sqrt{2}}\right)^2 + 2y_a^2\beta^2}}\, d\beta \Bigg\}. \tag{3.130}$$

Next, we work on the x-x' domain integrals denoted by I_X. By changing the order of integration, x-x' domain integrals are written as

$$I_X = \int_{-x_a}^{0} \int_{-x_a}^{x_a} \cos[k_e(x_a - |x|)]\text{sign}(x) \frac{1}{\sqrt{\left(\frac{x'-x}{\sqrt{2}}\right)^2 + 2y_a^2\beta^2}}\, dx\, dx' \,. \tag{3.131}$$

Then using the change of variables given in (3.78)-(3.80), which is depicted in Fig. 3.10, x-x' domain integral is transformed into a ν-υ domain integral where υ integration is evaluated analytically. As a result, in a similar fashion with the previous sections, (3.131) is reduced to a 1-D integral denoted by I_X^{1D}. Finally by changing the variables using (3.81) and (3.82), integration limits are normalized and I_X^{1D} is given by

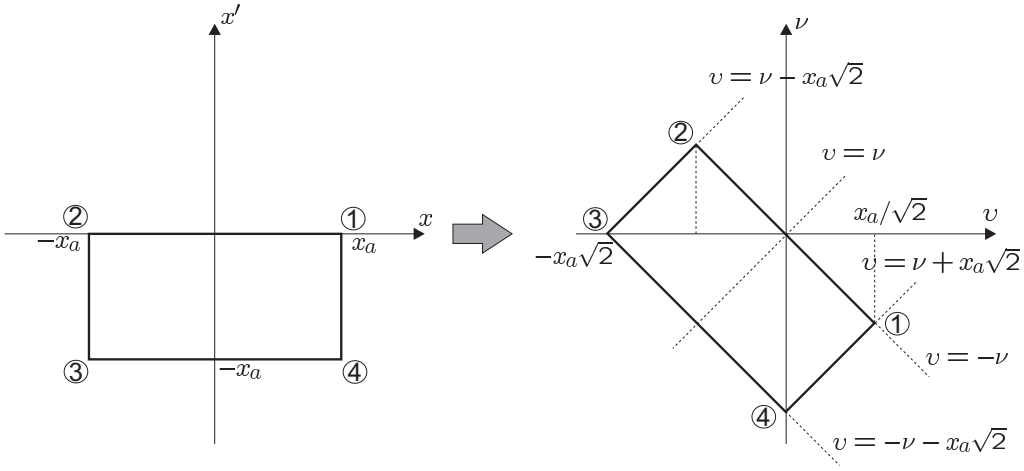

Figure 3.10: Mapping from the x-x' plane to ν-υ plane

$$\begin{aligned} I_X^{1D} &= \int_0^{0.5} \frac{2x_a}{k_e}\Big\{\sin(2k_e x_a\alpha) - 2\sin[k_e x_a(1-2\alpha)]\Big\} \frac{1}{\sqrt{2x_a^2\alpha^2 + 2y_a^2\beta^2}}\, d\alpha \\ &\quad + \int_{0.5}^{1} \frac{2x_a}{k_e} \sin[2k_e x_a(1-2\alpha)] \frac{1}{\sqrt{2x_a^2\alpha^2 + 2y_a^2\beta^2}}\, d\alpha \,. \end{aligned} \tag{3.132}$$

Once again, implementation of I_X^{1D} requires special attention since the denominator has a zero at $\alpha = 0$ if $\beta = 0$. So we approximate sine and cosine functions

in the interval $(0, \delta_\alpha)$ and using the integral formulas given in (3.74) and (3.75) we evaluate the singular part I_{Xs}^{1D} in closed-form given by

$$\begin{aligned} I_{Xs}^{1D} &= \frac{x_a\sqrt{2}}{k_e}\int_0^{\delta_\alpha}\Big\{\sin(2k_e x_a\alpha) - 2\sin[k_e(1-2\alpha)]\Big\}\frac{d\alpha}{\sqrt{x_a^2\alpha^2+y_a^2\beta^2}} \\ &\approx 2\sqrt{2}\left\{1+2\cos(k_e x_a)\right\}\left\{\sqrt{x_a^2\delta_\alpha^2+y_a^2\beta^2}-y_a\beta\right\} \\ &\quad -\frac{2\sqrt{2}}{k_e}\sin(k_e x_a)\left\{\ln\left(x_a\delta_\alpha+\sqrt{\beta^2y_a^2+x_a^2\delta_\alpha^2}\right)-\ln(\beta y_a)\right\}. \quad (3.133) \end{aligned}$$

As a result we rewrite I_X^{1D} as

$$\begin{aligned} I_X^{1D} &= \frac{x_a\sqrt{2}}{k_e}\int_{\delta_\alpha}^{0.5}\Big\{\sin(2k_e x_a\alpha) - 2\sin[k_e(1-2\alpha)]\Big\}\frac{d\alpha}{\sqrt{x_a^2\alpha^2+y_a^2\beta^2}} \\ &\quad + I_{Xs}^{1D} + \frac{x_a\sqrt{2}}{k_e}\int_{0.5}^{1}\sin[2k_e x_a(1-\alpha)]\frac{d\alpha}{\sqrt{x_a^2\alpha^2+y_a^2\beta^2}} \quad (3.134) \end{aligned}$$

where δ_α is chosen to be $2k_e x_a\delta_\alpha \ll 1$. For $\beta = 0$ this equation has still a logarithmic singularity and as β gets closer to 0, the erratic behavior of the integrand affects the numerical accuracy of the integral. Final equation including the treatment of this singularity can be derived from (3.124) by combining (3.130) and (3.134) and Z_{mn}^{xy} becomes

$$\begin{aligned} Z_{mn}^{xy} &= -c_1^{xy}\frac{y_a}{k_e}\Bigg[\sqrt{2}\int_0^1\Big\{\sin(2k_e y_a\beta) - 2\sin[2k_e y_a(1-\beta)]\Big\} \\ &\quad \times\left\{I_X^{1D}(\beta) - \frac{2\sqrt{2}}{k_e}\sin(k_e x_a)\ln(\beta)\right\}d\beta \\ &\quad +\frac{4}{k_e}\sin(k_e x_a)\int_{\delta_\beta}^1\Big\{\sin(2k_e y_a\beta) - 2\sin[2k_e y_a(1-\beta)]\Big\}\ln(\beta)d\beta \\ &\quad +8\sin(k_e x_a)\Bigg\{y_a[1+2\cos(2k_e y_a)]\left(\frac{\delta_\beta^2}{2}\ln(\delta_\beta)-\frac{\delta_\beta^2}{4}\right) \\ &\quad -\frac{1}{k_e}[\delta_\beta\ln(\delta_\beta)-\delta_\beta]\Bigg\} + \sqrt{2}\int_1^2\sin[2k_e y_a(2-\beta)]I_X^{1D}(\beta)\,d\beta\Bigg]. \quad (3.135) \end{aligned}$$

Similar to δ_α, δ_β is chosen to be $2k_e y_a \delta_\beta \ll 1$. Proper part of the cross coupling $Z_{mn}^{xy^{proper}}$ is evaluated numerically in an efficient way, which is explained in Section 3.6.2, in order to increase the accuracy of the solution even for the electrically very thin substrates.

In Table 3.9 comparison of the space and spectral domain solutions are given to test the accuracy of the space domain formulation for the cross coupling (denoted by Z_{mn}^{xy}) of basis (which are oriented in $\hat{x}$ or $\hat{y}$-direction) and testing functions (which are oriented in $\hat{y}$ or $\hat{x}$-direction), whose domains overlap. Geometric parameters given in Table 3.6 are used. Similar to the previous results which are given for the other components, agreement is very good between the two solutions.

	Spectral Domain (Z_{mn}^{xy})	Spatial Domain (Z_{mn}^{xy})
Case 1	$0.001 - j30.88$	$0.001 - j30.95$
Case 2	$0.0003 - j43.31$	$0.0003 - j43.32$
Case 3	$2.0 \times 10^{-7} - j49.6$	$2.0 \times 10^{-7} - j50.1$

Table 3.9: Spectral and Spatial Domain (Z_{mn}^{xy}) Results

3.5.4 Probe V_m^x Component Singularity Treatment

Probe component singularity treatment is rather simple compared to other components due to the simplicity of the Green's function components G_{zx} and G_{zy}. Using (3.50) and (3.62) and employing integration by parts in order to transfer the derivative onto the basis function, singular part of the voltage vector entry is given by

$$V_m^{x^{singular}} = -\frac{Z_0}{2\pi k_0} \int_{y_m-y_a}^{y_m+y_a} \int_{x_m-x_a}^{x_m+x_a} \frac{\zeta_p^\infty}{s} \text{sign}(x-x_m) \times \frac{\cos[k_e(x_a - |x-x_m|)]}{2y_a \sin(k_e x_a)}\, dx\, dy\,. \tag{3.136}$$

This time s is defined as $\sqrt{(x-x_p)^2+(y-y_p)^2}$, where (x_p, y_p) represent the position of the probe which is feeding the antenna. Note that $x_m + x_a < x_p < x_m + x_a$ and $y_m - y_a < y_p < y_m + y_a$. Thus, s can take the value 0 in this integral and there is a possible singularity in the numerical integration. Fortunately we can carry out the y-integration in closed-form using the integration formula (3.75). Then the resulting expression for (3.136) becomes

$$V_m^{x^{singular}} = -\frac{Z_0}{4\pi y_a \sin(k_e x_a) k_0} \int_{x_m-x_a}^{x_m+x_a} \left\{ \ln\left(y_2 + \sqrt{(x-x_p)^2+y_2^2}\right) - \ln\left(y_1 + \sqrt{(x-x_p)^2+y_1^2}\right) \right\} \times \cos[k_e(a-|x-x_m|)]\text{sign}(x-x_m)\, dx \tag{3.137}$$

where

$$y_1 = y_A - y_a \tag{3.138}$$

$$y_2 = y_A + y_a \tag{3.139}$$

where $y_A = y_p - y_m$. Table 3.10 shows the comparison between spectral and spatial domain results for the voltage vector entry of an $\hat{x}$-directed basis function $(x_m,\, y_m) = (0,\, 0)$ with a probe located at $(x_p,\, y_p) = (-x_a/2,\, 0)$. Geometric parameters are the same as given in Table 3.6. Once again space domain results are in good agreement with the spectral domain results.

	Spectral Domain (V_m^x)	Spatial Domain (V_m^x)
Case 1	$1.29 + j106.99$	$1.29 + j106.74$
Case 2	$0.005 + j61.04$	$0.005 + j61.01$
Case 3	$9.6 \times 10^{-5} + j63.86$	$9.1 \times 10^{-5} + j63.71$

Table 3.10: Spectral and Spatial Domain V_x Results

3.6 Mutual Coupling Calculation in Spatial Domain for Planar Grounded Dielectric Slabs (A general case where there is no singularity)

Spatial domain mutual coupling calculations require the numerical computation of the two double integrals on the domains of the basis and testing functions. Although a simple Gaussian quadrature numerical integration scheme is enough in the computation, the convergence of these integrals can become quite troublesome for relatively large basis functions and when the dielectric substrate is electrically very thin. However, using some change of variables in the spatial coordinates, the order of each of these integrals can be reduced to one by analytically evaluating one of the integrals. This reduces the computational effort and accelerates the spatial domain calculations.

3.6.1 Integration Domain Mapping in Spatial Domain: $\hat{x}$-$\hat{x}$ Case

Mutual coupling between two $\hat{x}$-directed PWS basis functions, located at (x_m, y_m) and (x_n, y_n) with the same dimensions, can be written as

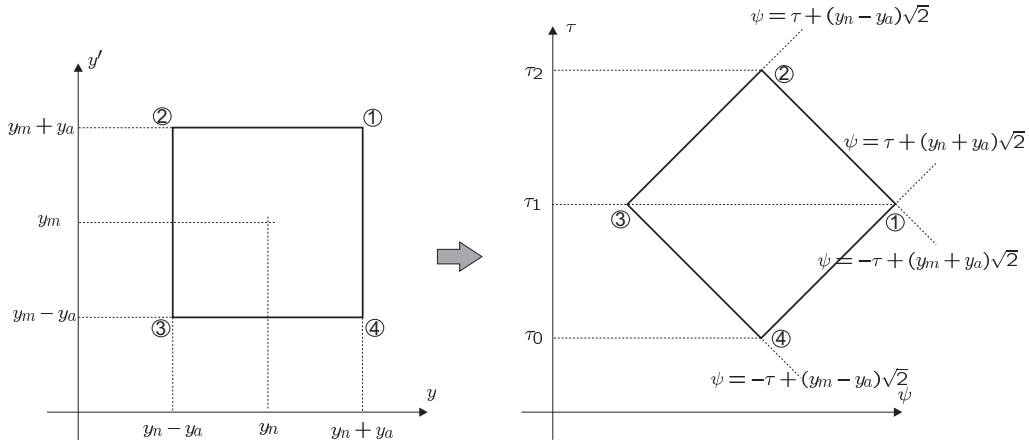

Figure 3.11: Mapping from the y-y' plane to τ-ψ plane

$$Z_{mn}^{xx} = \int_{y_m-y_a}^{y_m+y_a}\int_{y_n-y_a}^{y_n+y_a}\int_{x_m-x_a}^{x_m+x_a}\int_{x_n-x_a}^{x_n+x_a} G_{xx}(s)\frac{\sin[k_e(x_a-|x-x_n|)]}{2y_a\sin(k_e x_a)} \times\frac{\sin[k_e(x_a-|x'-x_m|)]}{2y_a\sin(k_e x_a)}\,dx\,dx'\,dy\,dy' \tag{3.140}$$

where x_a and y_a are the half-length and half-width of the basis functions and s is given in (3.45). In order to reduce the order of y-y' integrals, we start by mapping the y-y' domain to the τ-ψ domain by the change of variables given in (3.71)-(3.73), which is depicted in Fig. 3.11. Using the new variables s can be written as

$$s = \sqrt{(x-x')^2 + 2\tau^2}. \tag{3.141}$$

ψ integral is evaluated analytically by noting that ψ does not occur in the integrand. The resultant three-fold integral is given by

$$Z_{mn}^{xx} = \int_{\tau_0}^{\tau_2}\mathcal{T}_{xx}(\tau)\left\{\int_{x_m-x_a}^{x_m+x_a}\int_{x_n-x_a}^{x_n+x_a} G_{xx}(s)\frac{\sin[k_e(x_a-|x-x_n|)]}{2y_a\sin(k_e x_a)} \times\frac{\sin[k_e(x_a-|x'-x_m|)]}{2y_a\sin(k_e x_a)}\,dx\,dx'\right\}d\tau \tag{3.142}$$

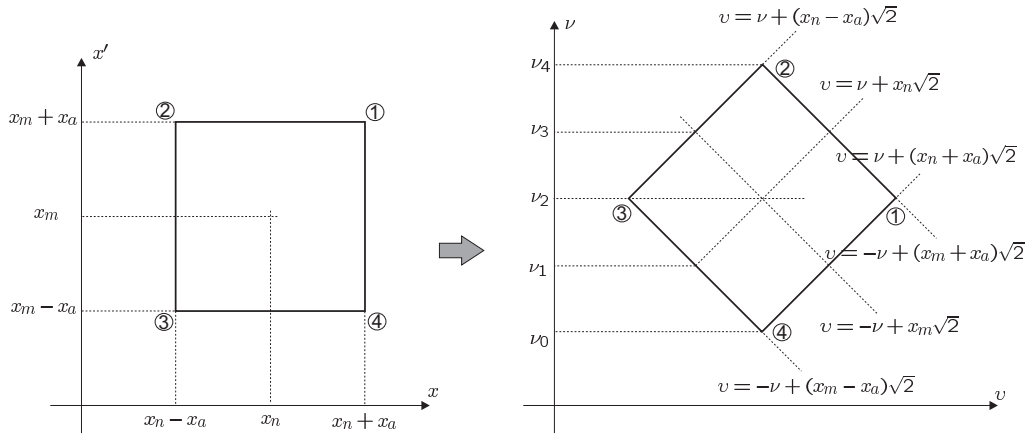

Figure 3.12: Mapping from the x-x' plane to ν-υ plane

where $\mathcal{T}_{xx}(\tau)$ is defined as

$$\mathcal{T}_{xx}(\tau) = \begin{cases} -2\tau + (2y_a + y_s)\sqrt{2} & \tau_1 \leq \tau < \tau_2 \\ 2\tau + (2y_a - y_s)\sqrt{2} & \tau_0 \leq \tau < \tau_1 \end{cases} \tag{3.143}$$

with the integration limits τ_0, τ_1 and τ_2 are given as

$$\tau_0 = \frac{y_s - 2y_a}{\sqrt{2}} \tag{3.144}$$

$$\tau_1 = \frac{y_s}{\sqrt{2}} \tag{3.145}$$

$$\tau_2 = \frac{y_s + 2y_a}{\sqrt{2}} \tag{3.146}$$

and $y_s = y_m - y_n$.

As the next step, after transferring the spatial derivatives in (3.46) onto the basis and testing functions x-x' domain is mapped to ν-υ domain (shown in Fig. 3.12) in a similar fashion as the previous section. Making use of some trigonometric identities and after regrouping the terms, final form of Z_{mn}^{xx} is given by

$$Z_{mn}^{xx} = -\frac{Z_0}{2\pi k_0} \left(\frac{1}{2y_a \sin(k_e x_a)} \right)^2 \int_{\tau_0}^{\tau_2} \mathcal{T}_{xx}(\tau) \left\{ I_{v1} + I_{v2} + I_{v3} \right\} d\tau \tag{3.147}$$

where I_{v1}, I_{v2} and I_{v3} are the integrals defined as

$$\begin{aligned} I_{v1} &= 2\int_{\nu_1}^{\nu_3} \Big\{ \cos[k_e(x_s - \nu\sqrt{2})]\mathcal{V}_1^{xx}(\nu)\left\{k_0^2 U(s) - k_e^2 Q(s)\right\} \\ &\qquad + \mathcal{V}_2^{xx}(\nu)\left\{k_0^2 U(s) + k_e^2 Q(s)\right\}\Big\} d\nu \end{aligned} \tag{3.148}$$

$$\begin{aligned} I_{v2} &= \int_{\nu_2}^{\nu_4} \Big\{ \cos[k_e(2x_a + x_s - \nu\sqrt{2})]\mathcal{V}_3^{xx}(\nu)\left\{k_0^2 U(s) - k_e^2 Q(s)\right\} \\ &\qquad + \mathcal{V}_4^{xx}(\nu)\left\{k_0^2 U(s) + k_e^2 Q(s)\right\}\Big\} d\nu \end{aligned} \tag{3.149}$$

$$\begin{aligned} I_{v3} &= \int_{\nu_0}^{\nu_2} \Big\{ \cos[k_e(2x_a - x_s + \nu\sqrt{2})]\mathcal{V}_5^{xx}(\nu)\left\{k_0^2 U(s) - k_e^2 Q(s)\right\} \\ &\qquad + \mathcal{V}_6^{xx}(\nu)\left\{k_0^2 U(s) + k_e^2 Q(s)\right\}\Big\} d\nu \end{aligned} \tag{3.150}$$

with

$$\mathcal{V}_1^{xx}(\nu) = \begin{cases} \nu - \frac{x_s - x_a}{\sqrt{2}} & \nu_1 < \nu < \nu_2 \\ \\ -\nu + \frac{x_s + x_a}{\sqrt{2}} & \nu_2 < \nu < \nu_3 \end{cases} \tag{3.151}$$

$$\mathcal{V}_2^{xx}(\nu) = \begin{cases} \frac{\cos(k_e x_a)}{k_e\sqrt{2}} \sin[k_e(-\nu\sqrt{2} - x_a + x_s)] & \nu_1 < \nu < \nu_2 \\ \\ \frac{\cos(k_e x_a)}{k_e\sqrt{2}} \sin[k_e(-\nu\sqrt{2} - x_a - x_s)] & \nu_2 < \nu < \nu_3 \end{cases} \tag{3.152}$$

$$\mathcal{V}_3^{xx}(\nu) = \begin{cases} \frac{x_s - \nu\sqrt{2}}{\sqrt{2}} & \nu_2 < \nu < \nu_3 \\ \\ \frac{-2x_a - x_s + \nu\sqrt{2}}{\sqrt{2}} & \nu_3 < \nu < \nu_4 \end{cases} \tag{3.153}$$

$$\mathcal{V}_4^{xx}(\nu) = \begin{cases} -\frac{\sin[k_e(x_s - \nu\sqrt{2})]}{k_e\sqrt{2}} & \nu_2 < \nu < \nu_3 \\ \\ \frac{\sin[k_e(2x_a + x_s - \nu\sqrt{2})]}{k_e\sqrt{2}} & \nu_3 < \nu < \nu_4 \end{cases} \tag{3.154}$$

$$\mathcal{V}_5^{xx}(\nu) = \begin{cases} \frac{-2x_a+x_s-\nu\sqrt{2}}{\sqrt{2}} & \nu_0 < \nu < \nu_1 \\ \\ \frac{-x_s+\nu\sqrt{2}}{\sqrt{2}} & \nu_1 < \nu < \nu_2 \end{cases} \tag{3.155}$$

$$\mathcal{V}_6^{xx}(\nu) = \begin{cases} \frac{\sin[k_e(2x_a-x_s+\nu\sqrt{2})]}{k_e\sqrt{2}} & \nu_0 < \nu < \nu_1 \\ \\ \frac{\sin[k_e(x_s-\nu\sqrt{2})]}{k_e\sqrt{2}} & \nu_1 < \nu < \nu_2 \end{cases} . \tag{3.156}$$

In (3.148)-(3.150), the $Q(s)$ function is defined as

$$Q(s) = U(s) - \frac{\epsilon_r - 1}{\epsilon_r} W(s)\,, \text{ with} \tag{3.157}$$

$U(s)$ and $W(s)$ are given before by (3.52) and (3.53), respectively. Finally, the separation s becomes $s = \sqrt{2\nu^2 + 2\tau^2}$ and the integration limits $\nu_0\,, \nu_1\,, \nu_2\,, \nu_3$ and ν_4 are given as

$$\nu_0 = \frac{x_s - 2x_a}{\sqrt{2}} \tag{3.158}$$

$$\nu_1 = \frac{x_s - x_a}{\sqrt{2}} \tag{3.159}$$

$$\nu_2 = \frac{x_s}{\sqrt{2}} \tag{3.160}$$

$$\nu_3 = \frac{x_s + x_a}{\sqrt{2}} \tag{3.161}$$

$$\nu_4 = \frac{x_s + 2x_a}{\sqrt{2}} \tag{3.162}$$

with $x_s = x_m - x_n$. The resultant τ and ν integrals are evaluated with a careful numerical computation which uses an adaptive Gaussian quadrature integration scheme in order to increase the efficiency of the solution. In this numerical integration scheme the number of points are doubled adaptively until a convergence criteria is met between the consecutive iterations. This convergence criteria is chosen for a desired accuracy.

3.6.2 Integration Domain Mapping in Spatial Domain: $\hat{x}$-$\hat{y}$ Case

Mutual coupling between an $\hat{x}$ and a $\hat{y}$-directed PWS basis functions located at (x_n, y_n) and (x_m, y_m), respectively is given by

$$Z_{mn}^{xy} = \int_{y_m-2y_a}^{y_m+2y_a}\int_{y_n-y_a}^{y_n+y_a}\int_{x_m-x_a/2}^{x_m+x_a/2}\int_{x_n-x_a}^{x_n+x_a} G_{xy}(s)\frac{\sin[k_e(x_a-|x-x_n|)]}{2y_a\sin(k_e x_a)} \times\frac{\sin[k_e(2y_a-|y'-y_m|)]}{x_a\sin(2k_e y_a)}\,dx\,dx'\,dy\,dy' \tag{3.163}$$

where G_{xy} is given by (3.48). After transferring the derivatives onto the basis and testing functions, and by using the same change of variables given by (3.78)-(3.80) (shown in Fig. 3.13), (3.163) becomes

$$Z_{mn}^{xy} = \frac{Z_0}{2\pi k_0}\left[\frac{k_e}{\sqrt{2}x_a\sin(2k_e y_a)}\right]\int_{y_m-2y_a}^{y_m+2y_a}\int_{y_n-y_a}^{y_n+y_a}\cos[k_e(2y_a-|y'-y_m|)] \times\text{sign}(y'-y_m)\left\{\int_{\nu_0^{xy}}^{\nu_3^{xy}}\mathcal{V}^{xy}(\nu)Q(s)\,d\nu\right\}dy\,dy' \tag{3.164}$$

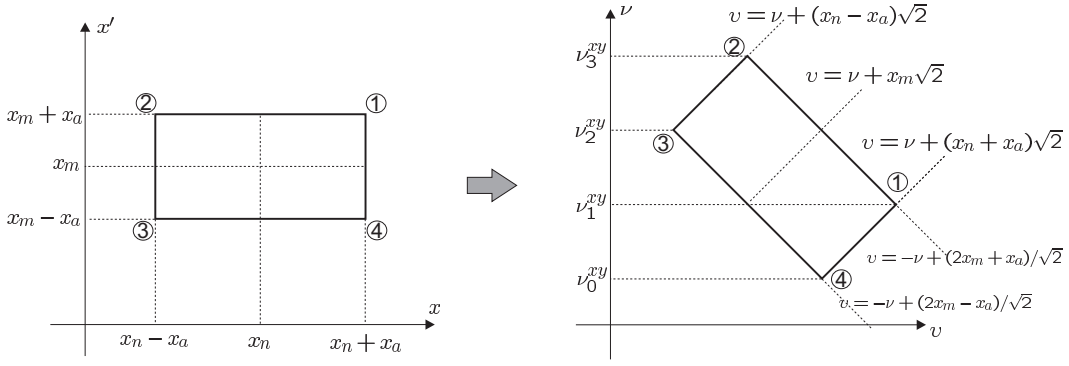

Figure 3.13: Mapping from the x-x' plane to ν-υ plane

where

$$\mathcal{V}^{xy}(\nu) = \begin{cases} -\sin[k_e(1.5x_a - x_s + \nu\sqrt{2})] & \nu_0^{xy} < \nu < \nu_1^{xy} \\ 2\cos\left(\frac{k_e x_a}{2}\right)\sin[k_e(\nu\sqrt{2} - x_s)] & \nu_1^{xy} < \nu < \nu_2^{xy} \\ \sin[k_e(1.5x_a + x_s - \nu\sqrt{2})] & \nu_2^{xy} < \nu < \nu_3^{xy} \end{cases} \tag{3.165}$$

and the constants ν_0^{xy}, ν_1^{xy}, ν_2^{xy} and ν_3^{xy} are given by

$$\nu_0^{xy} = \frac{x_s - 1.5x_a}{\sqrt{2}} \tag{3.166}$$

$$\nu_1^{xy} = \frac{x_s - 0.5x_a}{\sqrt{2}} \tag{3.167}$$

$$\nu_2^{xy} = \frac{x_s + 0.5x_a}{\sqrt{2}} \tag{3.168}$$

$$\nu_3^{xy} = \frac{x_s + 1.5x_a}{\sqrt{2}}\,. \tag{3.169}$$

Finally y-y' domain integration is converted into a τ-ψ domain integration using the change of variables given by (3.71)-(3.72)(shown in Fig. 3.14). The final form of the equation is in the form of

$$Z_{mn}^{xy} = \frac{Z_0}{2\pi k_0}\left(\frac{1}{x_a y_a \sin(k_e x_a)\sin(2k_e y_a)}\right)\int_{\tau_0^{xy}}^{\tau_3^{xy}} \mathcal{T}_{xy}(\tau)\left\{\int_{\nu_0^{xy}}^{\nu_3^{xy}} \mathcal{V}^{xy}(\nu)Q(s)\,d\nu\right\}d\tau \tag{3.170}$$

where the function $\mathcal{T}(\tau)$ is given by

$$\mathcal{T}_{xy}(\tau) = \begin{cases} \sin[k_e(3y_a - y_s + \tau\sqrt{2})] & \tau_0^{xy} < \tau < \tau_1^{xy} \\ 2\cos(k_e y_a)\sin[k_e(y_s - \tau\sqrt{2})] & \tau_1^{xy} < \tau < \tau_2^{xy} \\ -\sin[k_e(3y_a + y_s - \tau\sqrt{2})] & \tau_2^{xy} < \tau < \tau_3^{xy} \end{cases}\,. \tag{3.171}$$

The constants τ_0^{xy}, τ_1^{xy}, τ_2^{xy} and τ_3^{xy} are defined as

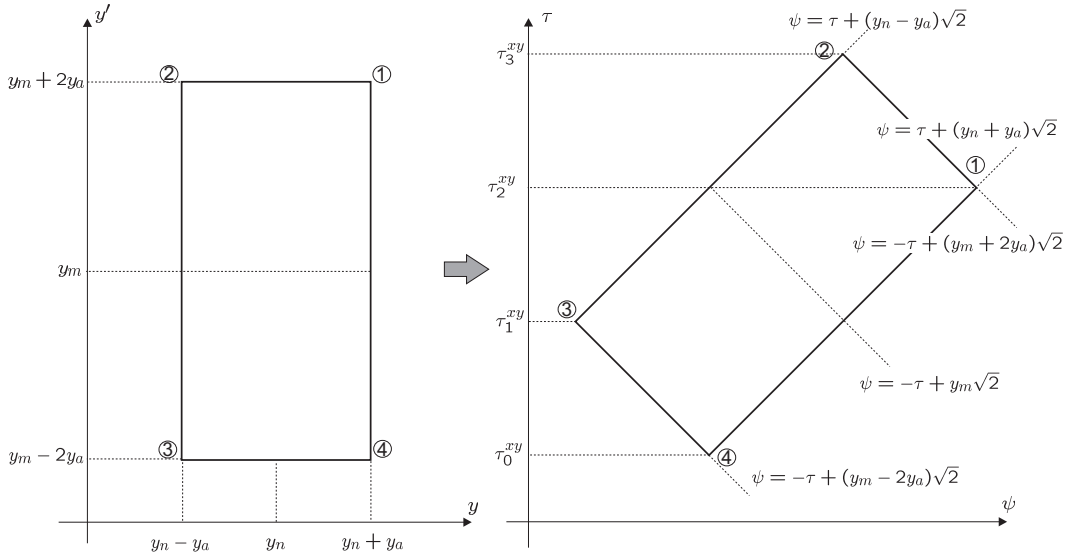

Figure 3.14: Mapping from the y-y' plane to τ-ψ plane

$$\tau_0^{xy} = \frac{y_s - 3y_a}{\sqrt{2}} \tag{3.172}$$

$$\tau_1^{xy} = \frac{y_s - y_a}{\sqrt{2}} \tag{3.173}$$

$$\tau_2^{xy} = \frac{y_s + y_a}{\sqrt{2}} \tag{3.174}$$

$$\tau_3^{xy} = \frac{y_s + 3y_a}{\sqrt{2}}\,. \tag{3.175}$$

The τ-ν integrals in (3.170) are evaluated numerically using an adaptive Gaussian quadrature integration scheme in a similar fashion to the $\hat{x}$-$\hat{x}$ case.

3.6.3 Evaluation of $V_m^{x,y}$ in Spatial Domain

The component of the voltage vector for an $\hat{x}$-directed basis function located at (x_m, y_m) can be expressed as

$$V_m^x = \int_{y_m - y_a}^{y_m + y_a} \int_{x_m - x_a}^{x_m + x_a} G_{zx}(s) \frac{\sin[k_e(x_a - |x - x_m|)]}{2y_a \sin(k_e x_a)}\, dy\, dx \tag{3.176}$$

where $s = \sqrt{(x_p - x)^2 + (y_p - y)^2}$ and (x_p, y_p) is the position of the the probe. There is no mapping applied to the integration domain of this integral, since it is already in the form of a double integral. An efficient adaptive Gaussian quadrature method is used in the numerical evaluation of this integral.

Note that voltage vector entry for an $\hat{y}$-directed basis function can be found by changing the parameters $x \leftrightarrow y$, center coordinates, half-length (x_a) and half-width (y_a) of the $\hat{x}$-directed basis functions with those of the and $\hat{y}$-directed basis functions.

Chapter 4

Green's Function Representations for Cylindrical Grounded Dielectric Slab

4.1 Spectral Domain Representation of Green's Function for Cylindrical Grounded Dielectric Slabs

Surface field components on a dielectric coated PEC cylinder can be expressed as a cylindrical IFT of their spectral domain counterparts given by

$$E_\phi(\phi, z) = \frac{1}{2\pi} \sum_{n=-\infty}^{\infty} e^{jn\phi} \left\{ \int_{-\infty}^{\infty} \tilde{E}_\phi(n, k_z) e^{jk_z z}\, dk_z \right\} \tag{4.1}$$

$$E_z(\phi, z) = \frac{1}{2\pi} \sum_{n=-\infty}^{\infty} e^{jn\phi} \left\{ \int_{-\infty}^{\infty} \tilde{E}_z(n, k_z) e^{jk_z z}\, dk_z \right\}. \tag{4.2}$$

In (4.1) and (4.2) the spectral domain electric field components are obtained using the special Green's function and the Fourier transform of the surface currents,

given by

$$\begin{bmatrix} \tilde{E}_\phi \\ \tilde{E}_z \end{bmatrix} = \begin{bmatrix} \tilde{G}_{\phi\phi} & \tilde{G}_{\phi z} \\ \tilde{G}_{z\phi} & \tilde{G}_{zz} \end{bmatrix} \begin{bmatrix} \tilde{J}_\phi \\ \tilde{J}_z \end{bmatrix}. \tag{4.3}$$

Derivation of these Green's function components starts with writing the electric field in terms of cylindrical wave functions

$$\tilde{E}_z^i = \sum_{n=-\infty}^{\infty} e^{-jn\phi}[a_n^i J_n(k_{ti}\rho) + b_n^i H_n^{(2)}(k_{ti}\rho)] \tag{4.4}$$

$$\tilde{H}_z^i = \sum_{n=-\infty}^{\infty} e^{-jn\phi}[c_n^i J_n(k_{ti}\rho) + d_n^i H_n^{(2)}(k_{ti}\rho)] \tag{4.5}$$

where the superscript $i = 1$ indicates the dielectric region whereas $i = 0$ indicates the free space. The constants a_n^i, b_n^i, c_n^i and d_n^i are found by applying the following boundary conditions:

(i) Tangential electric field is zero on conducting surfaces (at $\rho = a$ and on the printed conductor at $\rho = d$),

(ii) Tangential components of the electric field is continuous at the dielectric-air interface ($\rho = d$),

(iii) Tangential components of the magnetic field are continuous at the dielectric-air interface ($\rho = d$) except the printed conductor surfaces, where $\hat{n} \times \overline{H} = \overline{J}$

(iv) Radiation condition: fields vanish $\rho \to \infty$.

Finally in (4.4) and (4.5) k_{ti} denotes the transverse propagation constant in free-space ($i = 0$) and in the dielectric region ($i = 1$), which is defined as

$$k_{t0}^2 = k_0^2 - k_z^2; \quad k_0 = \omega\sqrt{\epsilon_0\mu_0} \tag{4.6}$$

$$k_{t1}^2 = k_1^2 - k_z^2; \quad k_1 = \omega\sqrt{\epsilon_1\mu_1}\,. \tag{4.7}$$

When the source and observation points are both on the air-dielectric interface ($\rho = \rho' = d$), the special Green's function components are given by [33]

$$\tilde{G}_{\phi\phi}(n, k_z) = \frac{jZ_0}{k_0}\left\{\left[\frac{k_0^2 k_{t0}}{k_{t1}^2}\right]\frac{R_n C_n^e T_m}{T} - k_{t0}\frac{R_n T_c^2}{(\epsilon_r - 1)T} - \left[\frac{nk_z}{dk_{t1}}\right]^2 \frac{C_n^e - k_{t0}R_n}{T}\right\} \tag{4.8}$$

$$\tilde{G}_{\phi z}(n,k_z)=\tilde{G}_{z\phi}(n,k_z)=\frac{jZ_0}{k_0}\left[\frac{nk_z}{d}\frac{k_{t0}^2}{k_{t1}^2}\frac{(C_n^e-k_{t0}R_n)}{T}\right] \tag{4.9}$$

$$\tilde{G}_{zz}(n,k_z)=\frac{jZ_0}{k_0}k_{t0}^2\frac{T_e}{T} \tag{4.10}$$

where

$$T=T_eT_m-T_c^2 \tag{4.11}$$

$$T_e=k_{t0}R_n-\frac{k_{t0}^2}{k_{t1}^2}C_n^e \tag{4.12}$$

$$T_m=k_{t0}R_n-\epsilon_r\frac{k_{t0}^2}{k_{t1}^2}C_n^m \tag{4.13}$$

$$T_c=\frac{k_0(\epsilon_r-1)}{k_{t1}^2}\frac{nk_z}{d} \tag{4.14}$$

$$R_n=\frac{H_n^{(2)'}(k_{t0}d)}{H_n^{(2)}(k_{t0}d)} \tag{4.15}$$

$$C_n^e=k_{t1}\frac{J_n'(k_{t1}a)Y_n'(k_{t1}d)-J_n'(k_{t1}d)Y_n'(k_{t1}a)}{J_n'(k_{t1}a)Y_n(k_{t1}d)-J_n(k_{t1}d)Y_n'(k_{t1}a)} \tag{4.16}$$

$$C_n^m=k_{t1}\frac{J_n(k_{t1}a)Y_n'(k_{t1}d)-J_n'(k_{t1}d)Y_n(k_{t1}a)}{J_n(k_{t1}a)Y_n(k_{t1}d)-J_n(k_{t1}d)Y_n(k_{t1}a)}\,. \tag{4.17}$$

and $'$ denotes the derivatives with respect to the argument. Similarly the normal components of the Green's function, where the source point is on the surface ($\rho'=d$) and the observation point is inside the dielectric region, can be written as [33]

$$G_{\rho\phi} = j\frac{Z_0}{k_0}\left\{\frac{jn}{\rho}\left[\frac{T_c^2}{\epsilon_r-1}-\frac{k_0^2 k_{t0} R_n T_m}{k_{t1}^2}\right]\frac{C_n^{pr1}}{T} + \frac{jk_z}{T}\left(\frac{nk_z}{dk_{t1}^2}\right)\left(\frac{k_{t0}^2}{k_{t1}^2}\right)(C_n^e - k_{t0}R_n)k_{t1}C_n^{pr2}\right\} \tag{4.18}$$

$$G_{\rho z} = \frac{jZ_0}{k_0}\left\{\frac{-jn}{\rho}\left(\frac{k_{t0}^2}{k_{t1}^2}\right)\frac{k_0 T_c C_n^{pr1}}{T} + \frac{jk_z}{T}\left(\frac{k_{t0}^2}{k_{t1}^2}\right)T_e k_{t1} C_n^{pr2}\right\} \tag{4.19}$$

$$C_n^{pr1} = \frac{J_n'(k_{t1}a)Y_n(k_{t1}\rho) - J_n(k_{t1}\rho)Y_n'(k_{t1}a)}{J_n'(k_{t1}a)Y_n(k_{t1}d) - J_n(k_{t1}d)Y_n'(k_{t1}a)} \tag{4.20}$$

$$C_n^{pr2} = \frac{J_n(k_{t1}a)Y_n'(k_{t1}\rho) - J_n'(k_{t1}\rho)Y_n(k_{t1}a)}{J_n(k_{t1}a)Y_n(k_{t1}d) - J_n(k_{t1}d)Y_n(k_{t1}a)}\,. \tag{4.21}$$

Expressions involving Bessel and Hankel functions and their derivatives suffer instability issues due to the large order (n) and argument of these functions. These functions are evaluated using closed-form expressions which are written by employing their Debye approximations and Olver's uniform representations. These closed-form approximations can be found in [33].

4.2 Spatial Domain Representation of Green's Function for Cylindrical Grounded Dielectric Slabs

Similar to the planar case, spectral domain expressions become extremely inefficient and yield inaccurate results when the geometry under interest becomes electrically large. Therefore, spatial domain hybrid MoM/Green's function technique is preferred to investigate the printed arrays on electrically large coated cylinders. To achieve the desired efficiency and accuracy in this method (in electrically large geometries), three spatial domain Green's function representations

are used interchangeably based on where each representation yields the most accurate result in a most efficient way. These Green's function representations are

(i) Planar approximations for the source region, which are explained in a detailed way in the previous chapter,

(ii) The steepest descent path (SDP) representation, which is briefly explained in the following subsection (4.2.1) and

(iii) The Fourier series representation, which is briefly explained in subsection (4.2.2).

4.2.1 Steepest Descent Path (SDP) Representation of the Green's Function

This representation is based on the circumferentially propagating series representation of the appropriate Green's function and its efficient numerical evaluation along a steepest descent path (SDP) on which the integrand decays most rapidly ([33],[40]).

Consider an infinitesimal surface current distribution $\mathbf{J}$ on the air-dielectric interface, which can be written as

$$\mathbf{J} = \mathbf{P_e} \frac{\delta(\phi - \phi')\,\delta(z - z')}{\rho'} \tag{4.22}$$

where $\mathbf{P_e} = P_e^z \hat{x} + P_e^\phi \hat{\phi}$ and its Fourier transform $\tilde{\mathbf{J}}$ is given by

$$\tilde{\mathbf{J}} = \frac{\mathbf{P_e}}{2\pi d} e^{jk_z z'} e^{jn\phi'} \,. \tag{4.23}$$

Using (4.1), (4.2) and (4.3), the surface electric field due to this current distribution is given by

$$E_l(\phi,z)=\frac{1}{4\pi^2 d}\sum_{n=-\infty}^{\infty}e^{jn(\phi-\phi')}\left\{\int_{-\infty}^{\infty}\tilde{G}_{lu}(n,k_z)P_e^u e^{jk_z(z-z')}\,dk_z\right\} \tag{4.24}$$

where $\hat{u}$ ($\hat{u}=\hat{\phi}$, $\hat{z}$ or $\hat{\rho}$) represents the source direction and $\hat{l}$ ($\hat{l}=\hat{\phi}$, $\hat{z}$ or $\hat{\rho}$) represents the observation direction (we did not consider the $\hat{l}\hat{u}=\hat{z}\hat{z}$ case) and $\tilde{G}_{lu}(n,k_z)$ is the corresponding component of the appropriate dyadic Green's function in the spectral-domain. Watson transform is applied to (4.24) in order to represent the electric field as a sum of circumferentially propagating waves given by

$$\begin{aligned}E_l(\phi,z) &= \frac{1}{4\pi^2 d}\int_{-\infty}^{\infty}dk_z e^{-jk_z(z-z')}\\ &\quad\left\{\int_{-\infty-j\epsilon}^{\infty-j\epsilon}G_{lu}(k_z,\nu)P_e^u\left(\sum_{p=-\infty}^{\infty}e^{-j\nu[(\phi-\phi')-2\pi p]}\right)d\nu\right\}.\end{aligned} \tag{4.25}$$

For an electrically large cylinder, the terms other than $p=0$ can be neglected since they represent the multiple wave encirclements which loose their strength as they travel on the surface of the cylinder. Therefore, taking only the term corresponding to $p=0$ is enough for most cases. The resulting expression for the electric field is given by

$$E_l(\phi,z)=\frac{1}{2\pi}\int_{-\infty}^{\infty}dk_z e^{-jk_z(z-z')}\left\{\int_{-\infty-j\epsilon}^{\infty-j\epsilon}G_{lu}(k_z,\nu)P_e^u e^{-j\nu(\phi-\phi')}d\nu\right\}. \tag{4.26}$$

Before applying the SDP method we perform a Fock type substitution and the employ polar transformations given by

$$\nu=k_{t0}d+m_t\tau \tag{4.27}$$

where

$$m_t=\left(\frac{k_{t0}d}{2}\right)^{\frac{1}{3}} \tag{4.28}$$

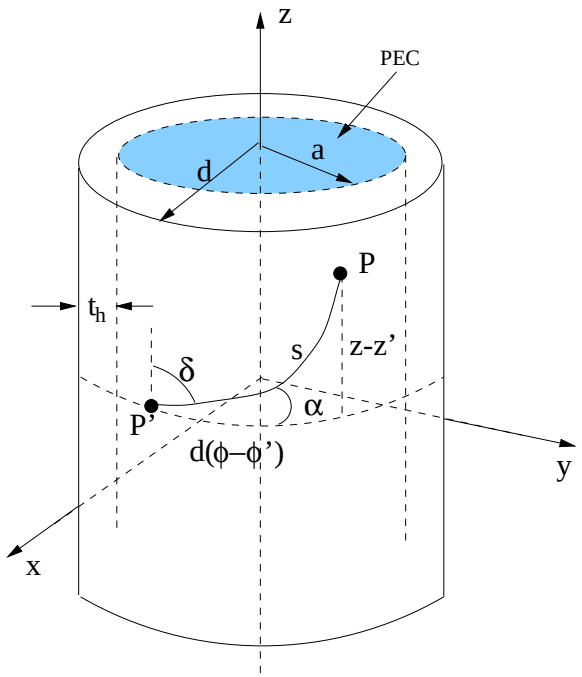

Figure 4.1: The cylindrical geometry

and

$$k_z = k_0 \sin(\psi) \tag{4.29}$$

$$k_{t0} = k_0 \cos(\psi)\,. \tag{4.30}$$

Using the geometrical relations, shown in Fig. 4.1, given by

$$z - z' = s \sin(\alpha) \tag{4.31}$$

$$d(\phi - \phi') = s \cos(\alpha) \tag{4.32}$$

with s being the arc length of the geodesic path between source and observation points on the surface of the coating and α being the angle between s and the circumferential axis, the following expression for the electric field is obtained:

$$E_l(\alpha,s) \approx \frac{1}{4\pi^2 d}\int_{C_\Psi} d\psi k_0\cos(\psi)e^{-jk_0 s\sin(\psi)sin\alpha} \left(\int_{C_\tau} G_{lu}(\psi,\tau)P_e^u e^{-jk_0 s\cos(\psi)cos(\alpha)}e^{-jm_t\tau(\phi-\phi')}m_t d\tau\right). \quad (4.33)$$

Integration contour C_ψ can be deformed into its steepest decent path as shown in Fig. 4.2 where the integrand decays most rapidly as explained in [33]. Resultant expressions for the electric field is given as

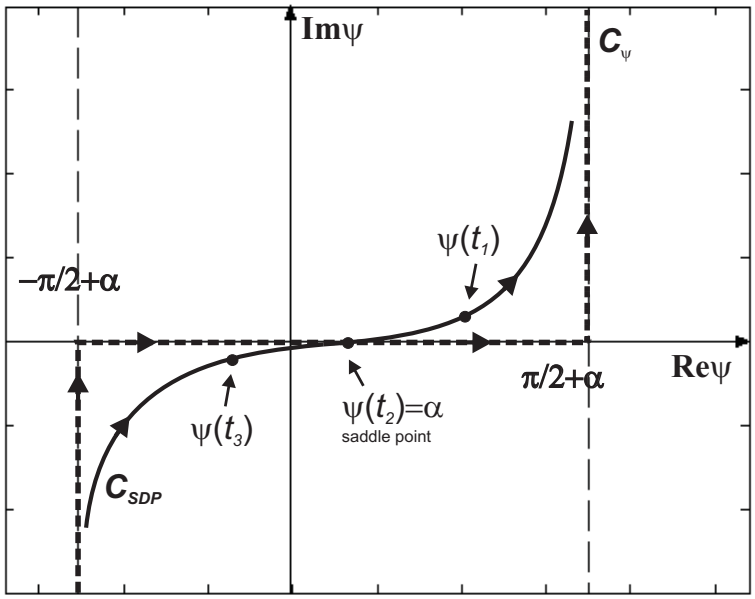

Figure 4.2: SDP path

$$E_l(\alpha,s) \approx \frac{\sqrt{2}e^{-j3\pi/4}}{4\pi^2 d}\frac{e^{-jk_0 s}}{\sqrt{k_0 s}}\int_{-\infty}^{\infty} dt\, e^{-t^2}\tilde{F}(\alpha,s,t) \quad (4.34)$$

where

$$\tilde{F}(\alpha, s, t) = \frac{k_0 cos\psi(t)}{cos\left(\frac{\alpha-\psi(t)}{2}\right)} \int_{C_\tau(t)} G_{lu}(\tau, t) P_e^u m_t e^{-j\xi\tau}\, d\tau \tag{4.35}$$

$$\psi(t) = \alpha - 2\arcsin\left(\frac{te^{j\pi/4}}{\sqrt{2}\sqrt{k_0 s}}\right) \tag{4.36}$$

and

$$\xi = m_t(\phi - \phi'). \tag{4.37}$$

In (4.34) and (4.35), explicit expressions for G_{lu} can be obtained from (4.8) - (4.10) with n is replaced by ν which is related to τ by (4.27).

4.2.2 Numerical evaluation of the Integrals for the SDP Representation

The surface wave expression given by (4.34) and (4.35) includes two integrals in the t and τ domains which are evaluated numerically. In the t domain, the integration is performed using a Gauss-Hermite quadrature algorithm, whereas in the τ domain, Filon's algorithm is used in conjunction with a Gaussian Quadrature integration algorithm, and a proper tail is added when necessary. Implementation of the Gauss-Hermite integration procedure to (4.34) and (4.35) yields the following expressions for the surface fields:

$$\begin{aligned} E_\phi(\alpha, s) \;\approx\; & \frac{\sqrt{2}e^{-j3\pi/4}}{4\pi^2 d} \frac{e^{-jk_0 s}}{\sqrt{k_0 s}} \sum_{q=1}^{Q} w_q \frac{k_0 \cos[\psi(t_q)] m_t}{\cos\left[\frac{\alpha-\psi(t_q)}{2}\right]} \\ & \times \left[\int_{C_{\tau(t_q)}} (G_{\phi\phi}(\tau, t_q) P_e^\phi + G_{\phi z}(\tau, t_q) P_e^z) e^{-j\xi\tau} d\tau\right] \end{aligned} \tag{4.38}$$

$$E_z(\alpha,s) \approx \frac{\sqrt{2}e^{-j3\pi/4}}{4\pi^2 d}\frac{e^{-jk_0 s}}{\sqrt{k_0 s}}\sum_{q=1}^{Q} w_q \frac{k_0\cos[\psi(t_q)]m_t}{\cos\left[\frac{\alpha-\psi(t_q)}{2}\right]} \times\left[\int_{C_{\tau(t_q)}}(G_{z\phi}(\tau,t_q)P_e^{\phi}+G_{zz}(\tau,t_q)P_e^{z})e^{-j\xi\tau}d\tau\right] \quad (4.39)$$

$$E_\rho(\alpha,s) \approx \frac{\sqrt{2}e^{-j3\pi/4}}{4\pi^2 d}\frac{e^{-jk_0 s}}{\sqrt{k_0 s}}\sum_{q=1}^{Q} w_q \frac{k_0\cos[\psi(t_q)]m_t}{\cos\left[\frac{\alpha-\psi(t_q)}{2}\right]} \times\left[\int_{C_{\tau(t_q)}}(G_{\rho\phi}(\tau,t_q)P_e^{\phi}+G_{\rho z}(\tau,t_q)P_e^{z})e^{-j\xi\tau}d\tau\right]. \quad (4.40)$$

Q is typically chosen to be 1, 3 or 5 (or rarely more) for a desired accuracy, depending on the geometry parameters. In some cases even $Q = 1$ (saddle point contribution) is enough for a highly accurate solution. However, the main difficulty comes from the evaluation of the τ-integral. Therefore, special care should be given to the efficient evaluation of the τ-integrals. As a first step, the $(-\infty - j\epsilon, +\infty - j\epsilon)$ integration in the ν-domain, whose path is shown in Fig. 4.3, is considered and part of it denoted by C_1 is deformed toward the third quadrant assuming that there is no pole or branch-point singularities in this quadrant. Consequently, the original contour $C = C_1 + C_2$ is now $\tilde{C} = \tilde{C}_1 + C_2$. Then, using (4.27) the integration path $\tilde{C}$ in the ν-domain is mapped to τ domain and $C_\tau(t_q)$ is obtained. However, the integration contour $C_\tau(t_q)$ should be updated for each t_q value. An example is given in Fig. 4.4 for $Q = 3$ case, where for t_1, t_2 and t_3 values used in the SDP integration, shown in Fig. 4.2, the corresponding $C_\tau(t_1)$, $C_\tau(t_2)$ and $C_\tau(t_3)$ paths are illustrated in Fig. 4.4. However, the integrands in the τ-domain exhibit a highly oscillatory and slowly decaying nature. Therefore, a proper integration routine is necessary to handle the oscillatory behavior of the integrand whereas an appropriate tail is used to handle its slowly decaying nature. Besides, deformation of the path from C to $\tilde{C}$ provides an exponential decay and hence, a very rapid convergence of the integrand along the third quadrant.

Consequently, first the integration contour is divided into three parts as it is shown in Fig. 4.5. C_τ^- represents the part where the integrand converges fast due

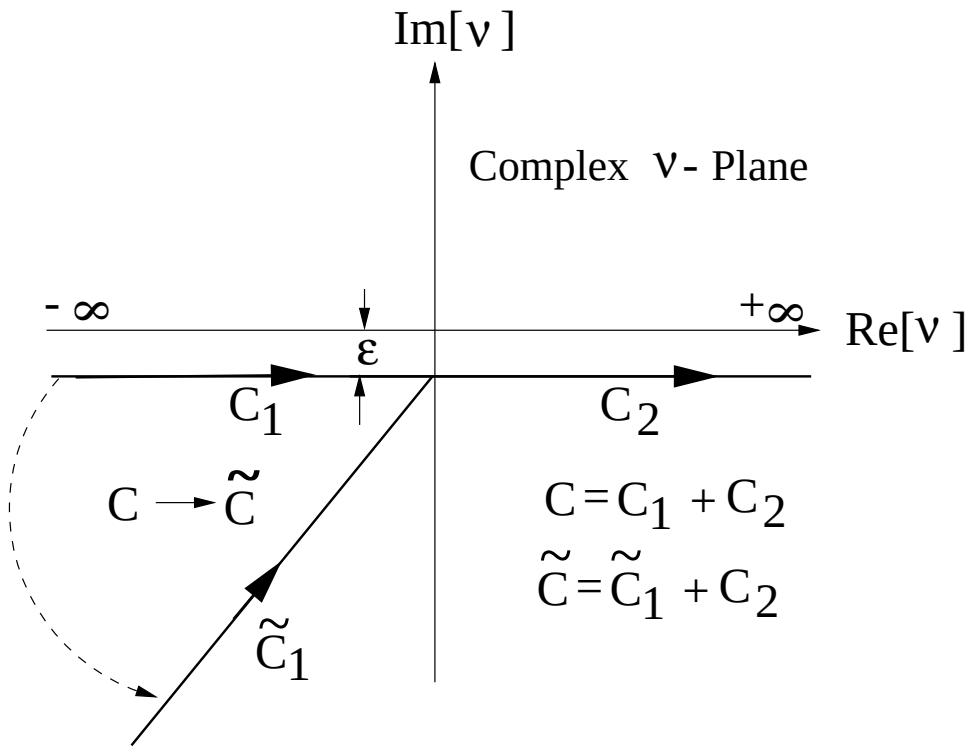

Figure 4.3: Integration contour in the ν-domain

to an exponential decay, while the C_τ^+ part has a slower convergence. After the τ' value, which is relatively big, the integrand is approximated by its asymptotic value and the resultant integral is evaluated in closed-form which we call as the tail contribution. Note that this method fails for the $\phi - \phi$ case. Therefore, in that case we performed an envelope extraction method with respect to τ. As a result the τ integrals for the z-z, ϕ-z and ϕ-ϕ cases are called I_1, I_2 and I_3, and they are given by

$$\begin{aligned} I_1 &= C_1\Bigg[\int_{C_\tau^-(t_q)} G_{zz}(t_q,\tau)P_e^z e^{-j\xi\tau}d\tau + \int_{\tilde{\tau}}^{\tau'} G_{zz}(t_q,\tau)P_e^z e^{-j\xi\tau}d\tau \\ &\quad + \int_{\tau'}^{\hat{p}_q\infty} \frac{B_1}{\tau}P_e^z e^{-j\xi\tau}d\tau\Bigg]. \end{aligned} \tag{4.41}$$

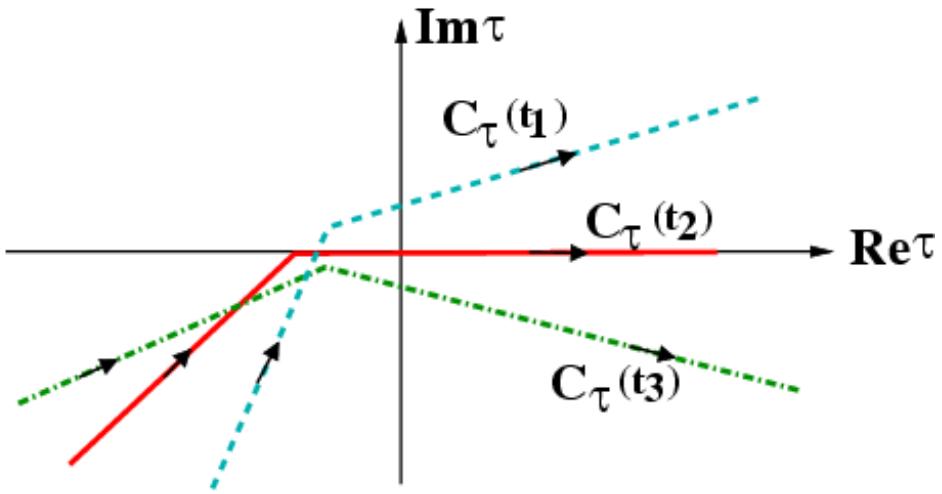

Figure 4.4: Integration contours in the τ-domain

$$I_2 = C_1\Bigg[\int_{C_\tau^-(t_q)} G_{\phi z}(t_q,\tau)P_e^z e^{-j\xi\tau}d\tau + \int_{\tilde{\tau}}^{\tau'} G_{\phi z}(t_q,\tau)P_e^z e^{-j\xi\tau}d\tau + \int_{\tau'}^{\hat{p}_q\infty} \frac{B_1}{\tau}P_e^z e^{-j\xi\tau}d\tau\Bigg]. \tag{4.42}$$

$$\begin{aligned} I_3 = C_1\Bigg[&\int_{C_\tau^-(t_q)} G_{\phi\phi}(t_q,\tau)P_e^\phi e^{-j\xi\tau}d\tau \\ &+ \int_{C_\tau^+(t_q)} \left(G_{\phi\phi}(t_q,\tau) - B_2\tau - B_3\right)P_e^\phi e^{-j\xi\tau}d\tau \\ &+ \int_{C_\tau^+(t_q)} B_2\tau P_e^\phi e^{-j\xi\tau}d\tau + \int_{C_\tau^+(t_q)} B_3 P_e^\phi e^{-j\xi\tau}d\tau\Bigg]. \end{aligned} \tag{4.43}$$

The constants B_1, B_2, B_3 and C_1 are given in [33]. Probe related integrals are performed similarly [33]. Tail integrals are evaluated in closed-form and given by [33]

$$F_1(\tau') = \int_{\tau'}^{\hat{p}_i\infty} \frac{B_1}{\tau}e^{-j\xi\tau}d\tau \approx B_1\frac{e^{-j\xi\tau'}}{j\xi\tau'}. \tag{4.44}$$

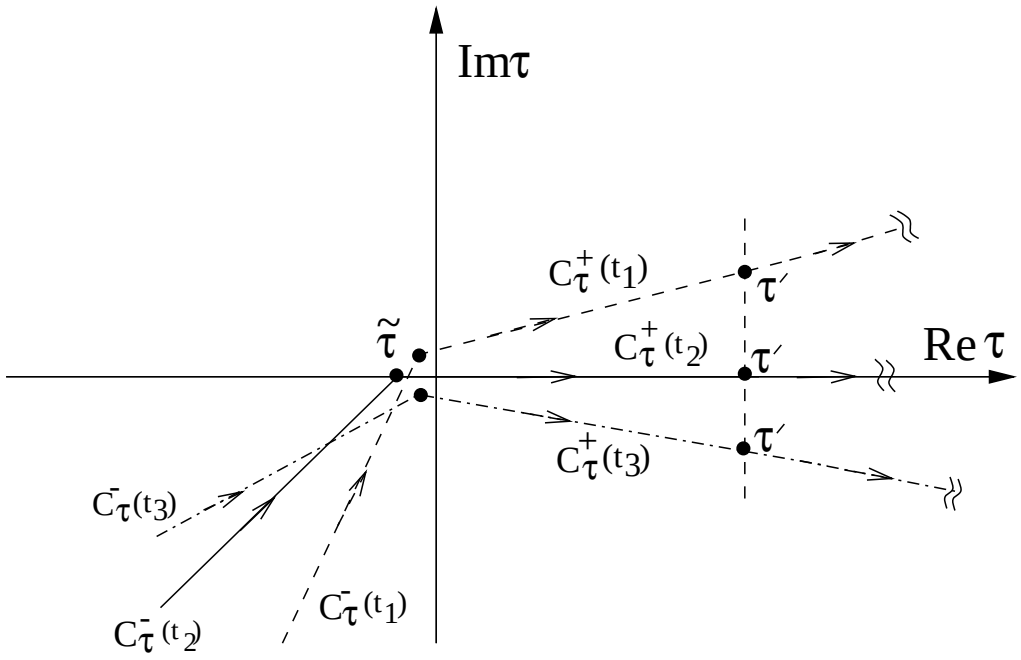

Figure 4.5: Integration contour in the τ-domain

$$F_2(\tau') = \int_{C_\tau^+(tq)} B_2 \tau e^{-j\xi\tau} d\tau \approx -B_2 \left[\frac{j\xi\tilde{\tau} e^{-j\xi\tilde{\tau}} + e^{-j\xi\tilde{\tau}}}{\xi^2} \right] \tag{4.45}$$

$$F_3(\tau') = \int_{\tau'}^{\hat{p}_i \infty} B_3 e^{-j\xi\tau} d\tau \approx B_3 \frac{e^{-j\xi\tau'}}{j\xi} \tag{4.46}$$

Finally, on each interval along the τ contour, where integrals are evaluated numerically, we used Filon's algorithm in conjunction with a Gaussian quadrature technique to handle their oscillatory nature. Further details can be found in [33]

4.2.3 Fourier Series Representation of Green's Functions

As it is mentioned earlier, SDP representation is not valid in the paraxial region (nearly axial region). In this region Fourier series representation of the Green's function is used [33],[41], which is relatively fast and accurate along this region. Besides, certain components can be made accurate and can be evaluated efficiently away from the paraxial region after performing some modifications.

Derivation of this representation of the Green's function starts by using the following transformations in (4.26):

$$\begin{aligned} k_z &= -\zeta\cos(\psi) && (4.47)\\ \nu &= \mu d && (4.48)\\ \mu &= -\zeta\sin(\psi) && (4.49) \end{aligned}$$

and

$$\begin{aligned} r_l &= d(\phi-\phi') = s\sin(\delta) && (4.50)\\ (z-z') &= s\cos(\delta) && (4.51) \end{aligned}$$

where $\delta = (90-\alpha)$, in (4.26). The resultant expression for the electric field becomes

$$E_l(s,\delta) \approx \frac{1}{2\pi}\int_0^{2\pi}\int_0^{\infty}\frac{G_{lu}(\zeta,\psi)}{2\pi}e^{j\zeta s\cos(\psi-\delta)}\zeta d\zeta d\psi. \qquad (4.52)$$

Note that, all the tangential components of the Green's function representation are periodic with respect to ψ with a period π such that [33]

$$\begin{aligned} G_{zz}(\zeta,\psi) &= G_{zz}(\zeta,\psi+\pi) && (4.53)\\ G_{\phi\phi}(\zeta,\psi) &= G_{\phi\phi}(\zeta,\psi+\pi) && (4.54)\\ G_{\phi z}(\zeta,\psi) &= G_{\phi z}(\zeta,\psi+\pi) && (4.55)\\ G_{z\phi}(\zeta,\psi) &= G_{z\phi}(\zeta,\psi+\pi)\,. && (4.56) \end{aligned}$$

Using this periodicity, the Green's functions components can be approximated by a Fourier series given by

$$G_{lu}(\zeta,\psi) = a_0(\zeta) + \sum_{n=1}^{\infty}a_n(\zeta)\cos(n2\psi) + \sum_{n=1}^{\infty}b_n(\zeta)\sin(n2\psi) \qquad (4.57)$$

where

$$a_0(\zeta) = \frac{1}{\pi}\int_T G_{lu}(\zeta,\psi)d\psi \tag{4.58}$$

$$a_n(\zeta) = \frac{2}{\pi}\int_T G_{lu}(\zeta,\psi)\cos(n2\psi)d\psi \tag{4.59}$$

$$b_n(\zeta) = \frac{2}{\pi}\int_T G_{lu}(\zeta,\psi)\sin(2\psi)d\psi\,. \tag{4.60}$$

Using these relations and approximating the Fourier series coefficients via a trapezoidal rule (explained in detail in [33]), approximate Green's function components are given by

$$\begin{aligned} G^a_{zz}(\zeta,\psi) \approx\ & G_{zz}(\zeta,\psi=\frac{\pi}{2}) \\ & + \left[G_{zz}(\zeta,\psi=0) - G_{zz}(\zeta,\psi=\frac{\pi}{2})\right]\left(\frac{1+\cos(2\psi)}{2}\right) \end{aligned} \tag{4.61}$$

$$G^a_{\phi z}(\zeta,\psi) \approx \frac{\zeta^2\sin(2\psi)}{2}\tilde{G}_{\phi z}(\zeta,\psi=0) \tag{4.62}$$

$$\begin{aligned} G^a_{\phi\phi}(\zeta,\psi) \approx\ & G^{p1}_{uu}(\zeta) + \frac{1}{2}G^{cc}_{\phi\phi}(\zeta,\psi=0) + \Big\{ -\zeta^2 G^{p2}_{uu}(\zeta) \\ & + \frac{1}{2}\left[G^{cc}_{\phi\phi}(\zeta,\psi=\frac{\pi}{2}) - G^{cc}_{\phi\phi}(\zeta,\psi=0)\right]\Big\}\left(\frac{1-\cos(2\psi)}{2}\right) \end{aligned} \tag{4.63}$$

where

$$G_{\phi z}(\zeta,\psi) = \frac{\zeta^2\sin(2\psi)}{2}\tilde{G}_{\phi z}(\zeta,\psi) \tag{4.64}$$

and

$$G_{\phi\phi}(\zeta,\psi) \approx G^p_{uu}(\zeta,\psi) + G^{cc}_{\phi\phi}(\zeta,\psi) \tag{4.65}$$

$$G^p_{uu}(\zeta,\psi) = G^{p1}_{uu}(\zeta) - G^{p2}_{uu}(\zeta)\left(\frac{1-\cos(2\psi)}{2}\right)\zeta^2\,. \tag{4.66}$$

Note that $G_{\phi\phi}$ is written as a sum of planar+curvature terms in (4.65) as explained in [33]. Superscripts 'p' stands for the planar term, whereas 'cc' denotes these curvature terms. Planar term is the component of the Green's function for a planar grounded dielectric substrate. (4.63) is obtained by inserting the approximate expression for the curvature correction term given by:

$$G_{\phi\phi}^{a,cc}(\zeta,\phi) \approx \frac{1}{2}\Bigg\{ G_{\phi\phi}^{cc}(\zeta,\psi=0) \tag{4.67}$$

$$+\left[G_{\phi\phi}^{cc}(\zeta,\psi=\frac{\pi}{2}) - G_{\phi\phi}^{cc}(\zeta,\psi=0)\right]\left(\frac{1-2\cos(2\psi)}{2}\right)\Bigg\}. \tag{4.68}$$

Also notice that the ζ and ψ variables are separated. By using the approximate Green's function representations (4.61)-(4.63) in (4.52) and performing the ψ integration in closed-form, the resulting surface fields are written as

$$E_{zz}(\delta,s) \approx \frac{-Z_0}{2\pi k_0}\left\{k_0^2 P(s) + \frac{\partial^2}{\partial z^2}[P(s)-Q(s)]\right\} \tag{4.69}$$

$$E_{\phi z}(\delta,s) \approx \frac{-Z_0}{2\pi k_0}\frac{\partial^2}{\partial z \partial r_l}\{M(s)-R(s)\} \tag{4.70}$$

$$E_{\phi\phi}(\delta,s) \approx \frac{-Z_0}{2\pi k_0}\left\{k_0^2 U(s) + \frac{\partial^2}{\partial r_l^2}\left[U(s) - \frac{\epsilon_r - 1}{\epsilon_r}W(s)\right]\right\}$$

$$+\frac{jZ_0}{4\pi k_0}\left\{S(s) - \frac{\partial^2}{\partial r_l^2}T(s)\right\}. \tag{4.71}$$

Explicit expressions for the special functions $P(s)$, $Q(s)$, $M(s)$, $R(s)$, $U(s)$, $W(s)$, $S(s)$ and $T(s)$ is given in [33].

As it is mentioned earlier, with a few modifications, Fourier series representation of the Green's function components ($G_{\phi z}$ and $G_{\phi\phi}$) can become valid in the region away from the paraxial region. In the evaluation of the Fourier coefficients, using different number of points in the trapezoidal rule, which is explained in detail in [33], accurate Green's representations can be obtained away from the paraxial region. The accurate approximations of $G_{\phi z}$ and $G_{\phi\phi}$ for the angles $\delta \to \pi/2$ is given by

$$G_{\phi z}^{a2}(\zeta,\psi) \approx \frac{\zeta^2 \sin(2\psi)}{2}\tilde{G}_{\phi z}(\zeta,\ \psi=\pi/2)$$

$$G_{\phi\phi}^{a2,\,cc}(\zeta,\psi) \approx G_{\phi\phi}^{cc}(\zeta,\psi=0) + \left[G_{\phi\phi}^{cc}(\zeta,\psi=\frac{\pi}{2}) - G_{\phi\phi}^{cc}(\zeta,\psi=0)\right]\left(\frac{1-cos2\psi}{2}\right). \quad (4.72)$$

On the other hand for the angles around $\delta = \pi/4$

$$G_{\phi z}^{a2}(\zeta,\psi) \approx \frac{\zeta^2 \sin(2\psi)}{2}\left[\frac{\tilde{G}_{\phi z}(\zeta,\ \psi=0)+\tilde{G}_{\phi z}(\zeta,\ \psi=\pi/2)}{2}\right] \quad (4.73)$$

$$G_{\phi\phi}^{cc}(\zeta,\psi) \approx \frac{3}{4}\Bigg\{G_{\phi\phi}^{cc}(\zeta,\psi=0) + \left[G_{\phi\phi}^{cc}(\zeta,\psi=\frac{\pi}{2}) - G_{\phi\phi}^{cc}(\zeta,\psi=0)\right]\left(\frac{1-cos2\psi}{2}\right)\Bigg\} \quad (4.74)$$

are the expressions that are used for the curvature correction term.

The Fourier Series representation of the Green's function is more accurate when the separation between the source and the observation point is small (except the paraxial region). Also, since the integration is only with respect to the variable ζ, it is computationally very efficient. For some geometric parameters it is preferable to use the Fourier Series representation of the $G_{\phi\phi}$ in the off-paraxial region for small separations, instead of the SDP representation due to its efficiency compared to SDP representation at this region.

4.3 Limitations of the Green's Function Representations for Cylindrical Grounded Dielectric Slab and the Switching Algorithm

In this section we briefly discuss the limitations of the Green's function representations in particular the SDP and the paraxial representations. Efficiency and accuracy of these representations are previously discussed in [41], [42]. These limitations are manifested in the electrical size (i.e. the radius) of the coated cylinder and/or in the thickness of the coating. Note that the dielectric constant of the coating can always be linked to the thickness. First of all, the SDP and the paraxial representations are developed for electrically large coated cylinders. Therefore, the desired accuracy is generally achieved when the radius is greater than $1\lambda_0$ (λ_0: free space wavelength). This is illustrated in Fig. 4.6, where the mutual coupling between two identical $\hat{z}$-directed and $\hat{\phi}$-directed current modes are plotted as a function of the inner radius a, and compared with the eigenfunction solution (spectral domain solution). The current modes are selected to be $(L, W) = (0.39\lambda_0, 0.01\lambda_0)$, the thickness is chosen as $0.06\lambda_0$ and the relative dielectric constant of the coating is set to 3.25. The couplings are evaluated at $s = 1.5\lambda_0$. The eigenfunction solution is plotted up to $a = 5\lambda_0$ since it exhibits serious convergence problems for greater radii. As expected, Green's function representations show excellent agreement with the eigenfunction solution (even for $a = 1\lambda_0$). The small difference in the $\phi - \phi$ coupling in Fig. 4.6(b) (especially at $a = 5\lambda_0$) is due to the convergence problems of the eigenfunction solution. Furthermore, the results approach to the planar case with the increasing cylinder radius without exhibiting any problems. On the other hand, these Green's function representations loose their accuracy when the thickness and/or relative dielectric constant of the coating increase. This is due the Debye, Watson and Olver's uniform approximations, made for the ratios of special functions (4.15), (4.16), (4.17), (4.20) and (4.21) as explained in detail in [40] and [33]. For the desired accuracy, an approximate upper limit is defined in [33] such that the thickness of the coating must be less than $0.2\lambda_d$, where $\lambda_d = \lambda_0/\sqrt{\epsilon_r}$.

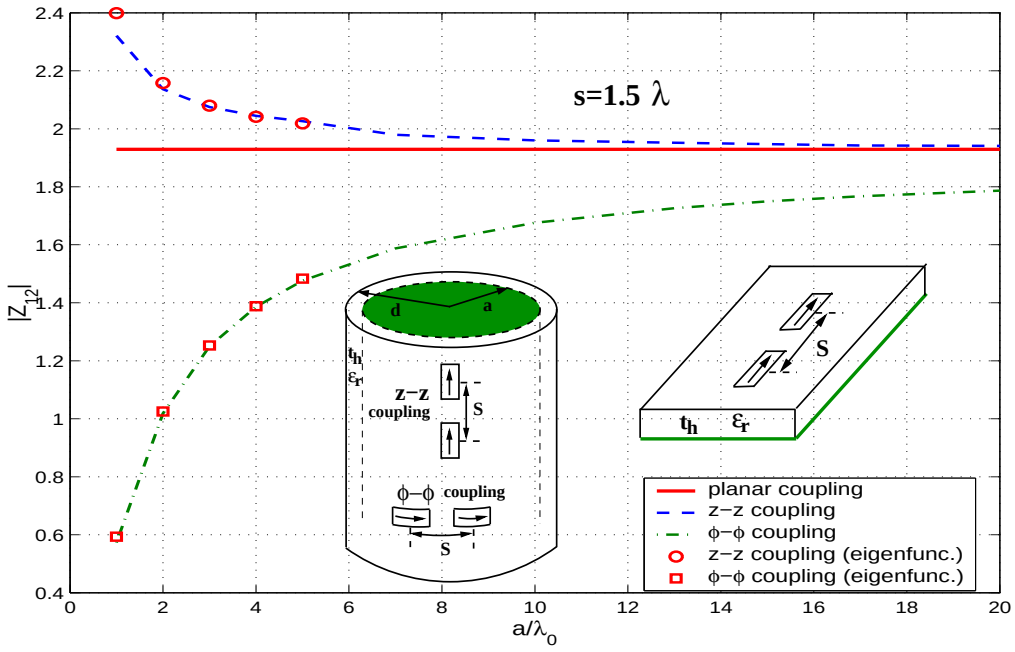

(a)

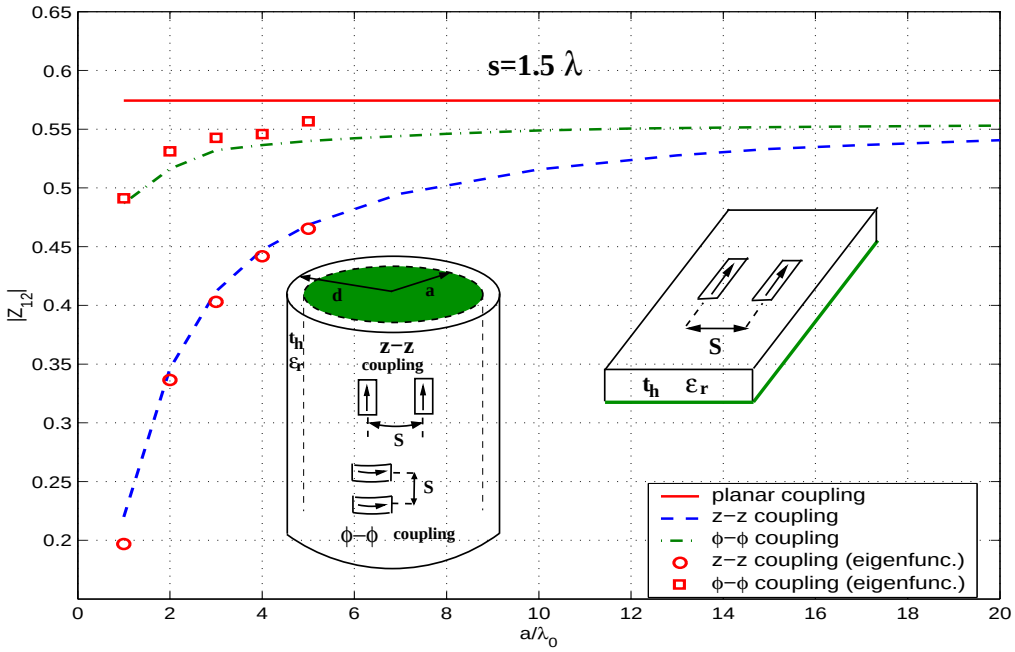

(b)

Figure 4.6: Magnitude of the mutual coupling, $|Z_{12}|$, between two identical $\hat{z}$-directed and $\hat{\phi}$-directed current modes versus inner radius a evaluated at $s = 1.5\lambda_0$ for $t_h = 0.06\lambda_0$ and $\epsilon_r = 3.25$ along the (a) E-plane and (b) H-plane. The size of the current modes is: $(L, W) = (0.39\lambda_0, 0.01\lambda_0)$.

Finally, these three Green's function representations are combined to span the whole cylinder surface using two slightly different switching algorithms for the arrays of $\hat{z}-$ and $\hat{\phi}-$directed printed dipoles. In both algorithms, the air-dielectric interface of the cylinder is divided into three regions and on each region, the corresponding aforementioned Green's function representation is used. For the array of $\hat{z}-$directed printed dipoles, the switching algorithm is given by

$$G_{zz} = \begin{cases} \text{Planar representation} & s < 0.4\lambda_0 \text{ (i.e self-term evaluations)} \\ \text{SDP representation} & (\xi_{SP}/s > 0.2) \bigcap (s \geq 0.4\lambda_0) \\ \text{Paraxial representation} & (\xi_{SP}/s \leq 0.2) \bigcap (s \geq 0.4\lambda_0) \end{cases} \tag{4.75}$$

which is similar to the switching algorithm used in [42]-[43], previously. However, the switching algorithm used for the array of $\hat{\phi}-$directed printed dipoles is different than the switching algorithm given in [42] and [44], and can be expressed as

$$G_{\phi\phi} = \begin{cases} \text{Planar representation} & s < 0.4\lambda_0 \text{ (i.e self-term evaluations)} \\ \text{SDP representation} & (\xi_{SP}/s > 0.2) \bigcap (s \geq 2\lambda_0) \\ \text{Paraxial representation} & [(\xi_{SP}/s \leq 0.2) \bigcap (s \geq 0.4\lambda_0) \text{ or} \\ & (\xi_{SP}/s > 0.2) \bigcap (0.4\lambda_0 \leq s < 2\lambda_0)] \ . \end{cases} \tag{4.76}$$

In both (4.75) and (4.76), ξ_{SP} is the saddle point value of (4.37) and is given by $\xi_{SP} = \left(\frac{d\, k_0 \cos\alpha}{2}\right)^{\frac{1}{3}} (\phi - \phi')$ in [40] with α being the angle between the ray path and the circumferential axis. Furthermore, around each boundary which divides the regions defined in (4.75) and (4.76), more than one Green's function representation yield almost the same accuracy. Hence, small variations in boundary definitions do not significantly affect the overall accuracy. Consequently, in addition to its accuracy and has not been used in this thesis, a similar switching algorithm that we have used for the $G_{\phi\phi}$ component is typically suitable for the $G_{\phi z}$ component.

Chapter 5

Scan Blindness Phenomenon in Finite Phased Arrays of Printed Dipoles

5.1 Introduction

Printed antenna arrays on planar or curved surfaces might have many elements on dielectric substrates (or in free space), where electromagnetic coupling through space and surface waves can lead to scan blindness [23] and seriously degrade the performance of a system. This phenomenon was once addressed as a *"catastrophic effect"* by Schaubert et al. [45]. Therefore, a complete understanding of the scan blindness phenomenon is required to improve the scan range of phased arrays and to reduce design costs significantly.

The blindness phenomenon, which was defined (for planar infinite arrays of printed antennas) as a phase matching between the phase progression of a surface wave (β_{sw}) on the dielectric substrate and the phase progression of a certain Floquet mode ([23], [46]), has been previously investigated in detail for various infinite and finite arrays of printed antennas on grounded planar dielectric substrates. The blindness mechanism was carefully explained first for infinite arrays

of printed antennas [23]-[24], [25], and then research on this topic was extended to finite phased arrays of printed antennas [4]-[26]. Later, this phenomenon was discussed for different array configurations such as infinite array of monopoles in a grounded dielectric slab [47], infinite arrays of printed dipoles on dielectric sheets perpendicular to a ground plane [48], infinite stripline-fed tapered slot antenna arrays with a ground plane [45], [49]. Furthermore, various methods to improve the scan range such as subarraying [46], substrate modification [50], loading the array elements with varactor diodes [51] or using shorting posts [52] were reported. However, the common point in all these aforementioned studies is the fact that arrays (infinite or finite) are mounted on planar platforms. Recently, we have presented a rigorous investigation of the scan blindness phenomenon for arrays of printed elements mounted on dielectric coated curved surfaces, where the curvature of the supporting structure affects the blindness mechanism as well as various performance metrics of the array [27].

Therefore, in this chapter, we briefly review [27], where scan blindness phenomenon is investigated for several arrays consisting of finite number of axially and/or circumferentially oriented printed dipoles on various-sized electrically large, dielectric coated, circular cylinders with different electrical parameters. Effects of several array and supporting structure parameters on the scan blindness mechanism as well as on various characteristics of arrays are observed. Furthermore, a one-to-one comparison between arrays of printed dipoles on aforementioned cylinders and arrays of printed dipoles on grounded planar dielectric slabs is made in terms of the blindness phenomenon. It is shown that the orientation of the array elements combined with the curvature effects plays an important role on the behavior of the surface waves, which in turn can alter the scan blindness in these structures. To achieve these goals, a hybrid Method of Moments (MoM)/Green's function technique in the spatial domain which is presented in the previous chapters is used.

Problem geometry, which has been already explained in the beginning of this thesis in Section 2.5, Fig. 2.3, is also illustrated in Fig. 5.1. Some formulation related to the performance metrics of the problem are presented in Section 5.2. Several numerical examples are given in Section 5.3 to demonstrate the effects

of the curvature of the host body (coated cylinder) on the surface waves and blindness mechanism. The importance of the array element orientation with respect to the curvature of the host body is discussed. Furthermore, how several electrical and geometrical parameters of the array together with its supporting structure affect the basic performance metrics of finite arrays of printed dipoles on coated cylinders are investigated.

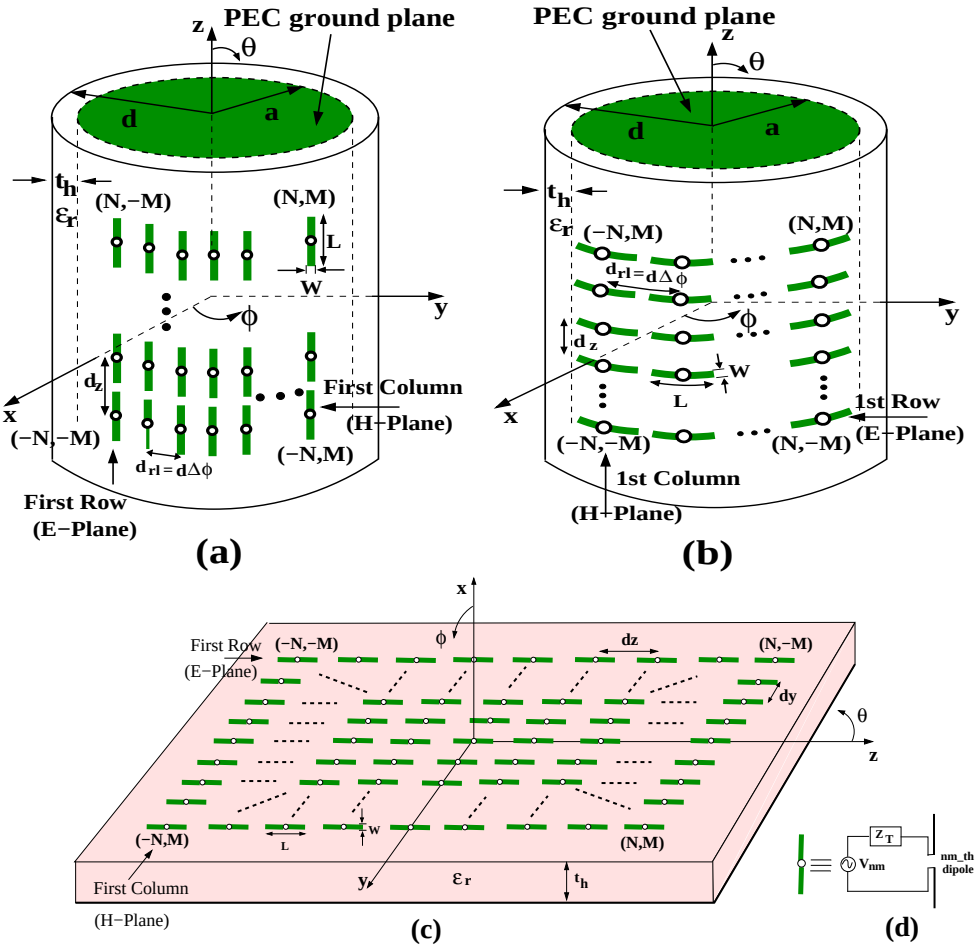

Figure 5.1: Geometries of periodic arrays of $(2N+1)\times(2M+1)$ (a) axially, (b) circumferentially oriented printed dipoles on dielectric coated, electrically large circular cylinders. (c) Geometry of a periodic, planar array of $(2N+1)\times(2M+1)$ printed dipoles. (d) Dipole connected to an infinitesimal generator with a voltage V_{nm} and a terminating impedance Z_T.

5.2 Some Definitions and Far-field Patterns

The full-wave solution used in this study is a hybrid MoM/Green's function technique in the spatial domain as explained in detail in Chapter 4 of this thesis and also in [42]-[44]. By applying Galerkin MoM approach to the EFIE the following matrix equation which is similar (2.7) is obtained in terms of network parameters [4], [43]-[44]:

$$([\mathbf{Z}] + [\mathbf{Z_T}]) \cdot \mathbf{I} = \mathbf{V}. \tag{5.1}$$

In the course of obtaining (5.1), dipoles are assumed to be thin ($W << L$) and a single expansion mode is used to represent the current on each dipole.

In (5.1), $[\mathbf{Z}] = [Z_{nm,pq}]$ is the impedance matrix of the array (2.8) with elements $Z_{nm,pq}$, which denotes the mutual impedance between the nmth and pqth ($-N \leq n,p \leq N$, $-M \leq m,q \leq M$) dipoles and it is given by

$$Z_{nm,pq} = \int_{S_{pq}} ds_{pq} \int_{S_{nm}} ds'_{nm}\; f_{pq}(\mathbf{r}_{pq})\; G_{uu}(\mathbf{r}_{pq}/\mathbf{r}'_{nm})\; f_{nm}(\mathbf{r}'_{nm})\,. \tag{5.2}$$

In (5.2), $f_{nm}(\mathbf{r}'_{nm})$ and $f_{pq}(\mathbf{r}_{pq})$ are the piecewise sinusoidal basis and testing functions (2.19) or (2.20) with $\mathbf{r}_{pq}$ and $\mathbf{r}'_{nm}$ being the position vectors of the pqth and nmth dipoles, respectively, and $G_{uu}(\mathbf{r}_{pq}/\mathbf{r}'_{nm})$ ($u = z$ or ϕ, depending on the orientation of the dipole) is the appropriate component of the dyadic Green's function for arbitrary source and observation locations. In Sections 4.2 and 4.3 accurate and efficient calculation of the Green's function representations is presented in detail. $[\mathbf{Z_T}]$ is the generator terminating impedance matrix which is diagonal [4], $\mathbf{I} = [I_{nm}]$ is the unknown vector of expansion coefficients, and finally $\mathbf{V}$, given by

$$\mathbf{V} = \left[V_{pq} = V_0 e^{-jk_0 d\cos(\phi - p\Delta\phi)\sin\theta} e^{-jk_0 q d_z \cos\theta}\right] \tag{5.3}$$

denotes the excitation of the pqth dipole, where an ideal delta gap generator at the terminal of each center-fed dipole is assumed. Note that (θ, ϕ) in (5.3) is the scan direction of the main beam, and $V_0 = 1$ for uniform excitations similar to [4], [43]-[44]. Furthermore, the Toeplitz property of the matrix $[\mathbf{Z}]$ is employed to

reduce the computational time and LU-decomposition method is applied in the solution of the matrix equation given by (5.1).

By obtaining the mode currents from the solution of matrix equation (5.1), several performance metrics for phased arrays given in [53]-[54], [4] are calculated to investigate scan blindness phenomenon for various cylindrical arrays of printed dipoles. Furthermore, calculated results for these performance metrics are compared with those for planar arrays. Among these performance metrics, the input impedance at the nmth dipole is computed as

$$Z_{in}^{nm} = \frac{V_{nm}}{I_{nm}}\,, \tag{5.4}$$

and is used in the calculation of the active reflection coefficient at the nmth dipole given by

$$R^{nm}(\theta,\phi) = \frac{Z_{in}^{nm}(\theta,\phi) - Z_{in}^{nm}(\theta=90^\circ,\phi=0^\circ)}{Z_{in}^{nm}(\theta,\phi) + Z_{in}^{nm\,*}(\theta=90^\circ,\phi=0^\circ)}\,. \tag{5.5}$$

By defining the active reflection coefficient at the nmth dipole as in (5.5), each array element is conjugate matched to its broadside scan impedance. Note that in some calculations (e.g. to quantify the non-uniformity in the input impedance across the finite array) the active reflection coefficient definition given by (5.5) can be modified, and a fixed element's input impedance at broadside scan can be used as a reference. For instance, if the middle element is chosen as a reference element, then the modified version of (5.5) is given by

$$R_{mid}^{nm}(\theta,\phi) = \frac{Z_{in}^{nm}(\theta,\phi) - Z_{in}^{mid}(\theta=90^\circ,\phi=0^\circ)}{Z_{in}^{nm}(\theta,\phi) + Z_{in}^{mid\,*}(\theta=90^\circ,\phi=0^\circ)}, \tag{5.6}$$

where the subscript/superscript 'mid' stands for the middle element of the array.

Another important metric is the active element pattern $E^{nm}(\theta,\phi)$ (and hence, the active element gain), which is the field radiated by the array when the nmth dipole is excited by a voltage generator, and all other dipoles are terminated in an impedance Z_T [4]. As explained in [4], this pattern gives a very good estimate of the gain pattern of the array even for small finite ones. The active element pattern for the nmth dipole is calculated by setting the feed voltage of this dipole to unity whereas feed voltages for all other dipoles are set to zero. The dipole currents are computed from the solution of (5.1) by setting Z_T equal to the conjugate of the

isolated dipole input impedance. Then the active element pattern for the nmth dipole is calculated as

$$E_{nm}(\theta,\phi) = E^{d}_{nm}(\theta,\phi) \sum_{p=-N}^{N} \sum_{q=-M}^{M} I_{pq} e^{-jk_0 d\cos(\phi - p\Delta\phi)\sin\theta} e^{-jk_0 q d_z \cos\theta} \tag{5.7}$$

where $E^{d}_{nm}(\theta,\phi)$ is the far-field element pattern of a single dipole on a dielectric coated circular cylinder calculated either asymptotically as presented in [55] or using a reciprocity approach as presented in [56]. In both solutions, the dipole current coefficients (I_{nm}) obtained from the solution of (5.1) are used, and both solutions yield exactly the same result. Once the active element pattern is determined, the active element gain of the nmth element is calculated as

$$G_{nm}(\theta,\phi) = \frac{4\pi |E_{nm}(\theta,\phi)|^2}{Z_0 P_{in}} \tag{5.8}$$

where P_{in} is the power delivered to the nmth element given by

$$P_{in} = Re\left\{ \sum_{p=-N}^{N} \sum_{q=-M}^{M} I_{pq} Z_{nm,pq} I^{*}_{nm} \right\} \tag{5.9}$$

and $Z_0 = 120\pi$ is the free-space intrinsic impedance.

Finally, majority of the numerical results for both cylindrical and planar arrays are given in the principle planes, namely, the E- and H-planes. Therefore, making use of Fig. 2.3(a), (b) and (c), where θ and ϕ are defined from the $z-$ and $x-$axis, respectively, the E- and H-planes are defined as follows. For the array of $\hat{z}-$directed printed dipoles on coated cylinders and array of printed dipoles on planar grounded dielectric slabs, as depicted in Fig. 2.3(a) and (c), respectively, E-plane is the xz plane and H-plane is the xy plane. Hence, to scan the E-plane ϕ is set to 0° and θ is varied, whereas to scan the H-plane θ is set to 90° and ϕ is varied. However, for the array of $\hat{\phi}-$directed printed dipoles on coated cylinders, as depicted in Fig. 2.3(b), E-plane is the xy plane and H-plane is the xz plane. Thus, to scan the E-plane θ is set to 90° and ϕ is varied, whereas to scan the H-plane ϕ is set to 0° and θ is varied.

5.3 Numerical Results and Discussion

Numerical results are presented (i) to demonstrate effects of the curvature combined with array element orientation on the surface waves and scan blindness mechanism; (ii) to investigate effects of several electrical and geometrical parameters of arrays together with their host platforms on the aforementioned performance metrics. In all results presented in this paper, the size of each dipole is selected to be $(L, W) = (0.39\lambda_0, 0.01\lambda_0)$, the periodicity of arrays is chosen to be $0.5\lambda_0$ (i.e. $d_z = d_{rl} = d_y = 0.5\lambda_0$), and finally $\epsilon_r = 3.25$ is used. Furthermore, all the cylindrical arrays are excited using the right hand side of (5.3). A similar excitation is used for the planar arrays ([4]).

The numerical results depicted in Fig. 5.2(a) and Fig. 5.2(b) show the magnitude of the reflection coefficient $|R|$ (defined in (5.5)) versus scan angle in the E- and H-planes, respectively. The arrays are 11×11 $\hat{z}-$ and $\hat{\phi}-$directed printed dipoles on a $3\lambda_0$ coated cylinder with $t_h = 0.06\lambda_0$. These results are also compared with those of a planar array (of $\hat{z}-$directed dipoles) with the same parameters (t_h, number of elements, etc.). The $|R|$ values of all the arrays are computed at their center elements, which are conjugate matched to broadside scan. A possible scan blindness is observed at $\theta = 41^\circ$ ($90^\circ - \theta = 49^\circ$) for the cylindrical array of $\hat{z}-$directed printed dipoles along the E-plane as shown in Fig. 5.2(a). At this angle, the reflection coefficient of the center element has a magnitude greater than unity ($|R| > 1$), which means that its input impedance has a negative real part (i.e. $Re(Z_{in}^{mid}) < 0$) . Therefore, this dipole delivers power to its generator implying that this power is delivered from other ports with $|R| < 1$ (i.e. $Re(Z_{in}^{nm}) > 0$) to the middle element. Note that in finite arrays the $|R| > 1$ condition for the center element of the array has been used as a tool to demonstrate the existence/possibility of scan blindness in [4], [2]. Thus, existence of this condition is also treated as an indication of a possible blindness in this paper. However, neither the array of $\hat{\phi}-$directed printed dipoles (on the same coated cylinder) nor the planar array shows blindness at this angle. Also it is observed that the shape of $|R|$ corresponding to the planar case is similar to that of the cylindrical array of $\hat{z}-$directed dipoles and it peaks around the same angle (but $|R| < 1$). This

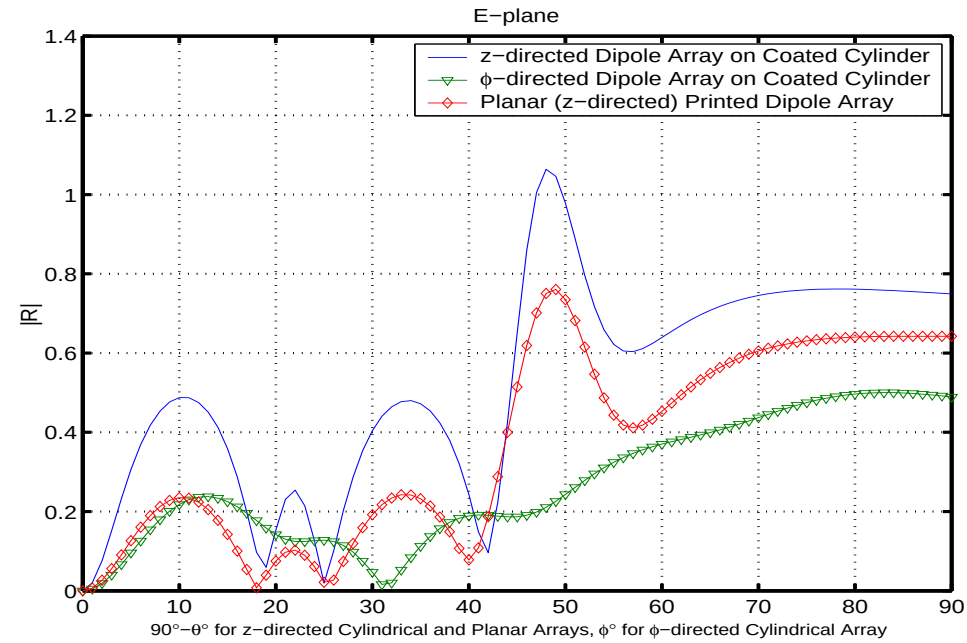

(a)

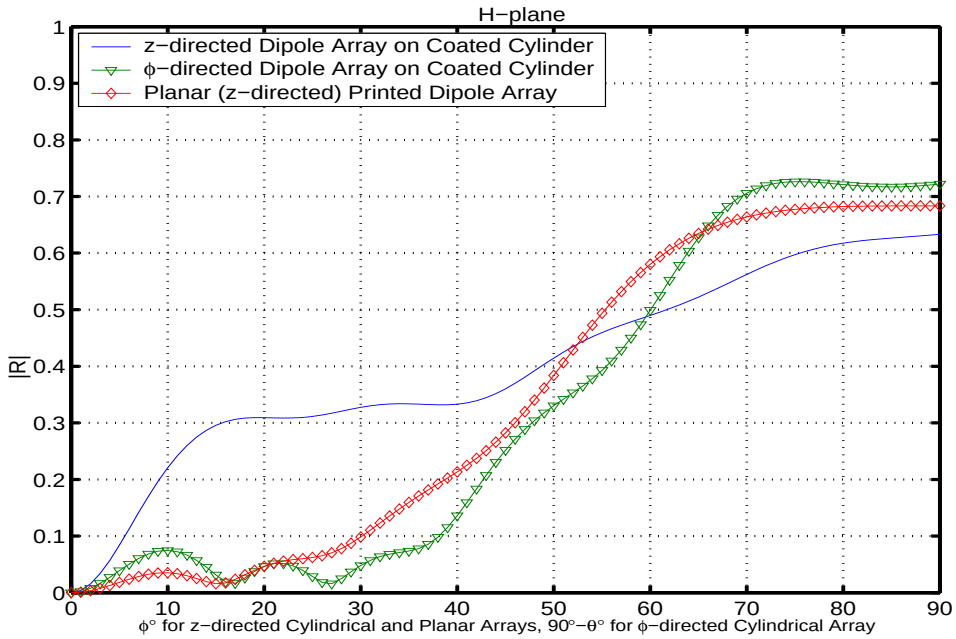

(b)

Figure 5.2: Magnitude of the reflection coefficient, $|R|$, of the middle element vs. scan angle comparison for 11×11 cylindrical arrays of axially ($\hat{z}$) and circumferentially ($\hat{\phi}$) directed printed dipoles, and the same array ($\hat{z}-$directed dipoles) on a planar grounded dielectric slab along the (a) E-plane, (b) H-plane. Array and host body parameters are: $(L, W) = (0.39\lambda_0, 0.01\lambda_0)$, $\epsilon_r = 3.25$, $t_h = 0.06\lambda_0$, $d_z = d_{rl} = d_y = 0.5\lambda_0$, $a = 3\lambda_0$.

may also suggest a potential scan blindness angle for the planar case. On the other hand, none of the arrays shows a scan blindness along the H-plane as illustrated in Fig. 5.2(b). This indicates that E-plane is more critical for relatively thin coatings since only the lowest-order surface wave is present, which confines scan blindness phenomenon to the E-plane [57]. Since the blindness mechanism is closely related to the surface wave fields excited within the substrate of the arrays [23]-[4], the curvature of the supporting structure combined with the array element orientation will change the behavior of these fields. In particular, along the E-plane, surface waves of the $\hat{z}-$directed dipoles on coated cylinders are stronger than $\hat{\phi}-$directed ones and printed dipoles on planar grounded dielectric slabs [43]-[44] (also see Fig. 4.6 (a)). Therefore, if the electrical and geometrical parameters of the array together with its host platform vary in a way to reinforce the surface waves, possibility of observing a scan blindness increases, especially along the E-plane. This is illustrated in Fig. 5.3 and Fig. 5.4 by varying the array size and the thickness of the coating, respectively.

In Fig. 5.3, the effect of the array size on the blindness mechanism is investigated. This is achieved by observing the variation in $|R|$ versus scan angle in the E-plane for arrays of 7×7, 11×11 and 15×15 $\hat{z}-$ and $\hat{\phi}-$directed printed dipoles on a coated cylinder with $a = 4\lambda_0$ and $t_h = 0.06\lambda_0$. As in the previous numerical example, results for planar array are also included for comparison purposes, and $|R|$ values are evaluated for the center elements (which are conjugate matched to broadside scan) of all the arrays. When the size of the array is increased (by adding more elements), surface waves are guided more efficiently along the E-plane for the planar and cylindrical array of $\hat{z}-$directed dipoles. In fact, surfaces waves are stronger for the cylindrical array of $\hat{z}-$directed dipoles when compared to the planar ones [43]. This results in a significant change in the shape of $|R|$ as shown in Fig. 5.3. Based on these results, scan blindness is not possible for the 7×7 arrays (see Fig. 5.3 (a)). However, a peak in the $|R|$ value appears around $\theta = 41^\circ$ ($90^\circ - \theta = 49^\circ$) for both the planar and cylindrical array of 11×11 $\hat{z}-$directed printed dipoles (Fig. 5.3 (b)). This may suggest a potential blindness around this angle even though $|R| < 1$. Finally, observing a scan blindness is possible for the cylindrical array of 15×15 $\hat{z}-$directed dipoles around $\theta = 36^\circ$

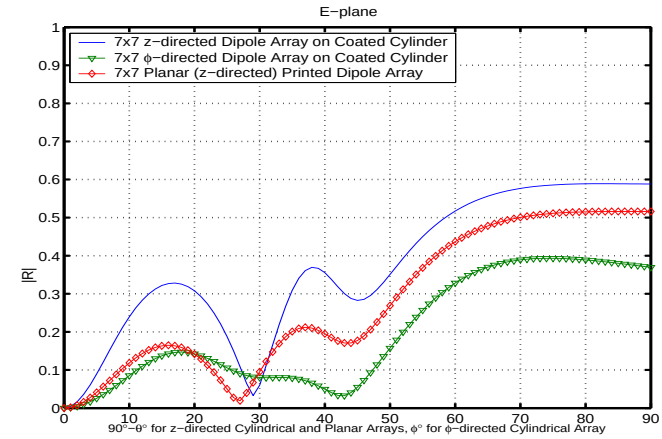

(a)

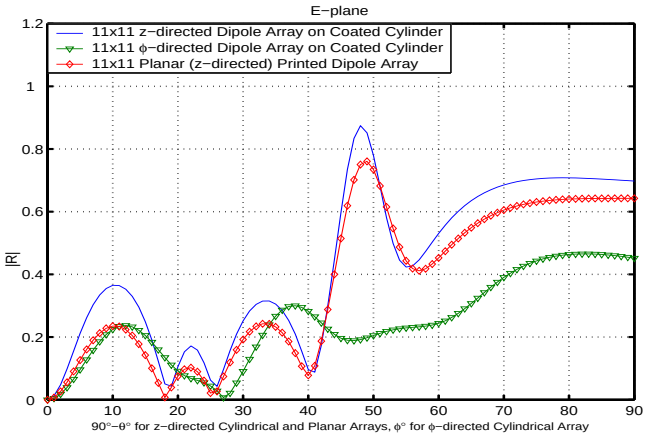

(b)

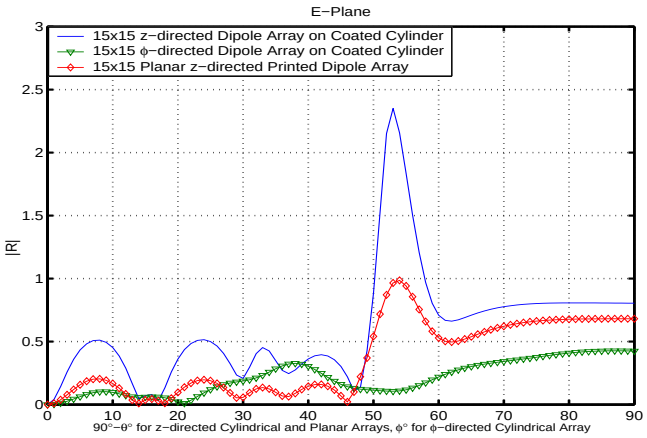

(c)

Figure 5.3: Magnitude of the reflection coefficient, $|R|$, of the middle element vs. scan angle along the E-plane for (a) 7×7, (b) 11×11 and (c) 15×15 $\hat{z}-$ and $\hat{\phi}-$directed printed dipoles on a $4\lambda_0$ coated cylinder. Planar array of $\hat{z}-$directed dipoles is also included. Other array and host body parameters are: $(L, W) = (0.39\lambda_0, 0.01\lambda_0)$, $\epsilon_r = 3.25$, $t_h = 0.06\lambda_0$, $d_z = d_{rl} = d_y = 0.5\lambda_0$.

($90^\circ - \theta = 54^\circ$) where $|R| \approx 2.35$ as clearly seen in Fig. 5.3(c). As expected, the middle element of this array has an impedance with a negative real part around this angle and it delivers power to its generator. For the same sized (i.e. 15×15) planar array, a potential blindness phenomenon also exists around the same angle since $|R|$ is nearly unity. On the other hand, $|R|$ values for the cylindrical array of $\hat{\phi}-$directed dipoles do not change dramatically with the variations in the array size as shown in Fig. 5.3, and the possibility of scan blindness is not observed. The best way to explain this result is to consider how the curvature of the coated cylinder affects the surface waves for this array. As the surface waves propagate along the E-plane, they continuously shed from the surface due to the curvature. Therefore, along the E-plane ($\hat{\phi}-$directed dipoles), surface waves are significantly weaker than those of the planar case [44]. Consequently, when the array size is increased, shedding of the waves from the surface continues to be more dominant than the guiding of these waves.

Results given in Fig. 5.2(a) and Fig. 5.2(b) are repeated for a thinner coating in Fig. 5.4 to further emphasize the importance of the surface waves on the blindness mechanism. Parameters used in Fig. 5.2 are kept the same except the coating thickness is decreased from $0.06\lambda_0$ to $0.02\lambda_0$. A decrease in the thickness of the coating diminishes the strength of the surface waves, which avoids the possibility of a scan blindness phenomenon in both planes. However, $|R|$ for the cylindrical array of $\hat{z}-$directed dipoles is still higher than that of a planar case, and a small local peak around $\theta = 41^\circ$ ($90^\circ - \theta = 49^\circ$) (which would increase for thicker substrates) is still visible as shown in Fig. 5.4(a). Note that the effect of the thickness and the relative dielectric constant (ϵ_r) on scan blindness phenomenon are similar. As it is well known, the "electrical thickness", which depends on the physical thickness, dielectric constant and wavelength, is what matters when surface waves are considered.

The effect of the cylinder radius is discussed next in Fig. 5.5 by plotting $|R^{nm}_{mid}|$ as a function of element position for 11×11 element arrays, where the definition given in (5.6) is used. In all cases, broadside scan is considered. In Fig. 5.5(a), $|R^{nm}_{mid}|$ across the E-plane ($\hat{z}-$direction, i.e. for the elements of the middle row, n=-5:5, m=0) of a $\hat{z}-$directed printed dipole array is shown. Similarly in Fig.

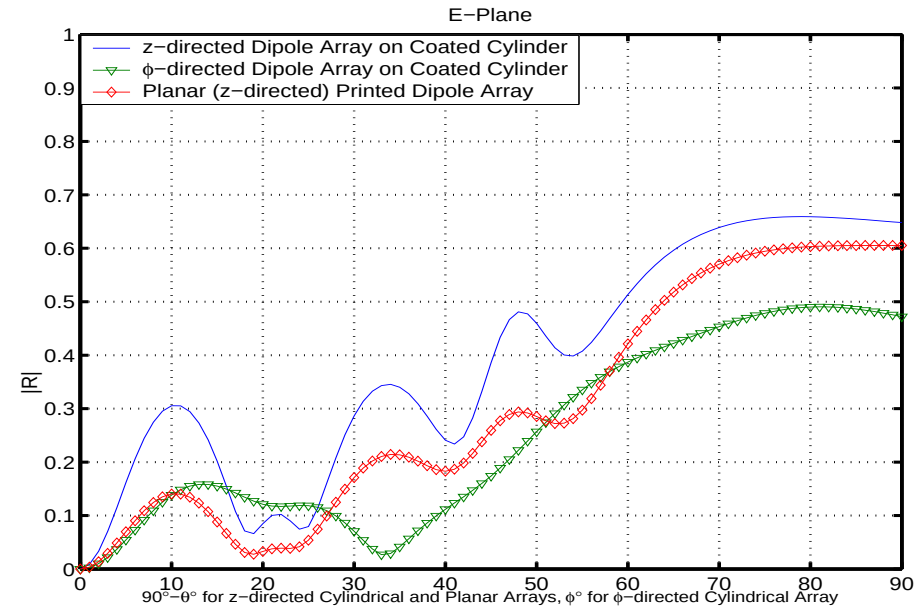

(a)

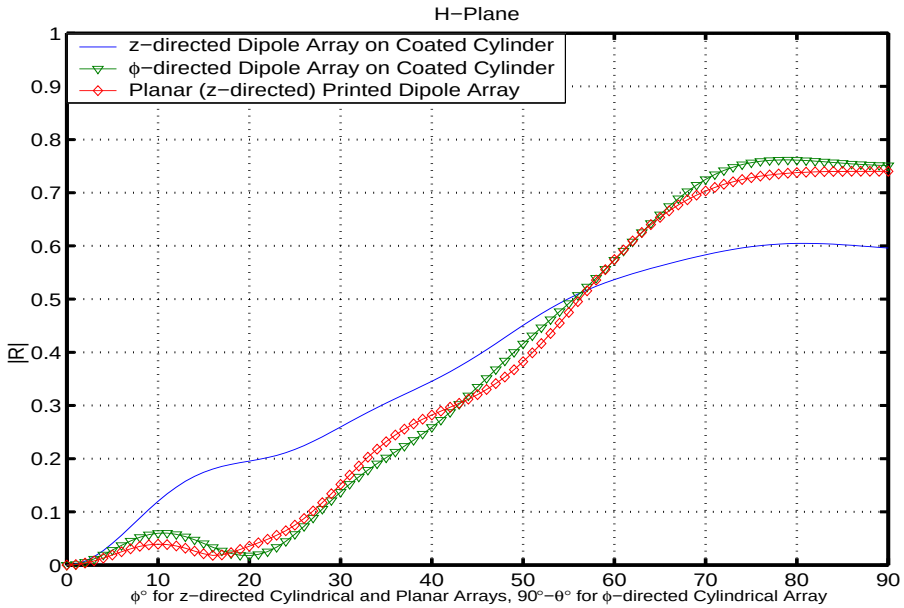

(b)

Figure 5.4: Magnitude of the reflection coefficient, $|R|$, of the middle element vs. scan angle comparison for 11×11 cylindrical arrays of $\hat{z}-$ and $\hat{\phi}-$directed printed dipoles, and the same array (of $\hat{z}-$directed dipoles) on a planar grounded dielectric slab along the (a) E-plane, (b) H-plane. Array and host body parameters are: $(L, W) = (0.39\lambda_0, 0.01\lambda_0)$, $\epsilon_r = 3.25$, $t_h = 0.02\lambda_0$, $d_z = d_{rl} = d_y = 0.5\lambda_0$, $a = 3\lambda_0$.

5.5(b), $|R^{nm}_{mid}|$ across the H-plane ($\hat{z}-$direction, i.e. for the elements of the middle column, n=0, m=-5:5) of a $\hat{\phi}-$directed printed dipole array is given. As seen from these figures, the input impedance across these finite arrays is nonuniform ([4]), in particular across the E-plane of cylindrical $\hat{z}-$directed dipole arrays. In this plane, such a non-uniformity increases as the size of of the radius is decreased, and relatively high variations in $|R^{nm}_{mid}|$ is observed when two consecutive elements are considered. This observation also manifests effects of the surface waves along the axial direction of the coated cylinder. Their strength increases with the decreasing radius [43] (also shown in Fig. 4.6(a)). Besides, the variation of $|R^{nm}_{mid}|$ is symmetric with respect to the center element in both planes, where the center element is perfectly matched at broadside ($|R^{mid}_{mid}| = 0$) and others are either slightly or considerably mismatched. Finally, as expected, the results for the cylinder approach that of a planar case as the radius of the cylinder increases.

Fig. 5.6 compares the finite arrays of printed dipoles on coated cylinders with their planar counterparts using the active element gain patterns defined in (5.8). Active element gain patterns corresponding to the cylindrical array of $\hat{z}-$directed dipoles discussed in Fig. 5.3(c) are shown in Fig. 5.6. These patterns were generated by feeding only the center element of the array and terminating all elements in $Z_T = 15.3 - j * 136.5$, which is the conjugate of the isolated dipole input impedance. First, the H-plane active element gain pattern is shown in Fig. 5.6(a). Along this plane, scan blindness is not observed since the surface waves are weak especially for the cylindrical case ($\hat{z}-$directed dipoles). Hence, the gain pattern is very smooth and nearly no oscillations are observed. Note that planar results are valid up to $\phi = 90^\circ$ due to the infinite substrate and ground plane assumption. On the other hand, for the same arrays, the active element gain pattern is very interesting along the E-plane, where scan blindness was said to be possible around $\theta = 36^\circ$ ($90^\circ - \theta = 54^\circ$) for the cylindrical array of $\hat{z}-$directed dipoles based on Fig. 5.3(c). A null or a dip was expected around this angle in this plane for the cylindrical case. Although the pattern in Fig. 5.6(b) corresponding to the cylindrical case is more oscillatory than that of the planar one, no null in the pattern is observed. The oscillations in the pattern are due to the surface waves which alter the array current distribution and make it more oscillatory

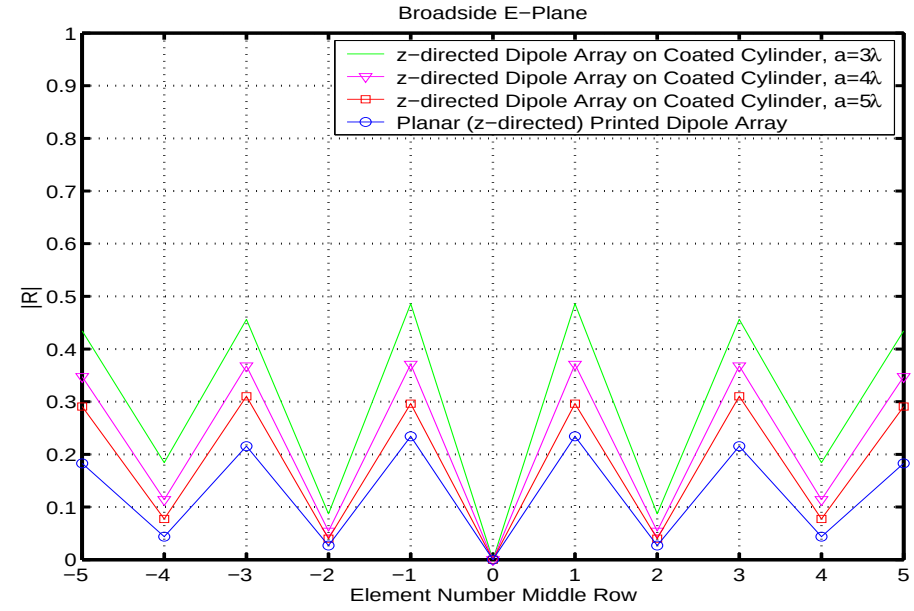

(a)

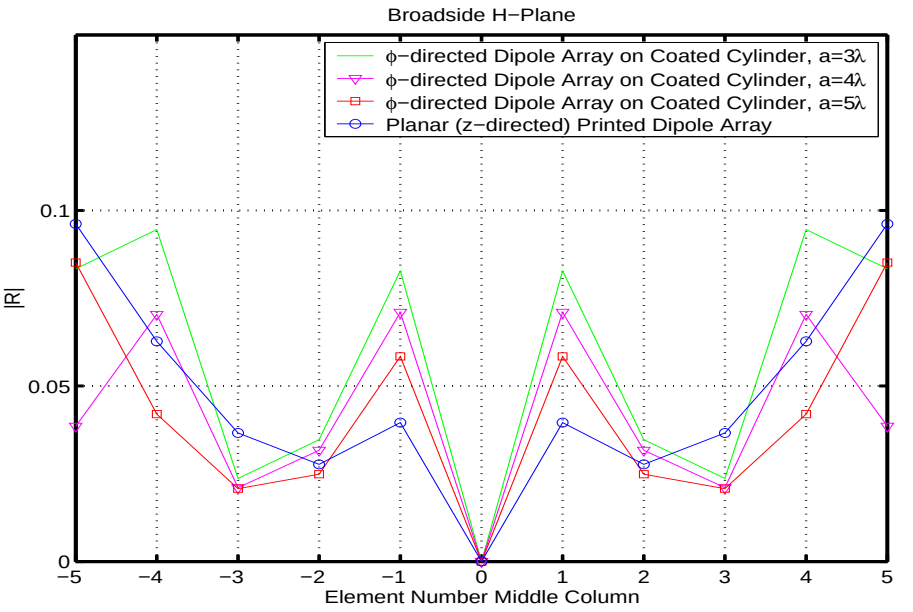

(b)

Figure 5.5: (a) $|R^{nm}_{mid}|$ vs. element position across the E-plane (n=-5:5, m=0) of an 11×11 element $\hat{z}-$directed dipole array on coated cylinders with radii $a = 3\lambda_0$, $a = 4\lambda_0$, $a = 5\lambda_0$ and $a = \infty$ (planar), and (b) same as (a) for an 11×11 element $\hat{\phi}-$directed dipole array across the H-plane (n=0, m=-5:5). Other parameters are $(L, W) = (0.39\lambda_0, 0.01\lambda_0)$, $\epsilon_r = 3.25$, $t_h = 0.06\lambda_0$, $d_z = d_{rl} = d_y = 0.5\lambda_0$.

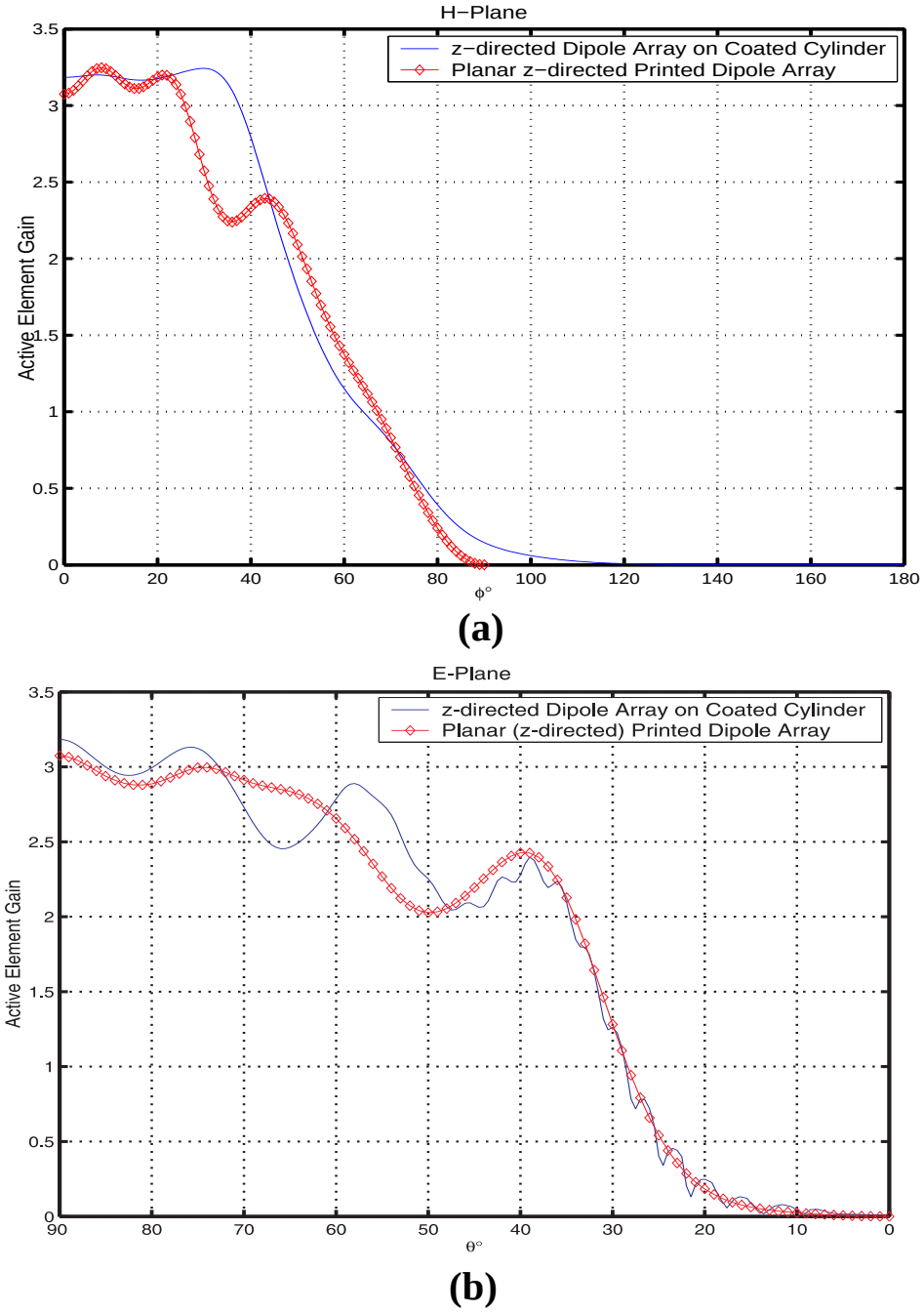

Figure 5.6: (a) H-plane, (b) E-plane active element gain patterns for 15×15 $\hat{z}-$directed printed dipoles on a $4\lambda_0$ cylinder and the same array on a planar grounded dielectric slab. Other array and host body parameters are the same as in Fig. 5.3(c).

(which can be deduced from the $|R|$ versus element position plots in Fig. 5.5(a)). One way to explain this result is to check how many dipoles in the array have a negative resistance (i.e. $Re(Z_{in}) < 0$ equivalent to $|R| > 1$) around this angle. It is observed that if only a small portion of the array elements have a negative resistance, then only a small amount of power is delivered to these elements from the rest of the array elements with $Re(Z_{in}) > 0$, and the remaining power is still radiated. Therefore, a potential "scan blindness" may not manifest itself as a visible dip in the gain pattern. In light of this discussion, this cylindrical array of $\hat{z}-$directed dipoles considered in Fig. 5.3(c), is excited for a scan of (θ, ϕ)=$(36^\circ, 0^\circ)$, which corresponds to the 'blindness angle' (w.r.to $|R| > 1$ result shown in Fig. 5.3(c)). The input impedance of all its elements are plotted on the complex impedance plane in Fig. 5.7(a). The elements experiencing a negative resistance are marked and their locations in the array are shown. Observe that only a small number of elements around the middle of the array have the property $Re(Z_{in}) < 0$ and they extract little power from the array. If more elements had negative resistance, then blindness will be observed in the gain patterns in the form of a visible dip. Finally, in an infinite array, which can be considered as the limiting case, the input impedance of all elements are identical and purely imaginary at the blindness angle. Therefore, a complete blindness would occur and manifests itself as a null in the gain pattern in this plane.

A similar investigation is also performed for the cylindrical array of $\hat{\phi}-$directed dipoles. They are excited at a scan of (θ, ϕ)=$(90^\circ, 54^\circ)$ such that the E-plane scan is performed exactly the same as $\hat{z}-$directed dipole array case. It is observed that $Re(Z_{in})$ values for all elements in this case are positive as clearly seen in Fig. 5.7(b). Based on this information and considering all the previously given numerical results, we can conclude that array element orientation with respect to the curvature of the supporting structure plays a significant role. Considerably different behaviors are observed concerning scan blindness phenomenon for finite arrays of axially and circumferentially directed printed dipoles on cylindrical platforms as well as their planar counterparts.

Finally, the normalized far-field radiation patterns pertaining to 13×13 arrays of $\hat{z}-$ and $\hat{\phi}-$directed dipoles on coated cylinders with radii $3\lambda_0$ and $5\lambda_0$, and their

comparison with patterns of a planar array are shown in Fig. 5.8. The thickness of the coating is $0.06\lambda_0$ for all cases. Fig. 5.8(a) shows the E-plane pattern for the cylindrical array of $\hat{z}-$directed dipoles. In this plane, effects of the curvature on the radiation pattern is minimum. Hence, as expected, patterns resemble to the planar case. However, along the H-plane, where the curvature affects the most, patterns are quite different as seen in Fig. 5.8(b). Agreement with the planar case is observed only in the main beam as well as in the first sidelobe levels. For the cylindrical array of $\hat{\phi}-$directed dipoles, the curvature plays a very significant role along the E-plane. This result is expected since the array elements are oriented perpendicular to the axis of the cylinder. Thus, other than the main beam, a complete disagreement with the planar case is expected and observed as shown in Fig. 5.8(c). The H-plane patterns are shown in Fig. 5.8(d) where the curvature does not have a significant impact and a good agreement is observed with the planar results. In the evaluation of all patterns, all dipoles are excited uniformly and no special beam forming technique is applied in the excitation of the arrays. Note that the ground plane and the substrate are assumed to be infinite for the planar case and the dipoles are $\hat{z}-$directed. Also cylinders are assumed to be infintely long along the $z-$direction (parallel to axis of cylinder). Therefore, patterns for planar array as well as the E-plane pattern for the cylindrical array of $\hat{z}-$directed dipoles and H-plane pattern for the cylindrical array of $\hat{\phi}-$directed dipoles are evaluated from -90° to 90°.

5.4 Conclusion

In this study, a rigorous investigation of surface waves and their effect on scan blindness phenomenon for conformal finite phased arrays of printed dipoles has been performed. Furthermore, effects of several array and supporting structure parameters on the basic performance metrics of arrays and on the blindness mechanism have been discussed. To be able to address these issues, a computationally optimized and very accurate spatial domain hybrid full wave analysis method which is presented in Sections 4.2 and 4.3. has been used Several relatively large but finite arrays pertaining to both axially and circumferentially oriented printed

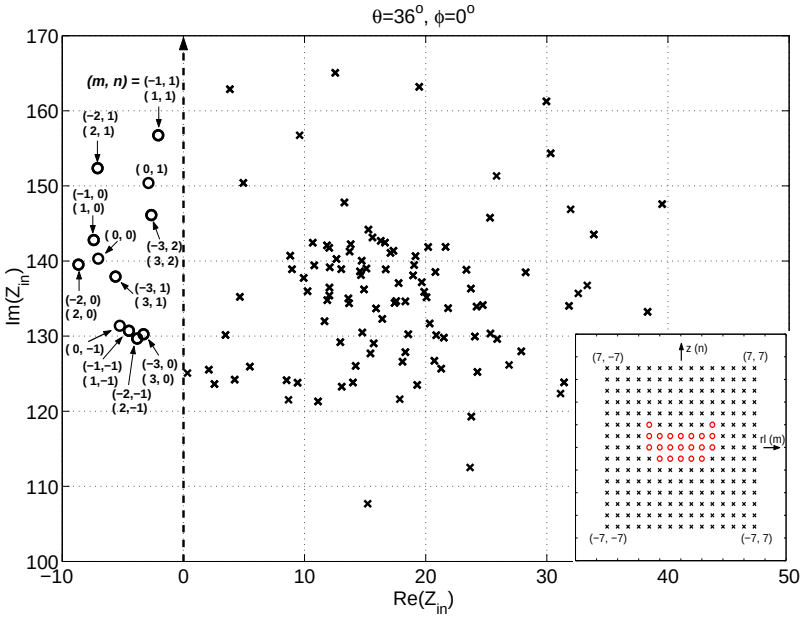

(a)

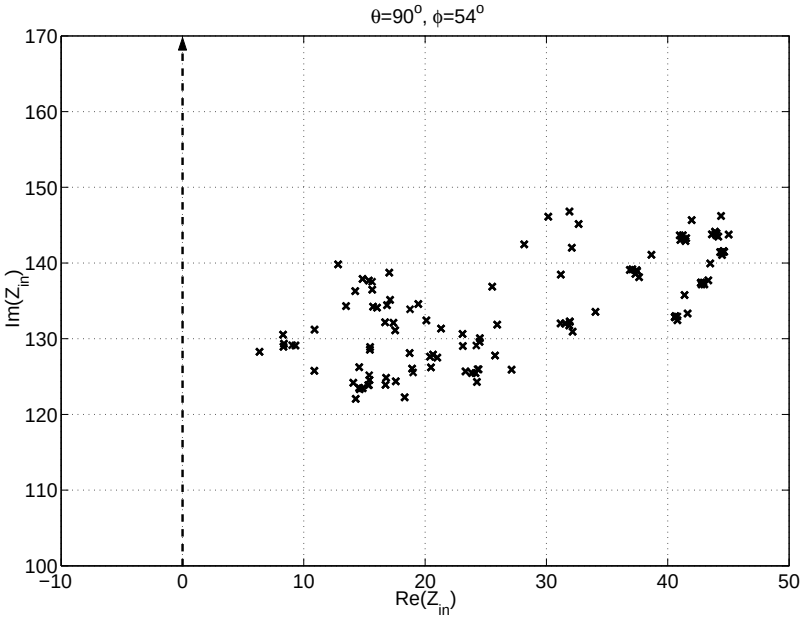

(b)

Figure 5.7: (a) Input impedance (Z_{in}) of all elements for a 15×15 $\hat{z}-$directed dipoles on a $4\lambda_0$ cylinder on the complex impedance plane. Location of the dipoles in the array with negative real resistance values are marked with 'o' (rest is marked with 'x'). (b) Same as (a) for the same sized $\hat{\phi}-$directed printed dipole array on the same cylinder. Other array and host body parameters are the same as in Fig. 5.3(c).

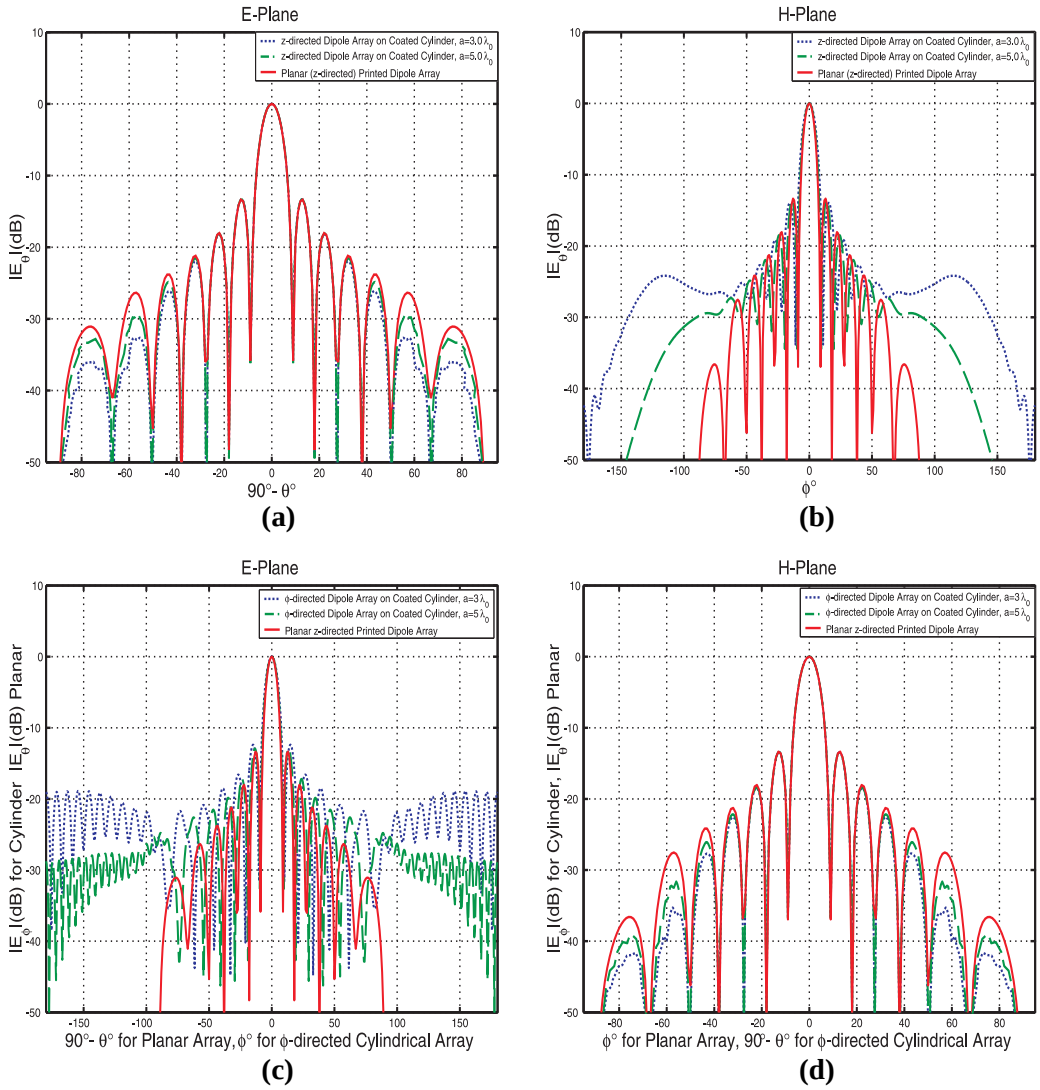

Figure 5.8: Far-field patterns of 13×13 printed dipole arrays on $3\lambda_0$, $5\lambda_0$ cylinders and on planar substrates. Patterns for planar and cylindrical $\hat{z}-$directed dipole arrays along the (a) E-plane, (b) H-plane. Patterns for planar and cylindrical $\hat{\phi}-$directed dipole arrays along the (c) E-plane, (d) H-plane. All arrays are phased to radiate along the broadside direction. Other array and host body parameters are: $(L, W) = (0.39\lambda_0, 0.01\lambda_0)$, $\epsilon_r = 3.25$, $t_h = 0.06\lambda_0$, $d_z = d_{rl} = d_y = 0.5\lambda_0$.

dipoles on coated cylinders with different radii have been studied.

In addition to standard parameters (size of the array, thickness of the substrate, value of the dielectric constant, etc.) that affect the blindness mechanism in finite phased arrays of printed dipoles on planar grounded slabs, it is shown here that the curvature of the supporting structure and the orientation of the array element significantly alters the surface waves excited within the substrate and in turn the blindness mechanism. Consequently, (*i*) finite phased arrays of printed dipoles on coated cylinders and similar arrays on planar grounded slabs show different behavior in terms of scan blindness, (*ii*) unlike planar arrays where scan blindness is mainly governed by the array related factors (substrate parameters, element spacings, etc.) rather than the particular element orientation, scan blindness in cylindrical arrays of printed dipoles is also governed by the orientation of the array elements with respect to the supporting structure. Under the same excitations and with the same array and host body parameters, axially oriented printed dipole arrays can exhibit scan blindness phenomenon, but it may not occur for arrays of circumferentially oriented printed dipoles.

Chapter 6

Efficient Analysis Of Large Finite Phased Arrays of Microstrip Patches Using GFBM With DFT Based Acceleration Algorithm

6.1 Introduction

Conventional integral equation based MoM solutions to the analysis of finite, planar phased arrays of printed antennas on grounded dielectric slabs suffer greatly from the memory storage requirements and computational cost when the number of elements in the array increases rapidly. Several efficient approaches have been proposed to accelerate Method of Moments (MoM) solution and to reduce the memory storage requirements. Some of the MoM based works are infinite array solution as well as its modifications to include array truncation effects [2], the hybrid UTD-MoM approach [12], MoM solution based on a discrete Fourier transform (DFT) representation of the currents, where the number of unknowns are significantly reduced [5], and implementation of iterative methods to the solution of the MoM matrix equation. In a recent study DFT based acceleration

method is combined with an iterative forward-backward method (FBM) successfully for large finite printed dipole arrays with rectangular boundaries [9]. Later on, this DFT-FBM is applied to the large finite printed dipole arrays with elliptical boundaries [58].

In order to use FBM for the analysis of planar finite phased arrays of microstrip patches it must be generalized to handle an arbitrary number of basis functions expanded on each element. In this chapter, a DFT based algorithm is used in conjunction a generalized forward backward method (GFBM) [28] for the fast analysis of planar finite phased arrays of microstrip patches. In this method the unknown current coefficients corresponding to a single patch are first solved by a conventional hybrid MoM/Greens function technique. The current coefficients corresponding to the whole array is then found using GFBM, where it sweeps the current computation element by element (each element corresponds to a probe-fed microstrip patch). A similar approach was reported previously in [59] for linear arrays of elements with arbitrary cross-sections.

The computational complexity of this method, which is originally $O(N_{tot}^2)$ (of order N_{tot}^2) for each iteration, can be reduced to $O(N_{tot})$ (N_{tot} being the total number of unknowns), assuming that elements are identical and periodic. This is achieved using a DFT based acceleration algorithm which divides the contributing elements into "strong" and "weak" interaction groups for a receiving element in the GFBM. The contributions from the strong group are obtained by the conventional element-by-element computation to assure the fundamental accuracy. On the other hand, contributions coming from the weak region are obtained based on a DFT representation of the array current. In general, only a few significant DFT terms are sufficient to provide accurate results due to the fact that they provide minor corrections to the solution in contrast to the dominating strong group.

6.2 Formulation

Problem geometry is illustrated in Fig. 6.1 where dielectric thickness is denoted by t_h and the relative permittivity of the dielectric substrate is ϵ_r. This $(2N + 1) \times (2M + 1)$ element array has inter-element spacing of (dx, dy) where dx is the inter-element distance in the $\hat{x}$-direction and dy in the $\hat{y}$-direction. For an $(2N+1) \times (2M+1)$ array of probe-fed microstrip patches we can write the MoM matrix equation (2.7) in the form of

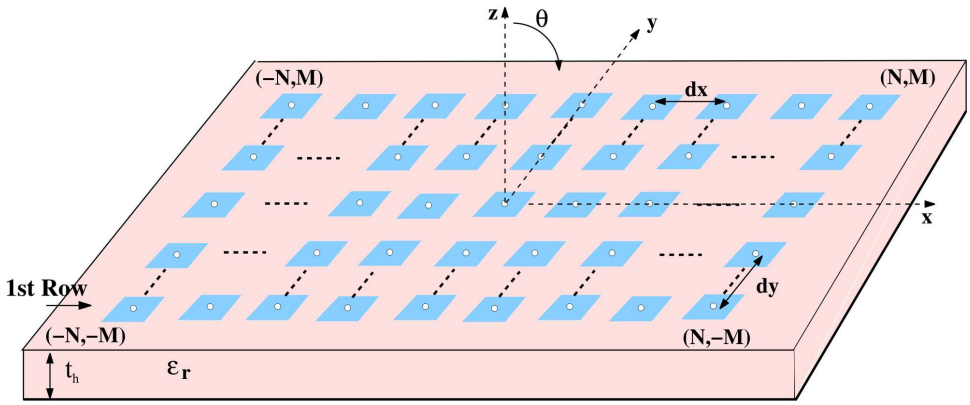

Figure 6.1: Geometry of a periodic, planar array of $(2N+1)\times(2M+1)$ microstrip rectangular patch antennas on a grounded dielectric slab.

$$\sum_{n=-N}^{N} \sum_{m=-M}^{M} \sum_{r=1}^{N_b} A_{nmr} Z_{nmr,pqs} = V_{pqs} e^{-j\beta_x pdx} e^{-j\beta_y qdy} \tag{6.1}$$

where

$$\beta_x = k_0 \sin(\theta_i) \cos(\phi_i), \quad \beta_y = k_0 \sin(\theta_i) \sin(\phi_i), \tag{6.2}$$

$$-N \leq p \leq N, \quad -M \leq q \leq M, \quad -N_b \leq s \leq N_b, \tag{6.3}$$

and (θ_i, ϕ_i) is the scan direction of the main beam. N_b denotes the number of basis functions per element. $Z_{nmr,pqs}$ is the mutual coupling between the nmr^{th} basis function and pqs^{th} testing function, whereas A_{nmr} is the unknown current coefficients to be found. Excitation vector, which is denoted by V_{pqs}, is calculated

using (3.176) where the coordinates $(x_p,\, y_p)$ denote the probe position of the pq^{th} patch whereas the coordinates $(x_m,\, y_m)$ denote the position of the pqs^{th} basis function.

In order to solve (6.1) using GFBM, first step is to decompose current vector as forward and backward components and the MoM impedance matrix in the form of (shown in Fig. 6.2)

$$\mathbf{I} = \mathbf{I}^f + \mathbf{I}^b \tag{6.4}$$

$$\underline{\mathbf{Z}} = \underline{\mathbf{Z}}^{fg} + \underline{\mathbf{Z}}^{sg} + \underline{\mathbf{Z}}^{bg} \tag{6.5}$$

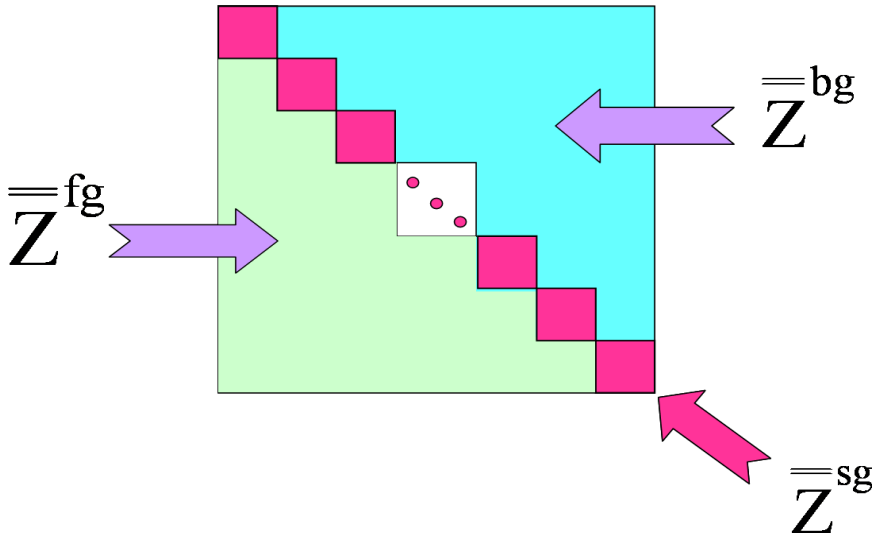

Figure 6.2: Decomposition of Z matrix

where $\underline{\mathbf{Z}}^{sg}$ is formed by the block diagonal matrices of $\underline{\mathbf{Z}}$ corresponding to the impedance matrix of a single patch, where as $\underline{\mathbf{Z}}^{fg}$ and $\underline{\mathbf{Z}}^{bg}$ are the lower and upper triangular parts of $\underline{\mathbf{Z}}$ with $\underline{\mathbf{Z}}^{sg}$ subtracted. Then the original matrix equation (6.1) is transformed into two matrix equations given by

$$\underline{\mathbf{Z}}^{sg}\mathbf{I}^f = \mathbf{V} - \underline{\mathbf{Z}}^{fg}\left(\mathbf{I}^f + \mathbf{I}^b\right) \tag{6.6}$$

$$\underline{\mathbf{Z}}^{sg}\mathbf{I}^b = -\underline{\mathbf{Z}}^{bg}\left(\mathbf{I}^f + \mathbf{I}^b\right) . \tag{6.7}$$

Equations (6.6) and (6.7) are solved iteratively for $\mathbf{I}^b$ and $\mathbf{I}^f$, starting with zero $\mathbf{I}^b(0)$. Since N_b is small compared N_{tot} (which is the total number of unknowns),

GFBM requires $O(N_{tot}^2)$ computational complexity and memory storage. GFBM sweep decomposition is depicted in Fig. 6.3.

To reduce the computational complexity, an acceleration algorithm based on the DFT representation of the induced currents on the array has been proposed, [8], [9]. To calculate the MoM matrix entry of an element (called as the receiving element), this algorithm divides the contributing elements in front of it into strong and weak interaction regions as shown in Fig. 6.4. Strong group is composed of elements within a few wavelength distance from the receiving element, and contributions from them are evaluated by employing a conventional MoM in an element-by-element fashion. To represent the contributions from the weak region, a few significant DFT terms from the DFT representation of the entire array currents are selected. Note that the current on each element is represented by using more than one expansion (basis) function. Therefore, the DFT acceleration algorithm presented in [8] and [9] is slightly modified to handle more basis functions per element. Briefly, when the elements are identical, each element has the same number of basis functions. Therefore, first basis functions of each element are periodic among each other, and can be treated as a periodic array of one basis function per element (i.e., a subarray is formed). The same is true for the second, third, etc., basis functions as well. As a result, contributions coming from the weak region of the overall array can be calculated by combining the weak region contributions of each sub-array using the corresponding DFT coefficients.

The DFT representation of A_{nmr} is given by

$$A_{nmr} = e^{-j\beta_x ndx} e^{-j\beta_y mdy} \sum_{k=-N}^{N} \sum_{l=-M}^{M} B_{klr} e^{-j2\pi \frac{kn}{2N+1}} e^{-j2\pi \frac{lm}{2M+1}} \tag{6.8}$$

where B_{klr} is the coefficient of the kl^{th} DFT term (r^{th} basis functions) given by

$$B_{klr} = \frac{1}{(2N+1)(2M+1)} \sum_{n=-N}^{N} \sum_{m=-M}^{M} A_{nmr} e^{j\beta_x ndx} e^{j\beta_y mdy} e^{j2\pi \frac{kn}{2N+1}} e^{j2\pi \frac{lm}{2M+1}} . \tag{6.9}$$

Then the weak region contributions to the pqs^{th} element can be expressed as

$$E_{weak} = \sum_{r} \sum_{k} \sum_{l} B_{klr} \sum_{n,\, m \in weak} Z_{nmr} e^{-j\beta_x ndx} e^{-j\beta_y mdy} e^{-j2\pi \frac{kn}{2N+1}} e^{-j2\pi \frac{lm}{2M+1}} . \tag{6.10}$$

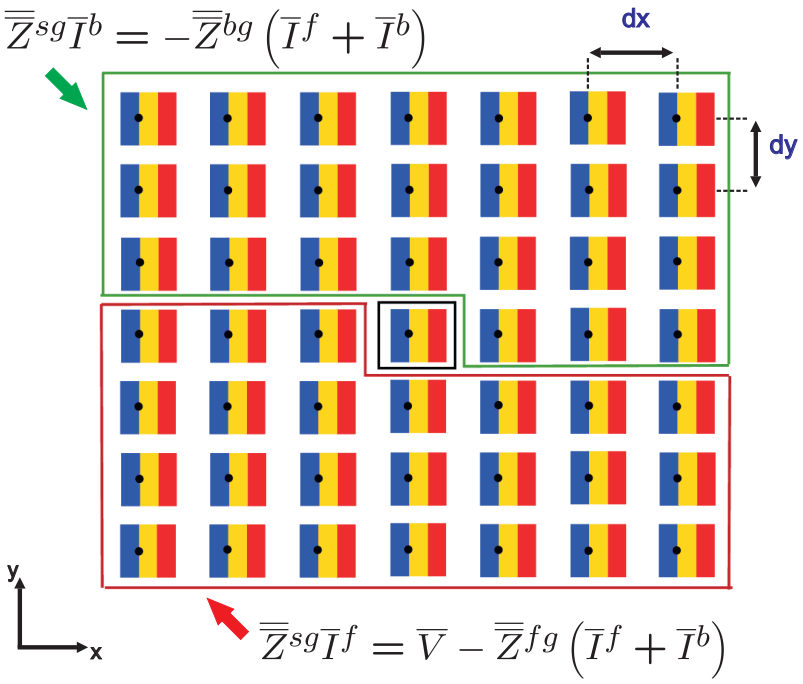

Figure 6.3: GFBM sweep decomposition

It has been observed that the DFT representation of practical large array current distribution is very compact, [5], such that only a few of these DFT coefficients are nonzero. Since the contribution of weak region provides slight corrections, it is sufficient to use a few significant DFT terms in the calculation of (6.10). Sufficient DFT terms are selected based on the criteria given in [5]. By rewriting (6.10) in the form given by

$$E_{weak} = \sum_{r=1}^{N_b} \left[\sum_{kl \in Q} B_{klr} C_{klr,\,pqs} \right] \tag{6.11}$$

where Q is the set of significant DFT terms, and

$$C_{klr,\,pqs} = \sum_{n,\,m \in weak} Z_{nmr,\,pqs} e^{-j\beta_x ndx} e^{-j\beta_y mdy} e^{-j2\pi \frac{kn}{2N+1}} e^{-j2\pi \frac{lm}{2M+1}} \tag{6.12}$$

$C_{klr,\,pqs}$ and hence, E_{weak} can be calculated very efficiently in an iterative fashion apart from the usual GFBM iterations, [9] using the equation given by

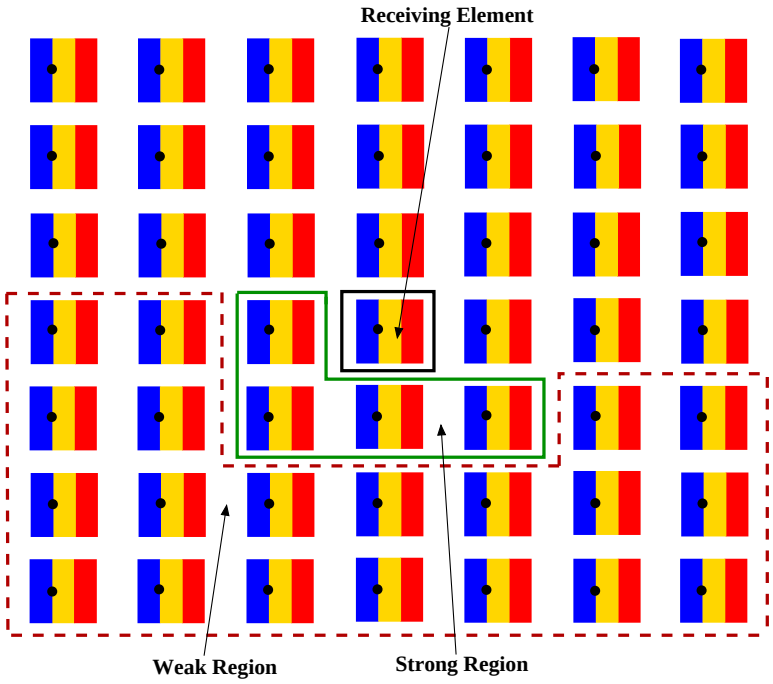

Figure 6.4: Decomposition of strong and weak interaction groups

$$C_{klr,\,pqs} = C_{klr,\,(p-1)qs}\, e^{-j\beta_x n dx} e^{-j2\pi\frac{k}{2N+1}} + \left(\sum_{m=-M}^{M} Z_{(-N)mr,\,pqs} e^{-j\beta_x(-N)dx} e^{-j\beta_y m dy} e^{-j2\pi\left(\frac{k(-N)}{2N+1}+\frac{lm}{2M+1}\right)} \right) \quad (6.13)$$

where the term inside the parenthesis, which is denoted as $D_{klr,\,pqs}$, is given by

$$\begin{aligned} D_{klr,\,pqs} = {} & D_{klr,\,p(q-1)s} e^{-j\beta_y m dy} e^{-j2\pi\frac{l}{2M+1}} \\ & - Z_{(-N)Mr,\,p(q-1)s} e^{-j\beta_x(-N)dx} e^{-j\beta_y(M+1)dy} e^{-j2\pi\frac{k(-N)}{2N+1}} e^{-j2\pi\frac{l(M+1)}{2M+1}} \\ & + Z_{(-N)(-M)r,\,pqs} e^{-j\beta_x(-N)dx} e^{-j\beta_y(-M)dy} e^{-j2\pi\frac{k(-N)}{2N+1}} e^{-j2\pi\frac{l(-M)}{2M+1}} \end{aligned} \quad (6.14)$$

The first term in (6.13) is related to the $C_{klr,\,(p-1)qs}$ which is obtained before $C_{klr,\,pqs}$ is interested. This relation is shown in Fig. 6.5(a) where we see that the weak group of the pqs^{th} receiving element is decomposed into two parts. The

upper sub-group and the lower sub-group which consist of the elements of the first row. Note that the upper sub-group of the pqs^{th} element is identical to the weak group of the $(p-1)qs^{th}$ element except a location shift which corresponds to a phase shift. The next step is the calculation of the second term in (6.13), namely $D_{klr,\,pqs}$, which contains the contributions coming from a one-dimensional array with the receiving element located far away from this array. This term is also calculated in an iterative fashion given by (6.14), using the periodicity of the elements in spatial domain, which corresponds to a phase shift. Since we have more than one basis function to represent the current on each element DFT coefficients are calculated for each subarray, which is shown in Fig. 6.5(b) and Fig. 6.5(c). The basis functions which are not being considered are colored with stripes.

As shown in [9], calculation of $C_{krl,pqs}$ requires only $O(N_{tot})$ operations. Hence, the overall computational complexity is $O(N_{tot})$.

6.3 Numerical Results

To validate the accuracy and the efficiency of the method, some numerical results for printed arrays obtained using the GFBM approach with DFT based acceleration algorithm are presented and compared with the direct solution of MoM. Fig. 6.6 shows the current distribution on the 3^{rd} and 11^{th} rows of an 21x21 array. 3 $\hat{x}$- directed current modes are expanded on each of the patch antenna and the array is scanned to the broadside: $(\theta_i,\, \phi_i) = (0^\circ, 0^\circ)$. Desired accuracy for the currents is achieved within 3 iterations by selecting only 9 elements (3x3) in the strong region and 15 (5 DFT term for each current mode) DFT terms. Moreover, DFT-GFBM is approximately 200 times faster than the conventional MoM with LU decomposition (CPU time of DFT-GFBM: 0.13sec., CPU time of MoM: 25.85sec.). A second example is shown in Fig. 6.7 for an 19x19 array where 10 current modes (4 $\hat{x}$-directed, 6 $\hat{y}$-directed,) are expanded on each of the patch antenna. Current distribution on the 2^{rd} and 10^{th} rows are depicted when the scan angle is again broadside: $(\theta_i,\, \phi_i) = (0^\circ, 0^\circ)$. Desired accuracy for the

currents is achieved within 3 iterations by selecting only 9 elements (3x3) in the strong region and 10 (1 DFT term for each current mode) DFT terms. DFT-GFBM is far more faster (approximately 760 times faster) than the conventional MoM, with a CPU time of only 0.7sec.

6.4 Conclusion

In this chapter an efficient and accurate method is presented for the analysis of large printed antenna arrays on planar grounded dielectric slabs. Both the computational and the memory storage requirements are $O(N_{tot})$.

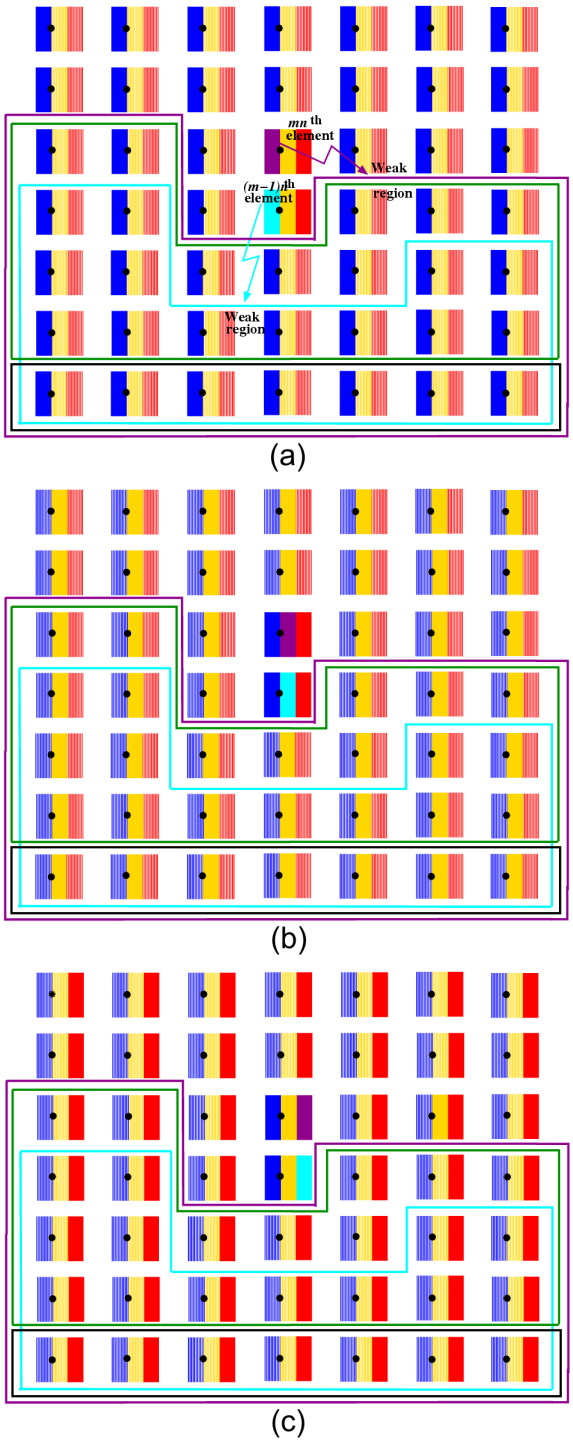

Figure 6.5: The forward weak group corresponding to the pqs^{th} receiving element is decomposed into 2 sub-groups (upper and lower loops). Note that the upper group is identical to the weak group corresponding to the $(p-1)qs^{th}$ element except a location shift which corresponds to a phase shift. This decomposition is repeated for each basis function shown in (a), (b) and (c)

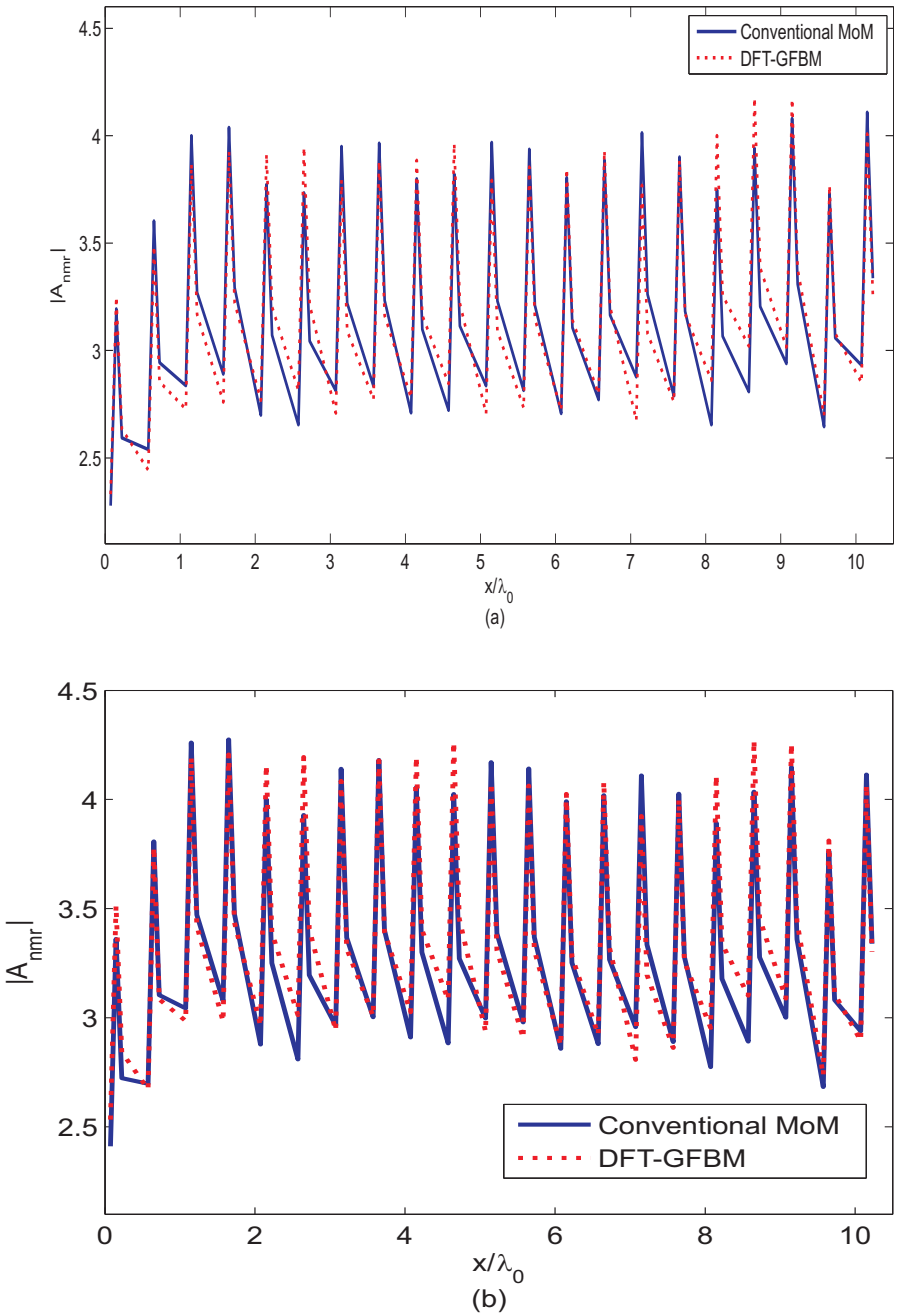

Figure 6.6: 21x21 Patch array on planar substrate. 3 expansion modes ($\hat{x}-$ *directed*) are used per patch. Magnitude of the current coefficients on the (a) 3^{rd} row, (b) 11^{th} row. Other array and host body parameters are $(L,\, W) = (0.3\lambda_0,\, 0.3\lambda_0)$, $d_x = d_y = 0.5\lambda_0$, $t_h = 0.04\lambda_0$, $\epsilon_r = 2.55$.

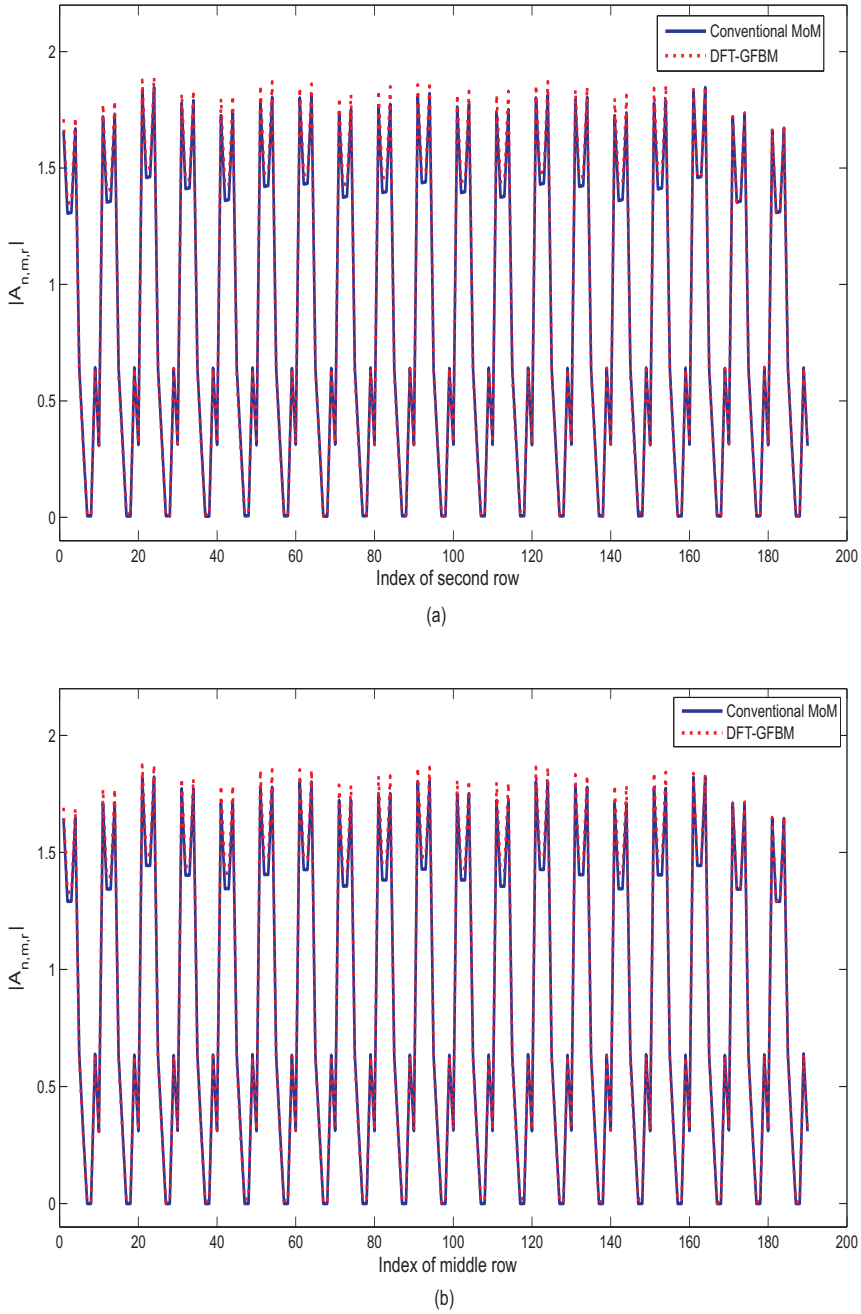

Figure 6.7: 19x19 Patch array on planar substrate. 10 expansion modes (4 $\hat{x}$-directed, 6 $\hat{y}$-directed,) are used per patch. Magnitude of the current coefficients on the (a) 2^{nd} row, (b) 10^{th} row. Other array and host body parameters are $(L,\, W) = (0.33\lambda_0,\, 0.53\lambda_0)$, $d_x = d_y = 0.7\lambda_0$, $t_h = 0.021\lambda_0$, $\epsilon_r = 2.22$.

Chapter 7

Conclusions

In this thesis a hybrid method based on the combination of MoM with special Green's function representations is developed in order to investigate printed antennas/arrays on planar and cylindrical grounded dielectric slabs in both spatial and spectral domains. The accuracy and efficiency of this hybrid MoM/Green's function technique depends on the accurate and efficient evaluation of the MoM impedance matrix entries, which strongly depend on the Green's function representations.

When the spectral domain calculations are considered, a single representation is used for planar geometries and again a single representation is used for cylindrical geometries. However, mutual coupling calculations in this domain has severe convergence issues especially for electrically large lateral separations between the source and observation points. Therefore, several techniques are used to improve their efficiency and accuracy. In this thesis closed-form expressions are derived for the asymptotic parts of both the impedance matrix and the excitation vector of probe fed printed geometries. Implementation of these closed-form expressions to our existing spectral domain MoM codes results a fast and accurate evaluation of MoM matrix and the excitation vector entries.

The spatial domain solution to the printed planar geometries require evaluation of finite double integrals where the main problem is handling the singularities occurring when two basis functions overlap with each other completely or partially. There is also a possible singularity problem in the evaluation of probe-basis function interactions when probe is positioned in the basis function. In this thesis these singularities are treated using mappings and change of variable methods. Numerical results are in a good agreement with the reference spectral domain solution, which is assumed to be pretty accurate when the basis functions overlap. Apart from the singularity treatments, these mappings and change of variable methods are also used when there is no singularity, in order to reduce the order of integrations. The remaining integrals are numerically evaluated using an adaptive Gaussian integration scheme resulting a fast and accurate spatial domain solution for printed planar geometries.

These improved methods are incorporated with two different studies in Chapter 5 and Chapter 6. In Chapter 5 we have presented an investigation of scan blindness phenomenon for finite arrays of printed dipoles on material coated electrically large circular cylinders, and its comparison with the same type of arrays on planar platforms. In this study spatial domain Green's function representations derived in [33] for cylindrical grounded dielectric slabs, given in Chapter 4 are used. Effects of several parameters on scan blindness for cylindrical geometries are presented using various numerical results. The results show that (i) finite phased arrays of printed dipoles on coated cylinders and similar arrays on planar grounded slabs show different behavior in terms of scan blindness, (ii) unlike planar arrays where scan blindness is mainly governed by the array related factors (substrate parameters, element spacings, etc.) rather than the particular element orientation, scan blindness in cylindrical arrays of printed dipoles is also governed by the orientation of the array elements with respect to the supporting structure.

In Chapter 6 we have presented a generalized forward backward method based on a DFT based acceleration algorithm which reduces the computational complexity of the full-wave solution for the analysis of electrically large finite phased arrays of printed dipoles and patches on planar grounded dielectric slabs. This

highly efficient and accurate method reduces the computational complexity of the problem, which is originally $O(N_{tot}^2)$ for each iteration to $O(N_{tot})$.

Bibliography

[1] A. Ishimaru, R. J. Coe, G. E. Miller and W. P. Green, "Finite periodic structure approach to large scanning array problems", *IEEE Trans. Antennas Propagat.*, Vol. 33, No. 11, pp. 1213-1220, November 1985.

[2] A. K. Skrivervik and J. R. Mosig, "Finite phased array of microstrip patch antennas: the infinite array approach", *IEEE Trans. Antennas Propagat.*, Vol. 40, No. 5, pp. 579-582, May 1992.

[3] A. K. Skrivervik and J. R. Mosig, "Analysis of finite phased arrays of microstrip patches", *IEEE Trans. Antennas Propagat.*, Vol. 41, No. 8, pp. 1105-1114, August 1993.

[4] D. M. Pozar , "Analysis of finite phased arrays of printed dipoles", *IEEE Trans. Antennas Propagat.*, Vol.33, No. 10, pp. 1045-1053, October 1985.

[5] H.-T. Chou, H.-K. Ho, P. H. Pathak, P. Nepa and O. A. Civi, "Efficient hybrid discrete Fourier transform-moment method for fast analysis of large rectangular arrays", *IEE Proc. Microwave Antennas Propagat.*, Vol. 149, No. 1 pp. 1-6, February 2002.

[6] H.-T. Chou, H.-K. Ho, O. A. Civi and V. B. Ertürk, "Applications of hybrid discrete Fourier transform-moment method to the fast analysis of large rectangular dipole arrays printed on a thin grounded dielectric substrate", *Microwave Opt. Technol. Lett.*, Vol. 34, No. 3, pp. 203-207, Aug. 5 2002.

[7] P. Janpugdee, *An efficient discrete Fourier transform based ray analysis of large finite planar phased arrays.*, M.S. thesis, The Ohio-State University Dept. of Electrical Engineering, 2002.

[8] H.-T. Chou, H.-K. Ho, "Implementation of a forward-backward procedure for the fast analysis of electromagnetic radiation/scattering from two-dimensional large phased arrays", *IEEE Trans. Antennas Propagat.*, Vol. 52, No. 2, pp. 388-396, February 2004.

[9] Ö. A. Civi, "Extension of forward backward method with DFT based acceleration algorithm for the efficient analysis of radiation/scattering from large finite printed dipole arrays", *Microwave Opt. Technol. Lett.*, Vol. 37, No. 1, pp. 20-26, April 5, 2003.

[10] V. B. Ertürk and H. T. Chou, "Efficient analysis of large phased arrays using iterative MoM with DFT-based acceleration algorithm", *Microwave Opt. Technol. Lett.*, Vol. 39, No. 2, pp. 89-94, October 20, 2003.

[11] Y. Zhuang, K.-L. Wu, C. Wu and J. Litva, "A combined full-wave CG-FFT method for rigorous analysis of large microstrip antenna arrays", *IEEE Trans. Antennas Propagat.*, Vol. 44, No. 1, pp. 102-109, January 1996.

[12] Ö. A Civi, P. H. Pathak, H.-T. Chou and P. Nepa, "A hybrid uniform geometrical theory of diffraction-moment method for the efficient analysis of electromagnetic radiation/scattering from large finite planar arrays", *Radio Science*, Vol. 35, No. 2, pp. 607-620, March-April 2000

[13] A. Neto, S. Maci, G. Vecchi and M. Sabbadini, "A truncated Floquet wave diffraction method for the full-wave analysis of large phased arrays, part2: generalization to 3D cases", *IEEE Trans. Antennas Propagat.*, Vol. 48, No. 4, pp. 601-611, April 2000.

[14] O. A. Civi, V. B. Ertürk, P. H. Pathak, P. Janpugdee and H. T. Chou, "A hybrid UTD-MoM approach for the efficient analysis of radiation/scattering from large, printed finite phased arrays ", *IEEE APS International Symposium and URSI Radio Science Meeting*, Vol.2, pp. 806-809, Boston, July 2001.

[15] A. Polemi, A. Toccafondi and S. Maci, "High-frequency Green's function for a semi-infinite array of electric dipoles on a grounded slab. Part 1: Formulation", *IEEE Trans. Antennas Propagat.*, Vol. 49, No. 12, pp. 1667-1677, December 2001.

[16] S. Maci, A. Toccafondi, A. Polemi and L. B. Felsen, "High-frequency Green's function for a semi-infinite array of electric dipoles on an infinite grounded stratified dielectric slab: part II-spatial domain parameterization", *IEEE Trans. Antennas Propagat.*, Vol. 53, No. 4, pp. 1364-1376, April 2005.

[17] P. Janpugdee and P. H. Pathak, "A DFT-based UTD ray analysis of large finite phased arrays on a grounded substrate", *IEEE Trans. Antennas Propagat.*, Vol. 54, No. 4, pp. 1152-1161, April 2006.

[18] K. L. Wong, *Design of Nonplanar Microstrip Antennas and Transmission Lines* John Wiley & Sons, Inc., New York 1999

[19] L. Josefsson and P. Persson, *Conformal Array Antenna Theory and Design* IEEE Press, Wiley-Interscience 2006

[20] S.-O. Park and C. A. Balanis, Analytical technique to evaluate the asymptotic part of the impedance matrix of Sommerfeld-type integrals, *IEEE Trans. Antennas Propagat.*, Vol. 45, pp. 798-805, 1997.

[21] S.-O. Park, C. A. Balanis and C. R. Birtcher, Analytical evaluation of the asymptotic impedance matrix of a grounded dielectric slab with roof-top functions, *IEEE Trans. Antennas Propagat.*, Vol. 46, pp. 251-259, 1998.

[22] S. Barkeshli, *An efficient approach for evaluating the planar microstrip Green's function and its applications to the analysis of microstrip antennas and arrays*, Ph.D. dissertation, The Ohio-State University Dept. of Electrical Engineering, 1988.

[23] D. M. Pozar and D. H. Schaubert, "Scan blindness in infinite phased arrays of printed dipoles", *IEEE Trans. Antennas Propagat.*, Vol.32, pp. 602-610, June 1984.

[24] D. M. Pozar and D. H. Schaubert, "Analysis of an infinite array of rectangular microstrip patches with idealized probe feeds", *IEEE Trans. Antennas Propagat.*, Vol.32, pp. 1101-1107, October 1984.

[25] D. M. Pozar, "General relations for a phased array of printed antennas derived from infinite current sheets", *IEEE Trans. Antennas Propagat.*, Vol.33, pp. 498-504, May 1985.

[26] D. M. Pozar , "Finite phased arrays of rectangular microstrip patches", *IEEE Trans. Antennas Propagat.*, Vol.34, pp. 658-665, May 1986.

[27] V.B. Erturk, O. Bakir, R.G. Rojas, and B. Guner, "Scan blindness phenomenon in conformal finite phased arrays of printed dipoles", *IEEE Trans. Antennas Propagat.*, Vol.54, pp. 1699 - 1708, June 2006.

[28] M. Pino, L.Landesa, JL Rodriguez, F. Obelleiro, R.J. Burkholder, "The generalized forward-backward method for analyzing the scattering from targets on ocean-like rough surfaces", *IEEE Trans. Antennas Propagat.*, vol.47, no.6, pp.961-968, June 1999.

[29] E.H. Newman, "An overview of the hybrid MM/Green's function method in electromagnetics", *Proceedings of the IEEE.*, Vol.76, no.3, pp. 270 - 282, March 1988.

[30] R. F. Harrington, *Time Harmonic Electromagnetic Fields.*, New York: McGraw-Hill, 1961.

[31] D.M. Pozar, "Input impedance and mutual coupling of rectangular microstrip antennas", *IEEE Trans. Antennas Propagat.*, vol.30, no.6, pp.1191-1196, Nov. 1982.

[32] M. Marin and P. H. Pathak, "Calculation of surface fields created by a current distribution on a coated circular cylinder", Tech. rep. 721565-1, The Ohio State University ElectroScience Lab. Dep. of Electrical Engineering, April 1989.

[33] V. B. Ertürk, *Efficient Hybrid MoM/Green's Function technique to Analyze Conformal Microstrip Antennas and Arrays.* PhD thesis, The Ohio State University ,2000.

[34] D. M. Pozar, Improved computational efficiency for the moment method solution of printed dipoles and patches, *Electromagn.*, 3 (1983), 299-309.

[35] F. Bilotti, A. Alu, F. Urbani and L. Vegni, Asymptotic evaluation of the MOM excitation vector for probe-fed microstrip antennas, *J. of Electromagn. Waves and Appl.*, 19 (2005), 1639-1654.

[36] Ansoft Corporation, ENSEMBLE Version 8.0. www.ansoft.com, Ansoft Corporation, Pittsburgh, PA.

[37] D. H. Schaubert, D. M. Pozar and A. Adrian, Effect of microstrip antenna substrate thickness and permittivity: comparison of theories with experiment, *IEEE Trans. Antennas Propagat.*, 37 (1989), 677-682.

[38] R. C. Hall and J. R. Mosig, Rigorous feed model for coaxially fed microstrip antenna, *Electronics Letters*, 26 (1990), 64-66.

[39] C. A. Balanis, *Antenna Theory Analysis and Design.*, John Wiley & Sons, Inc. New York 1997.

[40] V. B. Ertürk and R. G. Rojas, "Efficient computation of surface fields excited on a dielectric coated circular cylinder", *IEEE Trans. Antennas and Propagat.*, Vol. 48, No.10, pp. 1507-1516, October 2000.

[41] V. B. Ertürk and R. G. Rojas, "Paraxial space-domain formulation for surface fields on a large dielectric coated circular cylinder", *IEEE Trans. Antennas and Propagat.*, Vol. 50, No. 11, pp. 1577-1587, Nov. 2002.

[42] V. B. Ertürk and R. G. Rojas, "Efficient analysis of input impedance and mutual coupling of microstrip antennas mounted on large coated cylinders", *IEEE Trans. Antennas Propagat.*, Vol. 51, pp. 739-749, April 2003.

[43] V. B. Ertürk K. W. Lee and R. G. Rojas, "Analysis of finite arrays of axially directed printed dipoles on electrically large cylinders", *IEEE Trans. Antennas Propagat.*, Vol. 52, pp. 2586-2595, October 2004.

[44] V. B. Ertürk and B. Güner, "Analysis of finite arrays of circumferentially oriented printed dipoles on electrically large cylinders", *Microwave Opt. Technol. Lett.*, Vol. 42, pp. 299-304, August 2004.

[45] D. H. Schaubert, J. A. Aas, M. E. Cooley and N. E. Buris, "Moment method analysis of infinite stripline-fed tapered slot antenna arrays with a ground plane", *IEEE Trans. Antennas Propagat.*, Vol.42, pp. 1161-1166, August 1994.

[46] D. M. Pozar, "Scanning characteristics of infinite arrays of printed antenna subarrays", *IEEE Trans. Antennas Propagat.*, Vol.40, pp. 666-674, June 1992.

[47] D. M. Pozar, "Performance of an infinite array of monopoles in a grounded dielectric slab", *IEE Proc. Microwave Antennas Propagat.*, Vol.137, pp. 117-120, April 1990.

[48] J. P. R. Bayard, M. E. Cooley and D. H. Schaubert, "Analysis of infinite arrays of printed dipoles on dielectric sheets perpendicular to a ground plane", *IEEE Trans. Antennas Propagat.*, Vol.39, pp. 1722-1732, December 1991.

[49] D. H. Schaubert, "A class of E-plane scan blindnesses in single-polarized arrays of tapered-slot antennas with a ground plane", *IEEE Trans. Antennas Propagat.*, Vol.44, pp. 954-959, July 1996.

[50] M. Davidovitz, "Extension of the E-plane scanning range in large microstrip arrays by substrate modification", *IEEE Microwave and Guided Wave Lett.*, Vol.2, pp. 492-494, December 1992.

[51] R. B. Waterhouse and N. V. Shuley, "Scan performance of infinite arrays of microstrip patch elements loaded with varactor diodes", *IEEE Trans. Antennas Propagat.*, Vol.41, pp. 1273-1280, September 1993.

[52] R. B. Waterhouse, "The use of shorting posts to improve the scanning range of probe-fed microstrip patch phased arrays", *IEEE Trans. Antennas Propagat.*, Vol.44, pp. 302-309, March 1996.

[53] R. J. Mailloux, *Phased Array Antenna Handbook.*, Artech House, Inc. Boston 1994

[54] R. C. Hansen, *Phased Array Antennas.*, John Wiley & Sons, Inc. New York 1998.

[55] J. Ashkenazy, S. Shtrikman and D. Treves, "Electric surface current model for the analysis of microstrip antennas on cylindrical bodies", *IEEE Trans. Antennas Propagat.*, Vol.33, pp. 295-300, March 1985.

[56] R. A. Martin and D. H. Werner, "A reciprocity approach for calculating the far-field radiation patterns of a center-fed helical microstrip antenna mounted on a dielectric coated circular cylinder", *IEEE Trans. Antennas Propagat.*, Vol.49, pp. 1754-1762, December 2001.

[57] P. D. Patel, "Approximation location of scan-blindness angle in printed phased arrays", *IEEE Antennas and Propagat. Magazine*, Vol.34, pp. 53-54, October 1992.

[58] O. A. Civi, V. B. Ertürk and H.-T. Chou, "Extension of forward-backward method with dft-based acceleration algorithm for the efficient analysis of large periodic arrays with arbitrary boundaries", *Microwave Opt. Technol. Lett.*, Vol. 47, No. 3, pp. 293-298, Nov. 5, 2005.

[59] H.-T. Chou and H.-K. Ho, "A generalized forward-backward method for the efficient analysis of large array problems", *IEEE APS Int. Symp.*, vol.3, p.40-43 July 8-13, 2001.

Appendix A

Integral Formulas I

The integrals $\mathcal{A}(\chi - x_s)$, $\Im_a(\chi)$, $\Im_b(\chi)$, $\mathcal{B}(\chi)$ and $T(\chi)$, used in (3.24)-(3.26), are evaluated in closed-form in [21] given by

$$\begin{aligned}
\mathcal{A}(x - x_s) = & \int_0^\infty K_0(k_y|\chi - x_s|)\frac{\sin^2(k_y\frac{\Delta y}{2})}{k_y^2}\cos(k_y y_s)\,dk_y \\
= & \pi\left(\frac{\Delta y}{8}\right)\Bigg\{(1+n)\ln\left[(n+1)\Delta y + \sqrt{(\chi - x_s)^2 + (n+1)^2\Delta y^2}\right] \\
& + (n-1)\ln\left[(n-1)\Delta y + \sqrt{(\chi - x_s)^2 + (n-1)^2\Delta y^2}\right] \\
& - 2n\ln\left[n\Delta y + \sqrt{(\chi - x_s)^2 + n^2\Delta y^2}\right] \\
& + \frac{2}{\Delta y}\sqrt{(\chi - x_s)^2 + n^2\Delta y^2} \\
& - \frac{1}{\Delta y}\Bigg[\sqrt{(\chi - x_s)^2 + (n-1)^2\Delta y^2} \\
& + \sqrt{(\chi - x_s)^2 + (n+1)^2\Delta y^2}\Bigg]\Bigg\},
\end{aligned} \tag{A.1}$$

$$\begin{aligned}\Im_a(\chi) &= \int_0^\infty \frac{\sin^4\left(k_x\frac{\Delta x}{2}\right)}{k_x^4}\cos(k_x\chi)\,dk_x \\ &= \begin{cases} \frac{\pi}{96}\left\{(2\Delta x-|\chi|)^3-4(\Delta x-|\chi|)^3\right\}, & |\chi|<\Delta x \\ \frac{\pi}{96}(2\Delta x-|\chi|)^3, & \Delta x\le|\chi|<2\Delta x\,, \\ 0, & |\chi|\ge 2\Delta x \end{cases}\end{aligned} \tag{A.2}$$

$$\begin{aligned}\Im_b(\chi) &= \int_0^\infty \frac{\sin^4\left(k_x\frac{\Delta x}{2}\right)}{k_x^2}\cos(k_x\chi)\,dk_x \\ &= \begin{cases} \frac{\pi}{2}\left(\frac{1}{4}\Delta x-\frac{3}{8}|\chi|\right), & |\chi|<\Delta x \\ \frac{\pi}{2}\left(-\frac{1}{4}\Delta x+\frac{1}{8}|\chi|\right), & \Delta x\le|\chi|<2\Delta x\,, \\ 0, & |\chi|\ge 2\Delta x \end{cases}\end{aligned} \tag{A.3}$$

$$\begin{aligned}\mathcal{B}(\chi) &= \int_0^\infty K_0(k_y\chi)\frac{\sin^3\left(k_y\frac{\Delta y}{2}\right)}{k_y^2}\sin(k_y y_s)\,dk_y \\ &= \frac{\pi}{16}\left\{-3\sqrt{\chi^2+\left(\frac{\Delta y}{2}+y_s\right)^2}+3\sqrt{\chi^2+\left(\frac{\Delta y}{2}-y_s\right)^2}\right. \\ &\quad \sqrt{\chi^2+\left(\frac{3\Delta y}{2}+y_s\right)^2}-\sqrt{\chi^2+\left(\frac{3\Delta y}{2}-y_s\right)^2} \\ &\quad +3\left(\frac{\Delta y}{2}+y_s\right)\ln\left(\frac{\Delta y}{2}+y_s+\sqrt{\chi^2+\left(\frac{\Delta y}{2}+y_s\right)^2}\right) \\ &\quad -3\left(-\frac{\Delta y}{2}+y_s\right)\ln\left(-\frac{\Delta y}{2}+y_s+\sqrt{\chi^2+\left(\frac{\Delta y}{2}-y_s\right)^2}\right) \\ &\quad +\left(-\frac{3\Delta y}{2}+y_s\right)\ln\left(-\frac{3\Delta y}{2}+y_s+\sqrt{\chi^2+\left(\frac{3\Delta y}{2}-y_s\right)^2}\right) \\ &\quad \left.-\left(\frac{3\Delta y}{2}+y_s\right)\ln\left(\frac{3\Delta y}{2}+y_s+\sqrt{\chi^2+\left(\frac{3\Delta y}{2}+y_s\right)^2}\right)\right\},\end{aligned} \tag{A.4}$$

and

$$\begin{aligned}\mathcal{T}(\chi) &= \int_0^{\infty} \frac{\sin^3\left(k_x \frac{\Delta x}{2}\right)}{k_x^2} \sin(k_x\chi)\, dk_x \\ &= \begin{cases} -\frac{\pi}{8}\left(\frac{3}{2}\Delta x + \chi\right), & -\frac{3\Delta x}{2} < \chi < -\frac{\Delta x}{2} \\ \frac{\pi}{4}(\chi), & -\frac{\Delta x}{2} < \chi < \frac{\Delta x}{2} \\ \frac{\pi}{8}\left(\frac{3}{2}\Delta x - \chi\right), & \frac{\Delta x}{2} < \chi < \frac{3\Delta x}{2} \\ 0, & \text{otherwise} \end{cases} \end{aligned} \tag{A.5}$$

where K_0 is the modified Bessel function of the first kind.

The special functions $C(\chi)$ and $\Gamma(\chi)$, which are the analytical expressions of results of the integrals used in (3.27), are evaluated in [35] given by

$$\begin{aligned} C(\chi) &= \frac{\pi}{8} \int_{-\infty}^{+\infty} \frac{1}{\sqrt{\chi^2 + y^2}} \left[\text{rect}\left(\frac{y - y_A}{\Delta y}\right) + \text{rect}\left(\frac{y + y_A}{\Delta y}\right) \right] dy \\ &= \frac{\pi}{8} \Bigg\{ \ln\left(y_A + \frac{\Delta y}{2} + \sqrt{\chi^2 + \left(y_A + \frac{\Delta y}{2}\right)^2} \right) \\ &\quad - \ln\left(y_A - \frac{\Delta y}{2} + \sqrt{\chi^2 + \left(y_A - \frac{\Delta y}{2}\right)^2} \right) \\ &\quad + \ln\left(\frac{\Delta y}{2} - y_A + \sqrt{\chi^2 + \left(\frac{\Delta y}{2} - y_A\right)^2} \right) \\ &\quad - \ln\left(-\frac{\Delta y}{2} - y_A + \sqrt{\chi^2 + \left(-\frac{\Delta y}{2} - y_A\right)^2} \right) \Bigg\} \end{aligned} \tag{A.6}$$

and

$$\begin{aligned}\Gamma(\chi) &= \int_0^{\infty} \frac{\sin^2\left(k_x \frac{\Delta x}{2}\right)}{k_x} \sin(k_x\chi)\, dk_x \\ &= \begin{cases} -\frac{\pi}{4}, & -\Delta x < \chi < 0 \\ 0, & \chi = 0 \\ \frac{\pi}{4}, & 0 < \chi < -\Delta x \\ \pm\frac{\pi}{8}, & \chi = \pm\Delta x \\ 0, & \text{otherwise}\,. \end{cases} \end{aligned} \tag{A.7}$$

Appendix B

Integral Formulas II

The analytical expressions to the results of the integrals defined in (3.28)-(3.31), which are the main building blocks of (3.32)-(3.35), are given by

$$\begin{aligned} f_0(a,x_1,x_2) &= \frac{x_2}{2}\sqrt{x_2^2+a^2}-\frac{x_1}{2}\sqrt{x_1^2+a^2} \\ &\quad +\frac{a^2}{2}\ln\left(\frac{x_2+\sqrt{x_2^2+a^2}}{x_1+\sqrt{x_1^2+a^2}}\right) \end{aligned} \tag{B.1}$$

$$f_1(a,x_1,x_2) = \left(x_2^2+a^2\right)^{3/2}-\left(x_1^2+a^2\right)^{3/2} \tag{B.2}$$

$$\begin{aligned} f_2(a,x_1,x_2) &= \frac{\left[x_2\left(x_2^2+a^2\right)^{3/2}-x_1\left(x_1^2+a^2\right)^{3/2}\right]}{4} \\ &\quad -\frac{a^2}{8}\left[x_2\left(x_2^2+a^2\right)^{1/2}-x_1\left(x_1^2+a^2\right)^{1/2}\right] \\ &\quad -\frac{a^4}{8}\ln\left(\frac{x_2+\sqrt{a^2+x_2^2}}{x_1+\sqrt{a^2+x_1^2}}\right) \end{aligned} \tag{B.3}$$

$$\begin{aligned} f_3(a,x_1,x_2) &= \frac{1}{15}\left(x_2^2+a^2\right)^{3/2}\left(3x_2^2-2a^2\right) \\ &\quad -\frac{1}{15}\left(x_1^2+a^2\right)^{3/2}\left(3x_1^2-2a^2\right) \end{aligned} \tag{B.4}$$

$$F_0(a,x_1,x_2,x_s) = f_0(a,x_1-x_s,x_2-x_s) \tag{B.5}$$

$$\begin{aligned} F_1(a,x_1,x_2,x_s) &= f_1(a,x_1-x_s,x_2-x_s) \\ &\quad + x_s\, f_0(a,x_1-x_s,x_2-x_s) \end{aligned} \tag{B.6}$$

$$\begin{aligned} F_2(a,x_1,x_2,x_s) &= f_2(a,x_1-x_s,x_2-x_s) \,+\, 2x_s\, f_1(a,x_1-x_s,x_2-x_s) \\ &\quad + x_s^2\, f_0(a,x_1-x_s,x_2-x_s) \end{aligned} \tag{B.7}$$

$$\begin{aligned} F_3(a,x_1,x_2,x_s) &= f_3(a,x_1-x_s,x_2-x_s) \,+\, 3x_s\, f_2(a,x_1-x_s,x_2-x_s) \\ &\quad + 3x_s^2\, f_1(a,x_1-x_s,x_2-x_s) \\ &\quad + x_s^3\, f_0(a,x_1-x_s,x_2-x_s) \end{aligned} \tag{B.8}$$

$$\begin{aligned} g_0(a,x_1,x_2) &= x_2 \ln\left(a+\sqrt{x_2^2+a^2}\right) - x_1 \ln\left(a+\sqrt{x_1^2+a^2}\right) \\ &\quad -(x_2-x_1) + a \ln\left(\frac{x_2+\sqrt{a^2+x_2^2}}{x_1+\sqrt{a^2+x_1^2}}\right) \end{aligned} \tag{B.9}$$

$$\begin{aligned} g_1(a,x_1,x_2) &= \frac{x_2^2}{2} \ln\left(a+\sqrt{x_2^2+a^2}\right) - \frac{x_1^2}{2} \ln\left(a+\sqrt{x_1^2+a^2}\right) \\ &\quad + \frac{a}{2}\left(\sqrt{x_2^2+a^2}-\sqrt{x_1^2+a^2}\right) - \frac{1}{4}\left(x_2^2-x_1^2\right) \end{aligned} \tag{B.10}$$

$$\begin{aligned} g_2(a,x_1,x_2) &= \frac{x_2^3}{3} \ln\left(a+\sqrt{x_2^2+a^2}\right) - \frac{x_1^3}{3} \ln\left(a+\sqrt{x_1^2+a^2}\right) \\ &\quad - \frac{(x_2^3-x_1^3)}{9} + \frac{a}{6}\left(x_2\sqrt{x_2^2+a^2} - x_1\sqrt{x_1^2+a^2}\right) \\ &\quad - \frac{a^3}{6} \ln\left(\frac{x_2+\sqrt{x_2^2+a^2}}{x_2+\sqrt{x_1^2+a^2}}\right) \end{aligned} \tag{B.11}$$

$$\begin{aligned} g_3(a,x_1,x_2) &= \frac{x_2^4}{4} \ln\left(a+\sqrt{x_2^2+a^2}\right) - \frac{x_1^4}{4} \ln\left(a+\sqrt{x_1^2+a^2}\right) \\ &\quad - \frac{(x_2^4-x_1^4)}{16} + \frac{a\,(x_2^2-2a^2)}{12}\sqrt{x_2^2+a^2} \\ &\quad - \frac{a\,(x_1^2-2a^2)}{12}\sqrt{x_1^2+a^2}\,, \end{aligned} \tag{B.12}$$

$$G_0(a, x_1, x_2, x_s) = g_0(a, x_1 - x_s, x_2 - x_s) \tag{B.13}$$

$$\begin{aligned} G_1(a, x_1, x_2, x_s) &= g_1(a, x_1 - x_s, x_2 - x_s) \\ &\quad + x_s\, g_0(a, x_1 - x_s, x_2 - x_s) \end{aligned} \tag{B.14}$$

$$\begin{aligned} G_2(a, x_1, x_2, x_s) &= g_2(a, x_1 - x_s, x_2 - x_s) + 2x_s\, g_1(a, x_1 - x_s, x_2 - x_s) \\ &\quad + x_s^2\, g_0(a, x_1 - x_s, x_2 - x_s) \end{aligned} \tag{B.15}$$

$$\begin{aligned} G_3(a, x_1, x_2, x_s) &= g_3(a, x_1 - x_s, x_2 - x_s) + 3x_s\, g_2(a, x_1 - x_s, x_2 - x_s) \\ &\quad + 3x_s^2\, g_1(a, x_1 - x_s, x_2 - x_s) \\ &\quad + x_s^3\, g_0(a, x_1 - x_s, x_2 - x_s)\,. \end{aligned} \tag{B.16}$$